INTERNATIONAL JOURNAL OF
IJCOE
COASTAL, OFFSHORE & ENVIRONMENTAL ENGINEERING

Volume 8 | Issue 4 | Nov 2023

www.ijcoe.org info@ijcoe.org

International Journal of Coastal, Offshore and Environmental Engineering (IJCOE) Vol. 8 / Issue. 4 / Nov 2023

International Journal of Coastal, Offshore & Environmental Engineering
Since 2015
ISSN: 2980-8731 (online)

Volume 8 | Issue 4| Nov 2023
IJCOE
Editor-in-Chief: Prof. Hamid S.Bahai

International Journal of Coastal, Offshore & Environmental Engineering
Since 2015
ISSN: 2980-8721 (online)

In The Name of God

Message from the Editor-in-Chief

The IJCOE journal office was established in 2015,and its first issue was published in 2016. TheIJCOE covers a wide range of research in thefields of oceanography & ocean technology, aswell as marine industries & marine engineering.The editorial board of IJCOE consists of nearly130 of the greatest scientists and researchersfrom over 30 countries worldwide, and thejournal's review board comprises 1,000 membersfrom all five continents. The membership andapplication process for joining the editorial andreview boards of this journal is ongoing. IJCOE isa research-academic quarterly journal that haspublication and distribution permissions fromthe Press Organization and permission topublish scientific-research articles from theMinistry of Science, Research, and Technology(MSRT) with an "A" rating. It also holds a "Q1"rating from the ISC institute with an impactfactor (IF) of approximately 0.43 and isconsidered a "core journal" (prestigious andoutstanding journal). IJCOE is an open-accessjournal and allows the download and receipt ofaccepted articles in full text for free. It respectsand adheres to copyright and COPE regulations.The journal's office operates 24/7, providingservices to researchers. In addition to publishinga regular quarterly journal, IJCOE has 16 specialissues on specific topics in preparation. It alsoprovides conditions for publishing specializedbooks, references, and handbooks. Moreover, itis ready to cooperate with the secretariats ofreputable international conferences to publishtheir selected and outstanding articles. IJCOEevaluates, appraises, and publishes books,articles, and the scientific achievements andfindings of esteemed researchers and scientistsworldwide who are innovating and conductingin-depth research in the "important and strategicfield of the maritime technology & Oceanengineering." It welcomes any form of jointcooperation with universities, research institutes,and related research centers at the national,regional, and international levels, and extends ahand for collaboration.

Classification of Editorial Board in IJCOE

Editor-in-Chief

Director-in-Chief

Deputy Editor

Executive Managers

English Text Editor

Technical Editor

International Editorial Board

National Editorial Board

Editorial Board Associate

Editorial Board Assistant

Guest Editorial Board

Advisory Board

Administrative Coordinator

Honorary Board Member

Methodology Advisor

Author Benefits

- Open Access
- Rapid Publication
- Thorough Peer-Review
- No Copyright Constraints
- Coverage by Leading Indexing Services
- Discounts On Article Processing Charges (APC)
- No Space Constraints, No restriction on the maximum length of the papers, number of figures or colors

INTERNATIONAL JOURNAL OF IJCOE COASTAL, OFFSHORE & ENVIRONMENTAL ENGINEERING

Aims of IJCOE

Hydrodynamics

Marine equipment

Structural mechanics

Ocean environmental predictions

Stochastic calculations Experimental

Automatic Control of Marine Systems

Scope of IJCOE

Marine Hazards

Ocean Acoustics

Naval Architecture

Ocean Engineering

Coastal Engineering

Marine Meteorology

Marine Earth Sciences

Underwater Technology

Marine Renewable Energy

Polar & Arctic Engineering

Marine Renewable Energy

Marine Geography & Geodesy

Marine Environmental Engineering

Automatic Control of Marine Systems

Hydro Physics & Physical Oceanography

Type of papers

- Case Studies
- Book Reviews
- Review Article
- Letters to the Editor
- Methodology Papers
- Editorials and Commentaries
- Response or Rejoinder Papers
- Perspective or Opinion Papers
- Conceptual or Theoretical Papers
- Meta-Analysis and Systematic Reviews
- Short Communications or Brief Reports
- Research Articles (Original Research Papers)

Scientific Research Journal

Ministry of Science, Research And Technology (MSRT)

Jurnal Ranking 2023: A

Ministry Of Science, Research And Technology (ISC)

Citation Impact 2022: 0.429

Quartile 2022 : Q1

Core Collection

IJCOE is a Member of

Cantact Us

Office 1 | Research Institute of Meteorology and Atmospheric Science

Address | Tehran, Shahid Kharrazi Highway, Pajoohesh Blvd, Research Institute of Meteorology and Atmospheric Science, Sand and Dust Storm International Research Center (SDS-IRC), No. 13, 1st floor.

Phone | +982144787652

Postal code | 13611-14977

website | www.rimac.ac.ir

Office 2 | Iranian National Institute for Oceanography and Atmospheric Science

Address | Tehran, Dr. Fatemi Gharbi St., Shahid Etemadzade St., No. 3, third floor.

Phone | +982166944873

Postal code | 13389 – 14118

website | www.inio.ac.ir

Email | Info@ijcoe.org

Website | www.ijcoe.org

Follow Us

www.ijcoe.org

INTERNATIONAL JOURNAL OF IJCOE COASTAL, OFFSHORE & ENVIRONMENTAL ENGINEERING

Volume & Issue:

Volume 8, Issue 4, November 2023

Number of Articles: 6

Content

INTERNATIONAL JOURNAL OF
COASTAL, OFFSHORE & ENVIRONMENTAL ENGINEERING IJCOE Vol.8/No. 4/Autumn 2023 (1-8)

Available online at: www. Ijcoe.org

Experimental Study on Assessing Interaction of Quay Walls and Random Waves Using Artificial Neural Network

Ramin Vafaeipour Sorkhabi[1*], Reza Gholi Ejlali[1], Alireza Naseri[1], Amin Hosseinchi Gharehaghaji [2]

[1] *Department of Civil Engineering, Tabriz Branch, Islamic Azad University, Tabriz, Iran*
[2] *Department of Geomatics Engineering, Faculty of Civil Engineering, University of Tabriz, Tabriz, Iran*

ARTICLE INFO

Article History:
Received: 18 Feb. 2020
Accepted: 11 Sep. 2023

Keywords:
Quay Wall
Random Waves
Strain
ANN
Peak Frequency
Wave Height

ABSTRACT

Quay walls are sheltering structures used for protecting coastal regions against wave-induced forces. Because of the random nature of the wave behavior, the application of physical models for the study of wave-structure interaction can be quite efficient. The aim of this study was to investigate the behavior of quay walls under random waves through experimental methods. The study used walls with vertical geometrical form, which were exposed to sea random waves under the JONSWAP spectrum. Surface level and wall strain values were measured using built-in sensors. A neural network model was developed using the feed-forward method with the backpropagation algorithm to analyze the time series of water surface level and strain. High coefficients of determination during the training and verification phases were observed, indicating good network performance. Self-correlation analysis of the time series showed that the data exhibited first-degree Markov characteristics. This finding was taken into consideration and increased the coefficients of determination in the neural network model.

1. Introduction

The wide coastlines in the country, the concentration of population and industry in the coastal areas, and damages from stormy waves necessitate examining the resistant structures against waves as one of the essential requirements [1]. Numerous studies have been conducted on the protection of coasts against waves. In a study, Alami et al. tested a combination of reinforced coastal structures to reduce wave energy and observed that with a decrease in wave height, coasts are subjected to less damage [2]. Quay walls are one of the most important structures, which significantly protect the coasts. In addition to bearing the sea waves that are imposed randomly, these walls should resist other forces such as earthquakes, sea currents, wind, and the impact of floats on the sea according to the environmental conditions. One of the important tools for measuring the interaction between these factors is the application of physical models used broadly by researchers and engineers in recent years [3]. The foundation of these models can be traced back to the 15th century when Leonardo DaVinci proposed the physical principles underlying them. Later in the 17th century, Newton provided a comprehensive explanation of these principles. To study such physical phenomena, it is essential to collect accurate data under controlled conditions. The collected data can then be processed and analyzed to gain insights into the problem. However, despite numerous studies on the reaction between quay walls and irregular waves, not many have explored the relationship between wave-induced forces and the internal forces acting on the walls. In this research, the wall strain was measured by identifying strain on the wall during interaction with the random wave. The relationship between them was specified via the experimental model [4]. The modeling of the neural networks between the wave forces and the wall strain determines the relationship between these parameters, and the appropriate coefficient of determination expresses the efficiency of this model. Sainflou proposed a method for determining the pressure resulting from irregular waves for the first time. The advantage of his method was the feasibility of its application. By this method, the pressure distribution can be estimated approximately in a direct line [5]. Rundgren (1958) showed that the Sainflou method depicts the random waves force more than the actual amount [6]. The Minikin theory was proposed in 1950 based on experimental observations on large

walls under regular broken waves. Indeed, the work of Mini Kane was the first experimental research that investigated the effect of Ashlee in his studies in a comprehensive way [7]. The most famous studies on the impact of the waves on the quay walls and vertical breakers were conducted by Goda in 2010 that are used by engineers for designing [8]. In experimental research, Vijayakrishna et al. (2004) investigated the dynamic wall response against regular waves in energy-absorbent structures [9]. Huge (2004) studied the flexural anchor in offshore structures against waves [10]. Nilamani et al. (2004) examined the impact of roughness on the quay walls as intrusion and extrusion chess blocks on the mentioned wall in an experimental approach and also studied the upstream and downstream waves and their effect on the implied forces by the waves. The wall was thin and deformable, and the back of the wall was considered vacant. The advantage of their work was using irregular waves and sloped walls with different slopes [11]. A method presented by Cumo et al. (2010) is suitable for scaling up impact pressures measured during small-scale physical model tests. The method accounts for air leakage's effect and applies to wave impact loads on different coastal structures. This methodology's applications to wave impacts on seawalls or caisson breakwaters have been studied [12].

Based on the conducted experimental and numerical studies, in the current research, the experimental study on assessing interaction of quay walls and random waves using ANN has been carried out using an artificial neural network.

2. Methodology

2.1. Random waves

In general, the waves are divided into regular and random waves. Random waves can be defined as a combination of regular waves. The sea waves in the stormy state are random [13]. In this condition, zero up Crossing and Zero down Crossing methods and the hydrodynamic wave features are mapped. The Zero up crossing method is common and used in this research. Figure 1 shows the Zero up crossing method [14, 15].

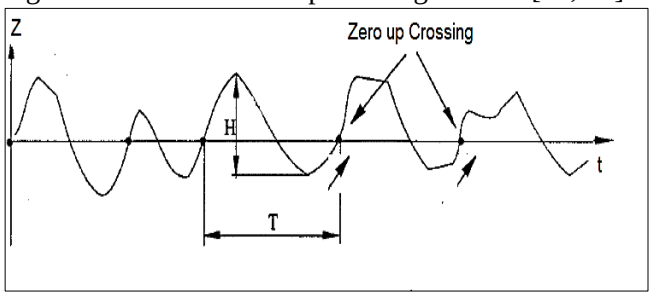

Figure 1. Random wave (field and experiential waves) [15]

2.2. Wave spectrum analysis

The random waves can be investigated using spectrum analysis on the recorded waves, which in this regard, spectrum density can offer a comprehensive justification of the waves in the sea conditions. Accordingly, the different spectrums, such as Bretschnider in 1959, P-M in 1964, TMA in 1985, and JONSWAP in 1974, were defined from the registered data. Sorenson introduced the JONSWAP spectrum as one of the most applicable spectrums in coastal structure design [16, 17]. A recent study has undertaken new research to create a spectrum that accurately reflects Iran's climate. To achieve this objective, the researchers utilized the JONSWAP spectrum, as depicted by Equation (1) and illustrated in Figure 2. These findings represent a significant step towards understanding and modeling Iran's climate patterns [14].

$$S(f) = \frac{\alpha g^2}{(2\pi)^4 f^5} e^{-1.25\left(f_p/f\right)^4} \gamma^a \quad (1)$$

Where γ is usually considered 1.6 to 6; however, 3.3 has been introduced as the best value in most references. The coefficient of γ is the density ratio in the maximum frequency spectrum JONSWAP to spectrum P-M [18]. Also, α and f_p Are defined in equations (2) to (4).

$$a = e^{-[(f-f_p)/(2\sigma^2 {f_p}^2)]} \quad (2)$$

$$\alpha = 0.076\left(\frac{gF}{W^2}\right)^{-0.22} \quad (3)$$

$$f_p = \frac{3.5g}{W}\left(\frac{gF}{W^2}\right)^{-0.33} \quad (4)$$

In these equations, *F*, Fetch length, *W* is the wind velocity, *f is the frequency, and* f_p is the peak frequency.

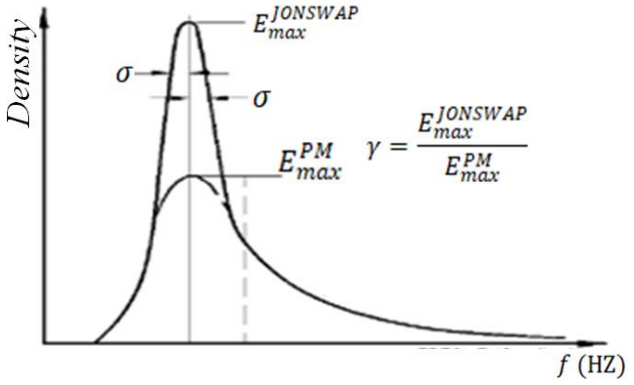

Figure 2. JONSWAP wave spectrum [19]

2.3. Physical model and experiments

The specifications were prepared for the current research, and the wave flume was designed and built in the Tabriz University Marine Structures Laboratory. The specifications used for experiments are as follows (figure 4).

- Length of flume: 12.5m
- Width of flume: 1.15m
-The length flume floor from the ground level is 75cm.
-Inside flume height: 1.05 m
- Water depth (d): 60 cm

-Wave generator type: hinged (Figure 3)
-Wall type: impermeable, without wave overhead, clipped on the floor, free in the margins
-Used waves: random under the JONSWAP spectrum
-Water level sampling frequency: 10 Hz
-Sampling frequency from the wall strain: 50 Hz

(a)

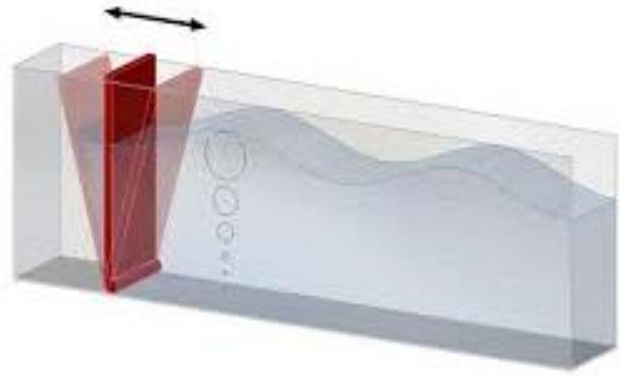

(b)

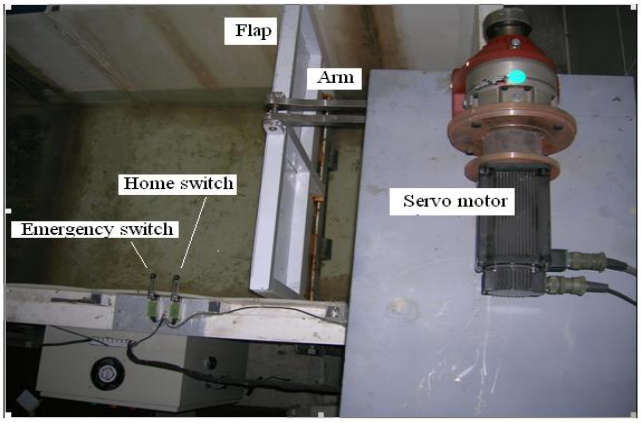

Figure 3. Hinged wave maker: (a) Schematic figure, (b) The hinged wave maker used in this research

Figure 4. Total view of the wave flume in the hydraulic laboratory

2.4. Generation and wave mapping

The JONSWAP spectrum input data is fed into the wave generator software via an input file, causing the paddle to initiate movement. However, as the numerical data may contain minor random fluctuations on the spectrum curve, generating these insignificant movements on the pedal is not feasible, and they must be eliminated. Consequently, a suitable filter is applied to the curve to remove any irregularities. The process of wave generation can be broken down into three simple steps, as illustrated in figures 5 and 6.

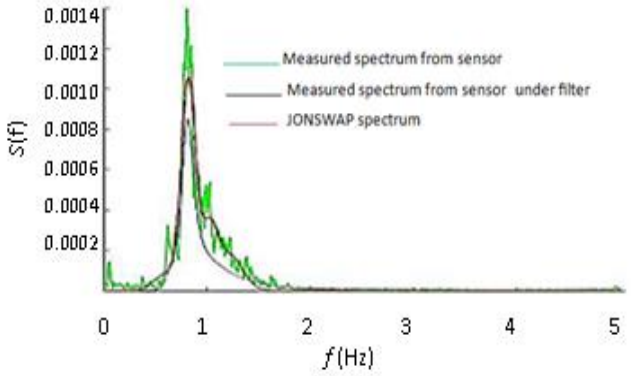

Figure 5. Primary spectrum (measured, filtered, and theoretic)

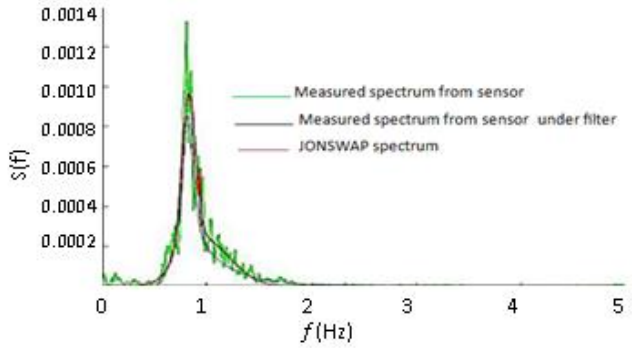

Figure 6. Modified spectrum (measured, filtered and theoretic)

-Generation of the primary wave based on the DSA numerical model and obtaining the spectrum resulting from the data mapped from sensor 1(MOD0).
-Modification of the obtained spectrum from step 1 according to the theoretic spectrum (MOD1).
-Repetition of step 2 in order to reduce the difference between the obtained spectrum and the theoretic spectrum (MOD2, 3).

2.5. Strain gauge

Strain gauges are TML Metal E-101R used for measuring flexural anchors as half-bridge. The sampling scope for the strain gauge varies from zero to 100Hz. Since the wall oscillation is faster than the water surface oscillation, thus it is necessary to pay attention to it in selecting the wall response sampling frequency to prevent the undesired problem of aliasing. In this research, the strain sampling frequency is 50Hz [20]. The manner of connection of the half-bridge and the details of the strain gauge are shown in Figure 7.

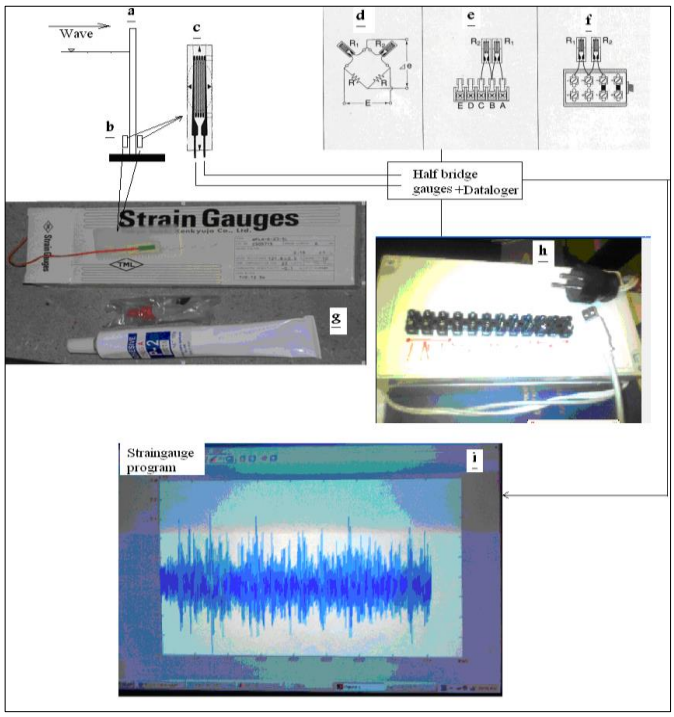

Figure 7. a) wall, b) place of the strain gauge on the wall, c) strain gauge schematic view, d) half-bridge connection to the unilateral data logger, e,f) strain gauge connection to the bilateral data logger, g) real image of strain gauge by special sticker, h) data logger, i) data images mapped from the strain gauge [20]

2.6. Experiments

Table 1 summarizes the experiments. The changes of the effective height are Hs from 3.9 to 9.2 cm, and peak frequency f_p ranges from 0.8 to 1.24 Hz. Table 1 presents the results of the five water level sensors used to measure fifteen waves in this study. For example, wave number 8 had a height of 5.4 cm and a peak frequency of 1.2 Hz at the water surface level, as indicated in the table. In this table H_s is significant wave height. To ensure accurate water level measurements in each experiment, mapping was performed from the still water surface and saved in separate files as time series data. Concurrently, strain gauges were installed on the wall to determine the pure strain caused by each wave. Consequently, for wave number 8, Table 3 and the strain gauge results corresponding to Table 2 were proposed. As the strain gauge was only installed on the wall, a time series file was created for strain measurements.

The wave absorber at the end of the channel is a metal mesh plate designed to absorb wave energy and prevent wave reflection. By absorbing the wave energy, it effectively eliminates the return wave and wave reflection.

Table 1. specifications generated random waves by JONSWAP spectrum based on the wave effective height and peak frequency

Number of Tests	H_s (cm)	Peak Frequency
1	5	0.8
2	5.2	1.24
3	5	1
4	5.6	1.23
5	7.3	1.22
6	3.9	1.23
7	5.4	1
8	5.4	1.2
9	4.3	1.23
10	7.7	1.21
11	6	1.23
12	7.5	1.23
13	9.2	1.23
14	5.6	1.24
15	7.5	1.21

Table 2. mappings for determining the wave from the water surface level sensors

Sensor	Water Surface Level	Water Static Surface Level
WP1 sensor	W1	W001
WP2 sensor	W2	W002
WP3 sensor	W3	W003
WP4 sensor	W4	W004
WP5 sensor	W5	W005

Table 3. mappings for determining the strain from the strain gauge built on the wall

Sensor	Strain File Name	The Strain File Name for Wall Still State
SG1	E1	E

2.7. Artificial neural networks modeling

Artificial neural networks have become increasingly prevalent in various fields, including engineering. In hydraulic engineering, the backpropagation algorithm is commonly utilized. Recent research has demonstrated that using a three-layer backpropagation algorithm can yield promising outcomes for prediction and simulation purposes in this field [21]. In this section, the neural network modeling was done based on the time series mapped from the experiments. Based on the research, the interaction between the wall and random waves is being studied. In this context, the water level time series are considered as input data, while the strain time series is considered as output data. The purpose is to analyze and understand the relationship between the wall and the waves, with a focus on measuring the strain and pressure exerted by the waves on the wall. Hence, changes in the water surface level can investigate the strain and pressure changes.

2.8. Network structure

Figure 7 depicts the feed-forward neural network with a backpropagation algorithm. This structure has been used in predicting the engineering works time series and is employed in this research. Based on this structure, nonlinear mapping is done between the input and output values. The feed-forward method is achieved based on the linear combination of the input

values leading to a nonlinear function. In Figure 8, i is related to the input layer, % is associated with the middle layer, j relates to neurons output, and k is the weight of the neurons in the feed-forward method, the connection among the neurons is done only by the middle layer. Equation (5) depicts the network output.

$$\hat{y}_k = f_0\left[\sum_{j=1}^{M} w_{kj}.f\left(\sum_{i=1}^{N} w_{ji}.x_i\right) + w_{j0}\right] \quad (5)$$

Where w_{ji} is the middle layer between neuron i from the input layer and neuron j from the middle layer, w_{j0} is the bios of neuron j , and f_h is the actuator function of the middle layer, w_{kj} is the output layer weight between neuron k from the output layer and j from the middle layer, f_0 is the actuator function for the output neuron, x_i is the input value in the input layer, $\hat{y}$ and y are the calculative and observation output values. The weights values differ in the middle and output layers and change in the network phase. The selective actuator functions are sigmoid logarithmic. The time series used in neural networks are normalized. Since these experimental data are related to some waves, they will be as positive and negative. Thus, this issue should be considered in their normalization. In the chapter on the analysis of the normalized form, the division of the time series was used as the maximum absolute value of the data in the time series. The data are used in this section based on this normalized method. On the other hand, applying this method is simple and common in engineering works [21].

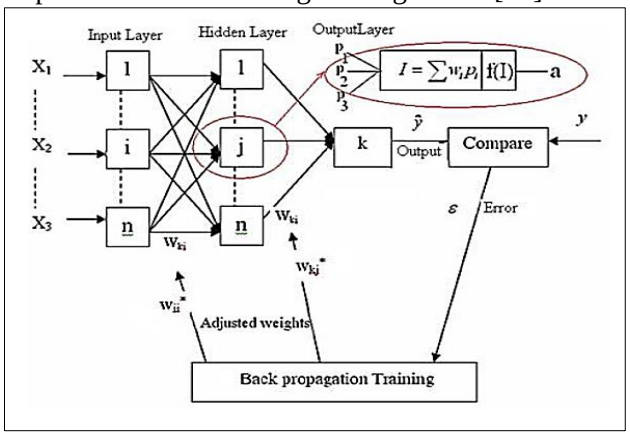

Figure 8. feed-forward neural network structure with the backpropagation algorithm with three layers [21]

2.9. Neural networks model

Various techniques are available for training and validating neural networks. A widely adopted approach for validation involves selecting one-third of the input and output time series from the beginning and one-third from the end [21]. The training process involves creating a model, and based on the model, the validation is predicted. To assess the quality of the network, regression coefficients are calculated for both the training and validation phases. The coefficient of determination, as expressed in equation (6), indicates how well the model performs, with a value closer to one indicating better performance. The Root Mean Square Error coefficient, as expressed in equation (7), is another metric used to evaluate model performance, with values closer to zero indicating superior performance.

$$R^2 = 1 - \frac{\sum_{i=1}^{N}(E_i - \hat{E}_i)^2}{\sum_{i=1}^{N}(\hat{E}_i - \overline{E})^2} \quad (6)$$

$$RMSE = \sqrt{\frac{\sum_{i=1}^{N}(E_i - \hat{E}_i)^2}{N}} \quad (7)$$

R^2, $RMSE$, N, E_i and $\overline{E}$ are coefficient of determination Root Mean Square Error, number of observations, strains obtained in the experiment (prediction values), and the average of strains related to the strain time series [22].

3. Results and discussion

If the time series of the water surface level is shown with W_t and the strain time series is depicted by E_t, the third-fourth W_t is considered as the training input from the beginning and one-fourth W_t, as verification input from the end, and one-fourth E_t as verification output from the end. Table 4 summarizes the values of the coefficient of determination in the training section (R_t^2) and verification (R_v^2) based on the network architecture. The network architecture inserts the input, middle, and output neurons. For instance, the (2-1-3) is meant the number of input neurons 2, central neuron 1 and output neuron 3. As is seen from Table 4, after 200 repetitions with network architecture of (1-5-1), the coefficients of determination are constant. Thus, R_t^2=0.7699, R_t^2=0.7743 are considered as coefficients.

Table 4. Results of BP-FFNN model in prediction of the water surface level strain

ANN architecture	epoch	R_v^2 (Calibration)	R_t^2 (Training)
1-2-1	50	0.7683	0.7681
1-2-1	100	0.7686	0.7688
1-2-1	150	0.7686	0.7701
1-2-1	200	0.7690	0.7710
1-2-1	250	0.7690	0.7710
1-2-1	300	0.7690	0.7710
1-2-1	400	0.7690	0.7710
1-2-1	500	0.7690	0.7710
1-3-1	200	0.7692	0.7713
1-4-1	200	0.7695	0.7731
1-5-1	**200**	**0.7699**	**0.7743**
1-6-1	200	0.7699	0.7743
1-7-1	200	0.7699	0.7743
1-5-1	300	0.7699	0.7743

Figure 9 shows the experimental and calculation results of water surface level strain prediction of the neural network model. Figure 9 depicts the regression curve for training, verification, and water surface level strain prediction. The obtained conversion coefficients for

training and verification depict better performance of the neural network models.

Figure 9 shows the experimental and calculation results of water surface level strain prediction of the neural network model.

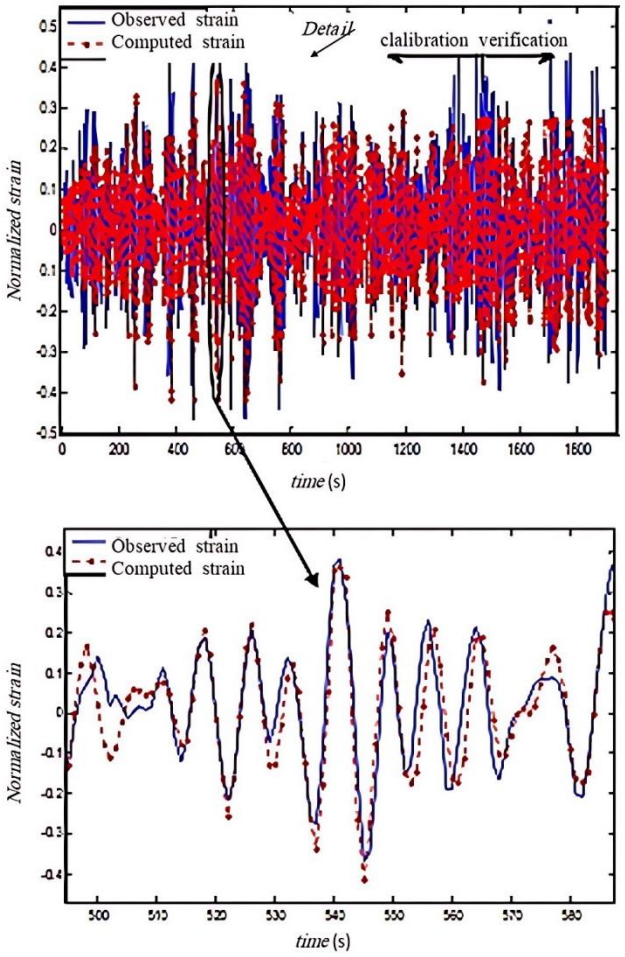

Figure 9. experimental and calculation results of strain prediction

Figure 10 depicts the regression curve for training, verification, and predicting water surface level strain. The obtained conversion coefficients for training and verification depict better performance of the neural network models. If there is a linear curve between time series y_t and the same time series with a step backward y_{t-1}, the first-grade self-correlation is established, and if there is a linear curve between y_t, and y_{t-2}, the second-grade self-correlation is established, and this trend is continued if the inputs x_t, and output y_t, are assumed, according to the Markov chain of rules, can be used for the prediction of the time series of first-grade Markov y_t, $X_t = \begin{bmatrix} x_t \\ y_{t-1} \end{bmatrix}$ and for second grade Markov $y_t, X_t = \begin{bmatrix} x_t \\ y_{t-1} \\ y_{t-2} \end{bmatrix}$ that provide better results relative to $X_t = [x_t]$. Because the behavior is not completely linear, all cases are usually considered in prediction. In Figure 11, the curve between E_t and E_{t-1} has been drawn and $R^2 = 0.5998$ was achieved, and Figure 12 shows $R^2 = 0.0122$ between E_t and E_{t-2}. Thus, the date on the strain time series is first-grade Markov.

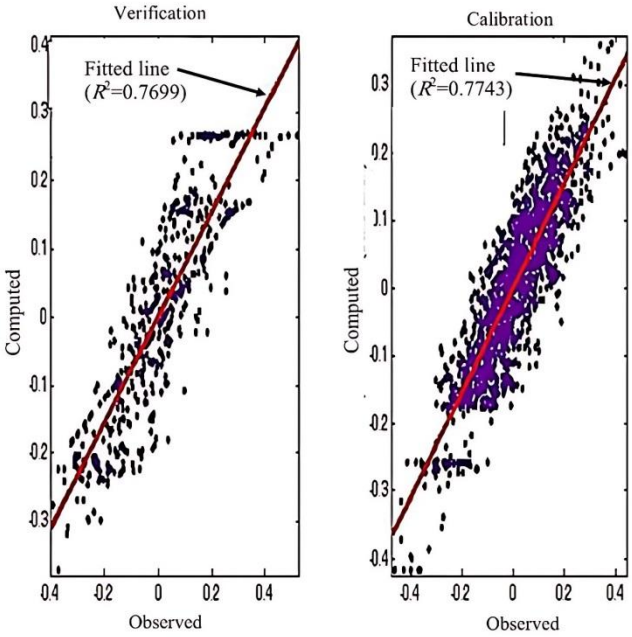

Figure 10. regression curve for training, verification, and water surface level strain prediction

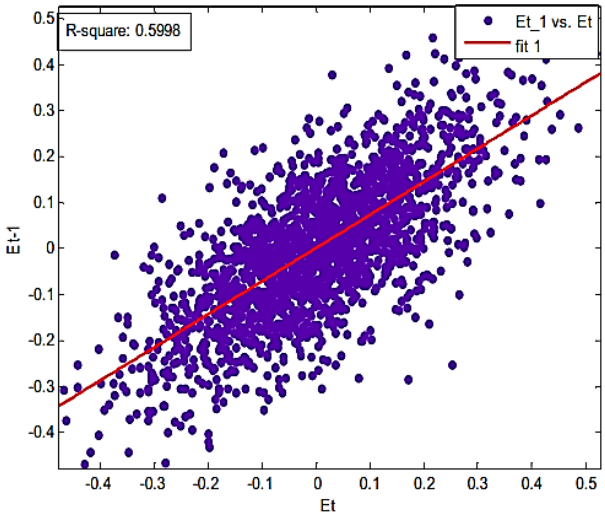

Figure 11. linear regression between E_t and E_{t-1}

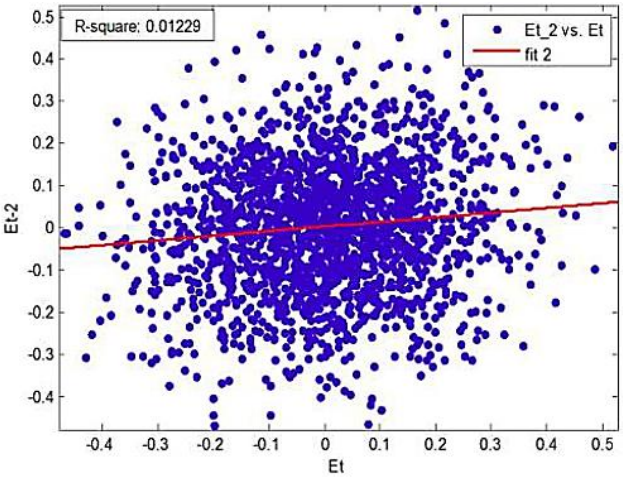

Figure 12. linear regression between E_t and E_{t-2}

The results of the neural network model are shown according to Table 5, considering first and second-grade Markov equations for strain and pressure. In these tables, it is seen that the value of R2 is increased by considering the first-grade Markov. On the other hand, in the case that $\begin{bmatrix} W_t \\ E_{t-1} \end{bmatrix}$ is considered in determining input strain instead of [W_t], the value of R^2 increases from 0.7773 to 0.8109.

Table 5. Results obtained from BP-FFNN model in prediction of strain from water surface level

Input	Output	ANN architecture	epoch	R_v^2 (Calibration)	R_t^2 (Training)
$[W_t]$	E_t	1-5-1	200	0.7699	0.7743
$\begin{bmatrix} W_t \\ E_{t-1} \end{bmatrix}$	E_t	**2-8-1**	**250**	**0.8418**	**0.8109**
$\begin{bmatrix} W_t \\ E_{t-1} \\ E_{t-2} \end{bmatrix}$	E_t	3-9-1	250	0.6536	0.6395

4- Conclusion

The present study aimed to investigate the behavior of quay walls under the influence of random waves, using experimental methods. Vertical geometrical form walls were exposed to sea waves with JONSWAP spectrum, and their surface level and wall strain values were measured using built-in sensors. The study utilized a neural network model, which employed the feed-forward method with the backpropagation algorithm. The model used time series data of water surface levels and strains to predict their behavior. Finally, the following results can be mentioned:

- The results of the study showed that the high conversion coefficients in the training and verification phases of the artificial neural networks modeling indicate better network performance.

The BP-FFNN model was able to predict the water surface level strain, and the best ANN architecture was (1-5-1), with epoch 200 and coefficients of determination Calibration and Training of 0.7743 and 0.7699, respectively, which are acceptable coefficients.

- The data on the series showed first-grade self-correlation (first-grade Markov) between water surface level and wall strain.
- The best ANN architecture was (2-8-1), with epoch 250 and coefficients of determination Calibration and Training of 0.8418 and 0.8109, respectively. Moreover, the first-grade Markov performed better than higher grades of Markov.

5. References

[1] Vafaeipour Sorkhabi, R., Naseri, A., Alami, M. T., and Mojtahedi, A. (2022), *Experimental Study of an Innovative Method to Reduce the Damage of Reshaping Rubble Mound Breakwaters*, Innovative Infrastructure Solutions, 7(6), 353.

[2] Alami, M. T., Vafaeipour Sorkhabi, R., Naseri, A., and Mojtahedi, A. (2022), *Enhancing Stability and Reduce Damage in Rubble-Mound Reshaping Breakwaters by Using Obstacles in Front of the Structure*, Civil Infrastructure Researches, 7(2), 33-49.

[3] Vafaeipour Sorkhabi, R., and Naseri, A. (2021), *Experimental Investigation of Optimal Slope Determination of Seawalls Subjected to Random Sea Waves based on Base Shear and Overturning Moment*, Amphibious Science and Technology, 2(3), 37-49.

[4] Vafaeipour Sorkhabi, R., and Naseri, A. (2019), *Experimental Investigation of the Interaction Between Vertical Flexible Seawall and Random Sea Waves*, Journal of Advanced Defense Science & Technology, 6(3): 155-162.

[5] Sainflou, G., (1928), *Essai sur les digues maritimes verticals*. Annales de ponts et chaussées, 98(1), 5-48.

[6] Rundgren, L., (1958), *Water wave forces : a theoretical and laboratory study*, Bulletin 549 Royal Institute of Technology, Division of Hydraulics, Stockholm, Sweden.

[7] Minikin, R., (1950), *Wind Waves and Maritime Structures: Studies in Harbor Making and in Protection of Coasts*, Charles Griffin & Company, London, 224-304.

[8] Goda, Y., (2010), *Random Seas and Design of Maritime Structures*, Advanced Series on Ocean Engineering, World Scientific.

[9] Vijayakrishna, E., Natarajan, and R., Neelamani, S., (2004), *Experimental Investigation on the Dynamic Response of a Moored Wave Energy Device under Regular Sea Waves*, Ocean Engineering, 31(5): 725- 743.

[10] Hughes, S.A., (2004), *Wave momentum flux parameter: A Descriptor for Near Shore Waves*, Coastal Engineering, 51(11): 1067-1084.

[11] Neelamani, S., Jawguei, L., and Shangchun, C., (2010), *An Experimental Study of Wave Forces on Vertical Breakwater*, Journal of Marine Science and Technology, 15(3): 158-170.

[12] Cumo, G., Allsop, W., and Takahashi, S., (2010), *Scaling Wave Impact Pressures on Vertical Wall*, Coastal Engineering, 57 (6): 604-609.

[13] Vafaeipour Sorkhabi, R., Alami, M., Naseri, A., and Mojtahedi, A. (2022), *Experimental Analysis of the Effect of a Submerged obstacle and Floating Wave Barrier in front of a Rubble Mound Breakwater on Diminishing the Damage Parameter*, International Journal of Coastal, Offshore and Environmental Engineering, 7(2), 39-48.

[14] SPM, (1984), *Shore protection manual*, Coastal Engineer's Research Center, U.S Army corps.

[15] Osgouei, A. D., Poursorkhabi, R. V., Maleki, A., and Ahmadi, H. (2021), *Effects of a Floating Wave*

Barrier with Square Cross Section on the Wave-induced Forces Exerted to an Offshore Jacket Structure, Ocean Systems Engineering, 11(3), 259-274.

[16] Naseri, A., Sorkhabi, R. V., Alami, M. T., and Mojtahedi, A. (2022), *Damage Parameter Variations of Breakwater along with a Floating Wave Barrier and a Submerged Obstacle*, International Journal of Sustainable Construction Engineering and Technology, 13(1), 202-217.

[17] Vafaeipour, R., Lotfollahi, M., and Aminfar, M., (2011), *The Effect of Random Waves Period on Coastal Wall Reaction with Various Geometrical Shapes with Numerical Method*, Journal of Oceanography, 8, 69-78.

[18] Sorensen, R.M., (1993), *Basic Wave Mechanic for Coastal and Ocean engineering*, Jon Wiley.

[19] Alami, M., Vafaeipoor, R., Naseri, A., Mojtahedi, A. (2022), *Experimental Analysis of the Effect of the Distance of a Submerged Berm in front of a Reshaping Rubble Mound Breakwater on Diminishing the Damage Parameter*, Journal of Civil and Environmental Engineering, 52.2(107), 1-13.

[20] Strain Gauge TML Pam E-101R, (2012), Sokki Kenkyujo Company, Ltd. Tokyo.

[21] Nourani, V., komasi, M., and Mano, A., (2009), *A Multivariate ANN - Wavelet Approach for Rainfall Runoff Modeling*, Water Recourse Management, 36,1251-1257.

[22] Motamedi, H., Rahbani, M., Harifi, A., and Ghaderi, D. (2020). *The choice between Radial Basis function and Feed Forward Neural Network to predict long term tidal condition.* International Journal of Coastal, Offshore And Environmental Engineering, 5(1), 1-9.

INTERNATIONAL JOURNAL OF
COASTAL, OFFSHORE & ENVIRONMENTAL ENGINEERING IJCOE Vol.8/No. 4/Autumn 2023 (9-17)

Available online at: www. Ijcoe.org

Sensitivity Analysis of Makran Subduction Zone's Seismic Parameters for Optimizing the Number of Potential Tsunami Scenarios

Ehsan Rastgoftar[1*], Ali Khoshkholgh[1], Mahmood Reza Akbarpour Jannat[1]

[1] Iranian National Institute for Oceanography and Atmospheric Science, Tehran, Iran,
Corresponding author:e.rastgoftar@inio.ac.ir

ARTICLE INFO

Article History:
Received: 06 Sep. 2023
Accepted: 19 Sep. 2023

Keywords:
Tsunami
Makran Subduction Zone
Earthquake Magnitude
Dip Angle
Rake angle

ABSTRACT

Given the necessity of knowing the probability and risk of future tsunamis in actions related to tsunami hazard mitigation, the Probabilistic Tsunami Hazard analysis (PTHA) approach has been accepted as the basis for tsunami risk assessment studies for high-risk areas such as the Makran region. Considering the uncertainties associated with fault parameters and the random nature of earthquake occurrence in PTHA, simulation a large number of potential tsunami scenarios is required in future tsunami studies of the Makran Subduction Zone (MSZ). In order to optimize the number of scenarios in these studies, appropriate values for the ranges and change intervals of some uncertain seismic parameters in different scenarios are determined in the present study. For this, the values used in previous studies for earthquake magnitude and depth as well as dip and rake angles of MSZ's tsunamigenic earthquakes are investigated; and the effects of variations in these parameters on the tsunami waves are evaluated through numerical modeling based on non-linear shallow water equations and sensitivity analysis.

The obtained results show that a minimum value of Mw0.1 for the interval of earthquake magnitude variations must set in developing potential tsunami scenarios for the Makran region. Also, considering two or three values in the range of 2º to 20º and 10 km to 30 km, respectively, as probable values for the dip angle of the subduction zone and the depth of tsunamigenic earthquakes seems sufficient. However, if the minimum number of scenarios is desired, selecting a unit value for the dip angle in the range of 10º to 15º and a constant earthquake depth of 10 km can be acceptable. Also, for rake angle a constant value of 90º can be considered in different scenarios.

1. Introduction

Tsunamis, despite their infrequent occurrence, are considered one of the greatest threats to human communities. According to available statistics, the 2004 Indian Ocean tsunami, with over 220,000 human casualties, remains the deadliest natural disaster of the present century by a large margin. The list also includes the 2011 Tohoku tsunami and 2018 Sulawesi tsunami. The significant loss of life and property damage associated with tsunamis makes them a high-risk event, despite their low probability. Therefore, understanding and assessing tsunamis and preparing for them is of utmost importance and special attention in coastal areas at risk.

Although any factor that suddenly displaces a large volume of seawater falls among the sources of tsunami (like landslide, volcanic activity …), the earthquakes resulted from the subduction of tectonic plates are recognized as the most common cause of tsunamis. According to "Global Historical Tsunami Database" [1] from 1900 to the present, more than 80% of potential tsunamis have been triggered by earthquakes. Among the earth's subduction zones, the Makran Subduction Zone (MSZ) is known as s susceptible region for generating tsunamis in the Indian Ocean (along with the Sunda subduction zone). Formed as a result of the collision of the Arabian plate with the Eurasian plate, this zone extends approximately 900 kilometers along the northwest of the Indian Ocean, adjacent to the southern coasts of Iran and Pakistan. The available evidences suggest fewer huge earthquakes in the Makran region compared to other subduction zones; however several significant earthquakes and tsunami events have been reported in this area. The most notable of these is the earthquake

and accompanying tsunami in 1945, which caused the death of over 4,000 people totally [2].

Before 2004, the occurrence of tsunamis in the Sunda subduction zone (at least its northern part) was considered unexpected, mostly because of the lack of historical data related to large earthquakes during the past 200 years. Following the occurrence of the massive earthquake and tsunami in 2004, more detailed studies revealed evidence of large tsunamis in the 1000-year-old sediment layers [3]. A similar situation could be true for the Makran region, especially in relation with its western part, which has showed lower seismic activity compared to the eastern part and has not experienced a major earthquake in recent centuries (at least in the past 600 years) [4].

Numerous studies have been conducted regarding the assessment of tsunamis in the Makran region. These studies initially focused on the modeling of the 1945 tsunami (or similar tsunamis) [5, 6, 7, 8, 9, and 10]. Subsequently, another category of studies formed, based on a deterministic analysis approach, in which limited and specific scenarios of potential earthquakes and tsunamis (mostly worst-case scenarios) were simulated [11, 12, and 13]. In recent years, a new series of studies has emerged to determine the probability of tsunami intensity, using a probabilistic tsunami hazard analysis (PTHA) approach [3, 14 and 15]. In these studies, by estimating earthquake occurrence rates, all possible tsunami scenarios, ranging from small to large events, along with all estimable uncertainties, are considered to assess tsunami risk.

Considering the need for probabilistic assessment and risk estimation of future tsunamis in decision-making processes related to tsunami hazard mitigation [16], PTHA studies for tsunami-prone regions is essential. For example, according to the American loading standard (ASCE/SEI 7-16), which can be considered the most comprehensive reference for considering the effects of tsunamis in structural design, the "design tsunami" is defined as an event with a 2% probability of being exceeded in a 50-year period and it should be determined based on a site-specific probabilistic tsunami hazard analysis approach [17].

In the PTHA approach all tsunami sources and uncertainties associated with tsunamis are usually considered through the implementation of a logic tree approach. The existing uncertainties, containing epistemic uncertainties related to fault parameters and aleatory uncertainties related to the random nature of earthquake occurrence and the inability to predict their magnitude and location, lead to the creation of various nodes in the developed logical tree. As a result, the PTHA approach involves simulating a large number of defined scenarios, the number of which reaches thousands depending on the diversity of uncertain parameters and the intervals for their values.

It should be noted that the necessity of simulating a large number of possible tsunami scenarios in the Makran region does not only include PTHA-related studies. Since the MSZ is located on the margins of the Indian Ocean at a very short distance from the coasts, it is a nearfield tsunami source for many neighboring countries such as Iran, Pakistan, Oman, and India. Its possible earthquakes can occur in close proximity to coastal areas or even inland. This means that the resulting tsunamis will reach the coasts of neighboring countries within a very short time interval (between 20 minutes to 1 hour), which makes the tsunami warning process very difficult. Therefore post-event tsunami simulation is not feasible for tsunami warning centers, and it is essential to have comprehensive databases extracted from pre-simulated probable tsunami scenarios available at these centers.

It is obvious that simulating a very large number of tsunami scenarios is computationally and time-intensive and is not desirable. What causes the multiplicity of these scenarios is the variations in the uncertain values of fault parameters and the random information related to the magnitude and location of earthquakes in different scenarios. In order to prevent unnecessary growth in the number of scenarios, the mentioned parameters variations should occur within the range of real and logical values. Furthermore, the steps of changes should be optimally selected in a way that excessive small steps do not cause the number of scenarios to increase unnecessarily. At the same time, it is necessary to avoid applying large change intervals leading to missing scenarios with serious differences.

With the aim of preventing the simulation of an excessive number of tsunami scenarios in future studies of tsunami assessment in the MSZ, in the present study suitable values for the range and steps of changes for some seismic parameters in different scenarios are determined. For this purpose, firstly the proposed or applied values for earthquake magnitude and depth as well as dip and rake angles of MSZ's tsunamigenic earthquakes in previous studies are investigated. Then, the effects of variations in these parameters on the subsequent tsunamis are evaluated through numerical modeling and sensitivity analysis. In the numerical modeling, the initial tsunami wave is generated using Okada's rectangular elastic half-space model [18]; the wave propagation is calculated based on the nonlinear shallow water equations solved in a nested grid model domain centered on the Chabahar Bay area. Finally, the tsunami wave height in the vicinity of the bay is evaluated as a sensitivity parameter for simulation.

2. Uncertain Seismic Parameters

For the modeling of seismic tsunamis, the occurrence of the earthquake is usually considered instantaneous and the temporal changes of ground deformation are disregarded. Thus, the generated seabed displacement is identically transferred to the water free surface providing the initial tsunami wave. Among the several algorithms have been proposed to calculate the seabed

dislocation, the Okada's half-space elastic method [18] is used in the intended numerical model. In this method, the deformation of the seabed is calculated using analytical stress-strain relationships and earthquake source parameters including fault length, fault width, slip amount on the fault surface, dip angle, strike angle, rake angle, and focal depth. Among these parameters, the surface rupture length (L), down-dip rupture width (W), and slip amount on the fault surface (Δ) are directly dependent on the earthquake magnitude. The empirical relationship between seismic moment (M_0) and moment magnitude (M_w) (Eq.(1)), along with the seismic moment formula connecting the released energy of the earthquake to the product of the fault surface area, average slip in the fault zone, and the rigidity of the earth (Eq.(2)), indicates the dependency.

$$M_w = \frac{2}{3} log_{10}^{(M_0)} - 6 \quad (1)$$

$$M_0 = \mu \Delta L W \quad (2)$$

Despite the advancements in human knowledge, it is still not possible to accurately predict the magnitude and location of future earthquakes. Possible earthquakes can occur at any point along the fault or subduction zone with different magnitudes and dimensions. Therefore, within probable tsunami scenarios for each region earthquakes with different magnitudes are considered, and accordingly, the parameters of fault length, width, and slip also vary. The depth of earthquake is another uncertain seismic parameter, which cannot be predicted for future events and varies in the earthquake and tsunami scenarios. Other required seismic parameters, such as the dip, slip, and strike angles within a specific subduction zone, like the Makran region, change within a limited range. Although some studies on the structure and geology of MSZ have been started in recent years (e.g.[19]), the precise values of the dip and rake angles for the Makran region have not been completely clear, and different numbers have been reported for them in various sources. Therefore, based on previous studies, the magnitude and depth of MSZ's potential earthquakes, as well as possible values for the dip and rake angles, are investigated, and the appropriate values are obtained for sensitivity analysis of these parameters.

3.1. Earthquake Magnitude

The earthquake magnitude is the most important variable parameter in tsunami scenarios, as it affects other dependent parameters such as fault length, fault width, and slip amount on the fault surface. Subduction earthquakes with magnitudes less than Mw7.5 usually do not generate tsunamis [20]. Earthquakes smaller than this value (up to Mw6.5) may only cause slight changes in sea level near the epicenter. On the other hand, the largest probable earthquake in seismic regions is determined based on seismicity and tectonic characteristics. Different values have been reported as the largest probable earthquake in the MSZ. Employing the instrumental earthquake catalogues, due to their short time period, underestimates the maximum magnitude [15]. Based on the dependency of the largest expected earthquake on the length of the continuous fault system along the convergent plate boundary, a moment magnitude Mw 9.0 earthquake, corresponding to full rupture of the plate boundary, was considered as the largest tsunami source in the Makran region [11]. According to the MSZ's approximate length of 900 kilometers, the occurrence of earthquakes up to Mw8.8 was found also possible [21]. Moreover, thermal modeling results indicate the potential of MSZ for generating earthquakes ranging from Mw8.7 to Mw9.2 [22]. Therefore, to cover all potential tsunami-generating earthquakes (in terms of magnitude), in sensitivity analysis scenarios the magnitude of earthquake varies between Mw7 and Mw9 at intervals of 0.1. According to empirical relationships of Wells and Coppersmith [23], the length, width, and slip of a fault vary in proportion to the earthquake magnitude. However, considering the formula between seismic moment and moment magnitude (Eq.(1)) and the equation for seismic moment (Eq.(2)), the predicted values are slightly modified. Table 1 shows the changes in earthquake magnitude and its related parameters during the sensitivity analysis. It is obvious that other seismic parameters are assumed to be constant during this analysis (Table 2).

Table 1. Variation of earthquake magnitude and related parameters during sensitivity analysis

Moment magnitude	Fault length (km)	Fault width (km)	Fault slip (m)
Mw 7.0	40	20	1.11
Mw 7.1	50	20	1.25
Mw 7.2	60	20	1.47
Mw 7.3	70	20	1.79
Mw 7.4	80	20	2.21
Mw 7.5	90	20	2.77
Mw 7.6	110	30	2.14
Mw 7.7	120	30	2.76
Mw 7.8	150	30	3.12
Mw 7.9	170	30	3.89
Mw 8.0	200	40	3.51
Mw 8.1	230	40	4.31
Mw 8.2	270	40	5.18
Mw 8.3	320	40	6.18
Mw 8.4	380	50	5.88
Mw 8.5	440	50	7.17
Mw 8.6	520	60	7.14
Mw 8.7	600	60	8.74
Mw 8.8	710	60	10.44
Mw 8.9	830	70	10.81
Mw 9.0	980	70	12.93

Table 2. The values of fixed seismic parameters for sensitivity analysis

Sensitivity analysis seismic parameter	Fixed seismic parameters							
	Earthquake magnitude	Fault length	Fault width	Fault Slip	Dip angle	Rake angle	Earthquake depth	Strike angle
Earthquake magnitude	---	---	---	---	8º	90º	5 km	270º
Dip angle	Mw 8.7	600 km	60 km	8.74 m	---	90º	5 km	270º
Rake angle	Mw 8.7	600 km	60 km	8.74 m	8º	---	5 km	270º
Earthquake depth	Mw 8.7	600 km	60 km	8.74 m	8º	90º	---	270º

3.2. Dip Angle

Dip angle of a subduction zone, presenting the angle between the oceanic plate and the continental plate, describes the contact between the two tectonic plates according to the geometry of contact surface. With regards to increase in curvature of the contact area of the two plates with increasing depth, the dip angle of a subduction zone is not constant and usually grows with the depth of the earthquake. Due to the low level of seismic activity in the MSZ and limited data on past earthquakes, there is not accurate information regarding the dip angle and its variations with depth. In a study by Byrne et al. [24] on some earthquakes in the Makran region, the estimated dip angle values range from 7º to 27º (Table 3). According to the estimated value of 7º for the dip angle of the 1945 earthquake, many studies related to simulating the tsunami in the MSZ have used 7º as the dip angle [6, 9, 11, 25, and 26]. However, other values such as 10º [27] and 3º [28] have also been considered. Rashidi et al. [3] in modeling of Makran's potential tsunamis, set the dip angle range between 2º and 8º; maybe based on the results obtained from seismic reflection profiles along the MSZ indicating a relatively small dip angle between 2º and 8º [29]. With regard to the aforementioned points, for the sensitivity analysis of the dip angle the range of this parameter is considered to be 2º and 20º (in 3º degree intervals). The values of other seismic parameters are provided in Table 2.

Table 3. Seismic parameters of Makran earthquakes [24]

Date	Latitude (ºN)	Longitude (ºE)	Dip angle (º)	Rake angle (º)	depth (m)
Nov.27 1945	25.15	63.48	89	7	27
Aug.5 1947	25.04	63.49	68	7	20
Sept.1 1962	25.60	65.22	80	10	18
Feb.13 1969	24.99	62.75	84	9	18
Aug.6 1972	25.04	61.22	114	22	33
Aug.18 1972	24.83	63.14	84	9	20
Sept.2 1973	24.88	63.21	70	23	18
July 29 1975	25.22	63.09	88	27	18

3.3. Rake angle

The rake angle determines the movement of a fault relative to its strike, where values of 0º and 90º respectively represent strike-slip faulting and dip-slip faulting. Usually dip-slip faulting, by creating vertical displacement in the seafloor, leads to the formation of tsunami. A study of 36 earthquakes that generated tsunamis in different subduction zones shows that their average rake angle is approximately 91º [30]. However, full dip-slip faulting is rare in nature, and dip-slip faults often also have a component of strike-slip motion. According to Table 3, the estimated rake angle for dip-slip earthquakes in the MSZ varies between 68º and 114º. Considering the estimated value of 89º for the rake angle of the 1945 earthquake, simulations of the MSZ tsunami usually adopt a value of 89º or 90º for this seismic parameter. However, other values such as 100º have also been considered in some studies [31]. Therefore, for sensitivity analysis, the rake angle in simulations ranges from 70º to 120º (in 10º intervals).

3.4. Earthquake depth

The typical depth of earthquakes that generate tsunamis is less than 30 kilometers [31]. Earthquakes with greater source depths cannot effectively transfer energy to the seafloor and are unable to cause significant displacement of the ocean bed. The average depth of the 36 studied tsunamigenic earthquakes is estimated to be around 25 kilometers [30]. Table 3 indicates that the estimated depth of the earthquakes in the Makran region is less than 33 kilometers. Considering the depth of 27 kilometers for the 1945 earthquake, simulations of the MSZ tsunamis often assume a quake depth of 25 kilometers. Based on the above, the range of source depth variations for sensitivity analysis is considered to be values less than 35 kilometers (in 5-kilometer intervals).

3. Numerical Modeling

Like the usual approach of tsunami simulation, the variations in the free surface elevation obtained from tsunami generation phase (initial tsunami wave) are introduced as initial conditions to the tsunami propagation equations. Since the wavelengths of seismic tsunamis (hundreds of kilometers) are much larger than the ocean depth (a few kilometers), their propagation is usually calculated using shallow water equations, which are the simplest type of depth-averaged wave equations. In the MOST model [32],

used as the numerical model in this study, non-linear shallow water equations (NSW) are employed, which are expressed in Cartesian coordinates as follows:

$$\frac{\partial(\eta+d)}{\partial t}+\frac{\partial(u(\eta+d))}{\partial x}+\frac{\partial(v(\eta+d))}{\partial y}=0 \quad (3)$$

$$\frac{\partial u}{\partial t}+u\frac{\partial u}{\partial x}+v\frac{\partial u}{\partial y}+g\frac{\partial(\eta+d)}{\partial x}=g\frac{\partial d}{\partial x} \quad (4)$$

$$\frac{\partial v}{\partial t}+u\frac{\partial v}{\partial x}+v\frac{\partial v}{\partial y}+g\frac{\partial(\eta+d)}{\partial y}=g\frac{\partial d}{\partial y} \quad (5)$$

where η represents the free surface elevation (tsunami wave height), d is the still water depth, g is the gravitational acceleration, and u and v are the mean velocities at depth in the x and y directions, respectively. Considering that tsunami waves may travel long distances on the order of hundreds or thousands of kilometers before reaching coastal areas, for a more accurate representation of wave propagation over this long distance, factors such as seabed topography and the Coriolis force are also taken into account in the MOST model. Additionally, the effects of wave dispersion, which are not seen in the NSW equations, are approximately considered in the MOST model by utilizing the inherent numerical dispersion of the finite difference method.

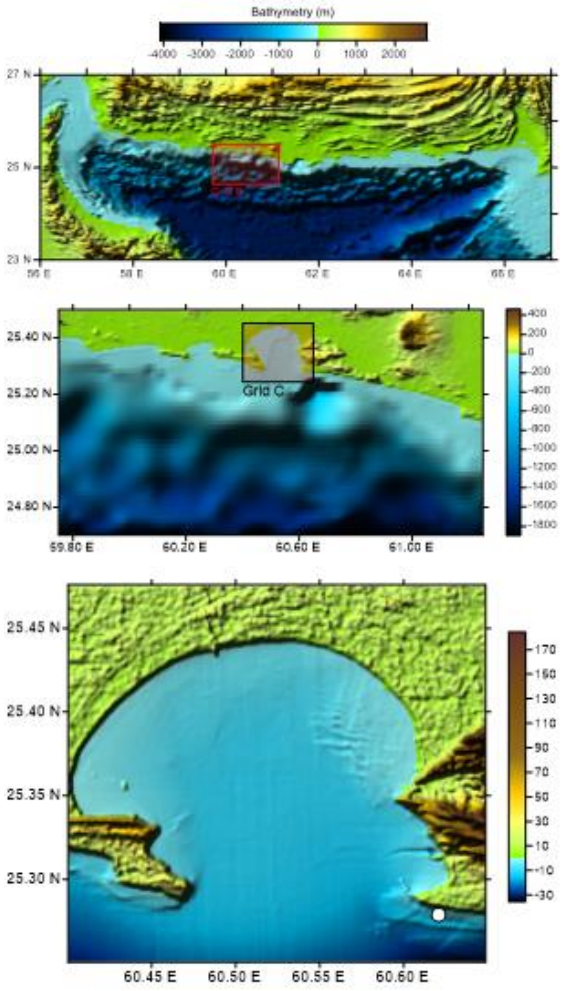

Figure 1. Values of hydrographic and topographic data of modeling grids; large-scale grid (top), intermediate grid (middle), coastal grid (bottom). The white circle indicates the position of the numerical wave station.

Due to the very long wavelengths of seismic tsunamis, considering computational points containing water depth information at distances apart (on the order of kilometers) may be sufficient for modeling tsunami generation and propagation in deep water. However, as the tsunami waves propagate towards the shore and the water depth decreases, the wavelength of the waves decrease. On the other hand, the impact of tsunami waves on coasts and the extent of run-up mainly depend on the complex effects of sea depth and coastal topography in the vicinity of the coastal region. Therefore, the governing equations for tsunami propagation (Eq.(3) to Eq.(5)) are solved here in a three-level nested grid model domain; moving from deep water toward the target coastal areas (Chabahar Bay) the grid resolution increases (Figure 1).

4. Results

In order to evaluate the results of sensitivity analysis, the wave height of the tsunami resulting from the simulations has been extracted at a point near Chabahar port (60.62º E - 25.28ºN) with a depth of approximately 50 meters (Figure 1). The recorded time series of waves during the sensitivity analysis of earthquake magnitude are shown in Figure 2 in two separate graphs (due to significant changes in tsunami wave height with earthquakes size). Also, Figure 3 shows the maximum recorded tsunami wave height for all earthquakes.

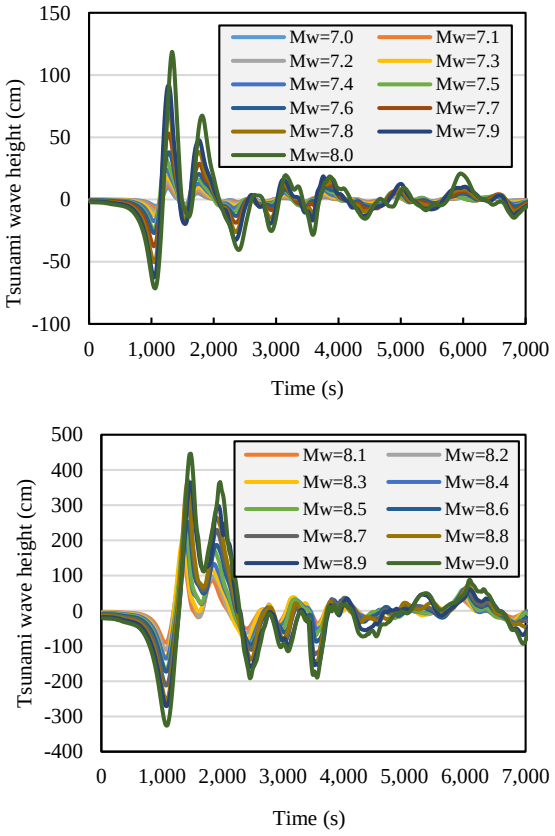

Figure 2. Time series of tsunami waves recorded during the sensitivity analysis of earthquake magnitude.

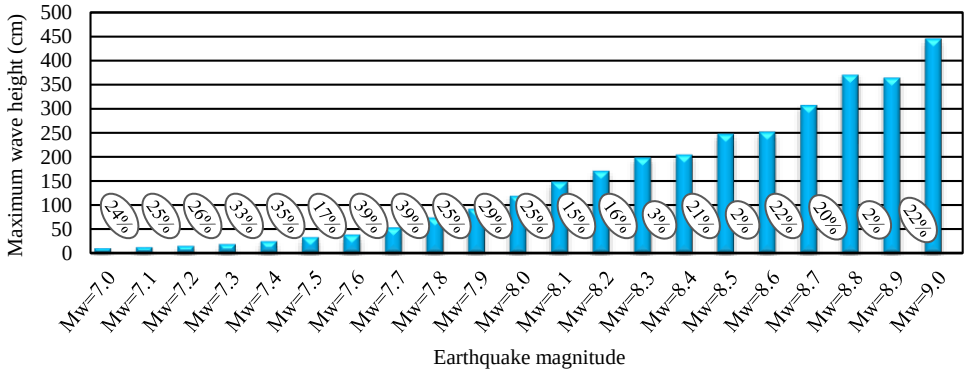

Figure 3. variation of maximum tsunami wave height with earthquake magnitude.
The numbers inside the circles indicate the amount of change in wave height between successive intervals of earthquake magnitude.

It is observed that, as expected, the height of the tsunami wave increases with the magnitude of the earthquake. However, as can be seen in Figures 2 and 3, this trend is violated in some cases, and the height of the waves does not always increase with the increase in earthquake magnitude.

By carefully examining Table 1, it can be realized that the main cause of this is mainly related to variations in the amount of slip in the scenarios. For example, between Mw8.5 to Mw8.6 and also Mw8.8 to 8.9 earthquake scenarios, the amount of slip does not increase significantly, and as a result, the calculated wave height does not rise significantly either. The source of this non-uniform trend is related to the way of determining the amount of slip in the scenarios; here, for each scenario, firstly the length and width of the fault was estimated according to the earthquake magnitude and the applied empirical relationships, and then the amount of slip was determined in such a way that the relationship between magnitude and earthquake moment (Eq.(1)) is satisfied. This has caused the amount of slip, which is a key parameter determining the height of tsunami waves, to not change proportionally with the earthquake magnitude in sensitivity analysis scenarios (Table 1). Another point is related to the pattern of tsunami wave propagation near the coast; due to the variation in fault size in different scenarios, the pattern of tsunami wave propagation also changes, which leads to wave reflection and amplification, and can cause larger waves for smaller earthquake scenarios.

The time series in Figure 4, corresponding to the sensitivity analysis of dip angle, demonstrate that with an increase in the of dip angle, the ocean floor uplift and subsequently the tsunami wave height increase. However, the tsunami height changes due to dip angle variation are not significant, as shown in Figure 5 (the numbers inside the circles). The maximum tsunami wave height varies by approximately 10% for successive scenarios with a 3º change in dip angle.

The variations of tsunami wave height with changes in the rake angle are shown in Figures 6 and 7. Based on the obtained results, the changes in tsunami height due to changes in the rake angle are very small (about 5%).

Additionally, as expected, the maximum tsunami wave height is observed during the rake angle of 90 degrees (full dip-slip faulting).

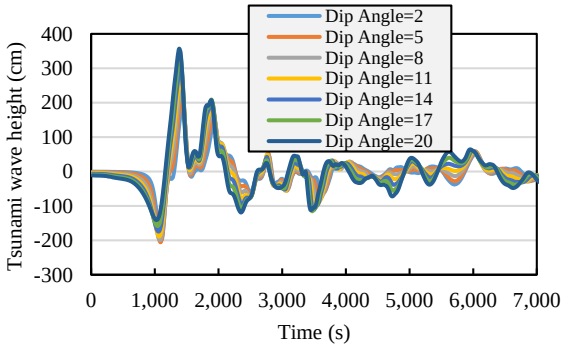

Figure 4. Time series of tsunami waves recorded during the sensitivity analysis of dip angle.

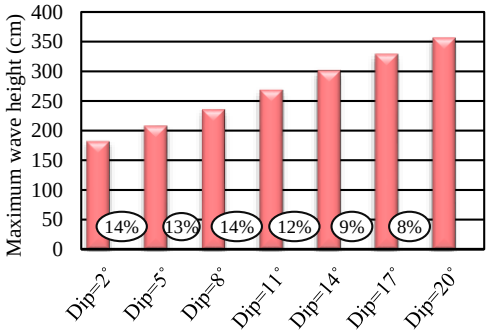

Figure 5. Variation of maximum tsunami wave height with dip angle. The numbers inside the circles indicate the amount of change in wave height between successive intervals of dip angle.

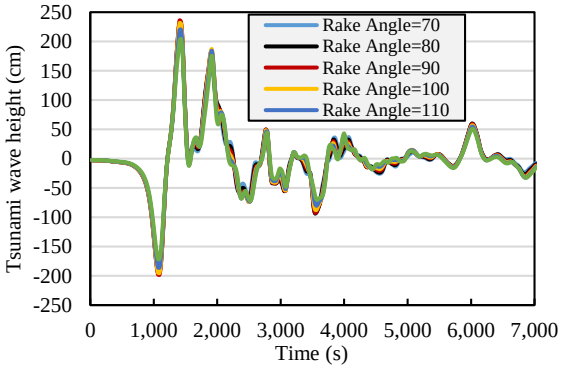

Figure 6. Time series of tsunami waves recorded during the sensitivity analysis of rake angle.

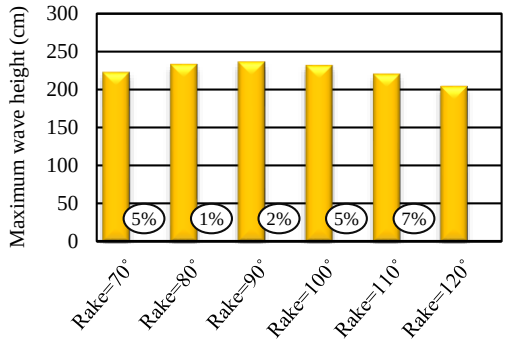

Figure 7. Variation of maximum tsunami wave height with rake angle. The numbers inside the circles indicate the amount of change in wave height between successive intervals of rake angle.

The simulation results related to the sensitivity analysis of the depth of the earthquake (Figures 8 and 9) indicate that although, as expected, with an increase in the focal depth, the displacement of the ground surface and subsequently the tsunami wave height decrease, but this trend is not accurate in the first step, meaning that a of 5-kilometer earthquake depth has resulted in smaller waves in comparison to a similar earthquake at a depth of 10 kilometers.

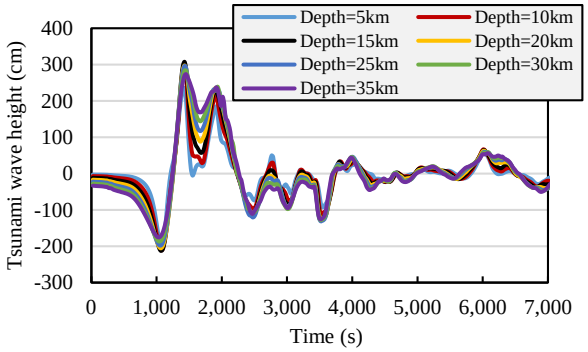

Figure 8. Time series of tsunami waves recorded during the sensitivity analysis of earthquake depth.

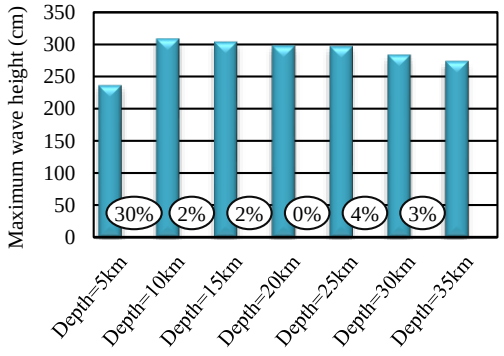

Figure 9. Variation of maximum tsunami wave height with earthquake depth. The numbers inside the circles indicate the amount of change in wave height between successive intervals of earthquake depth.

In order to be more sure about the accuracy of the results of the of earthquake depth sensitivity analysis, in addition to the nearshore wave station, the tsunami wave height has also been recorded at another point in the deep water area of Chabahar Port (at a depth of 1600 meters) (Figures 10 and 11). Again, it is observed that an earthquake depth of 10 kilometers creates the highest wave height. Furthermore, the changes in tsunami height due to a 5-kilometer change in earthquake depth are relatively small (less than 10 percent). the comparison of the recorded waves at the two numerical stations also shows that the nearshore waves (with a height of 2.5 to 3 meters) are higher than the deep water waves (with a height of 1 to 1.5 meters).This can be attributed to the increase in the height tsunami waves as they approaches the coast due to shoaling.

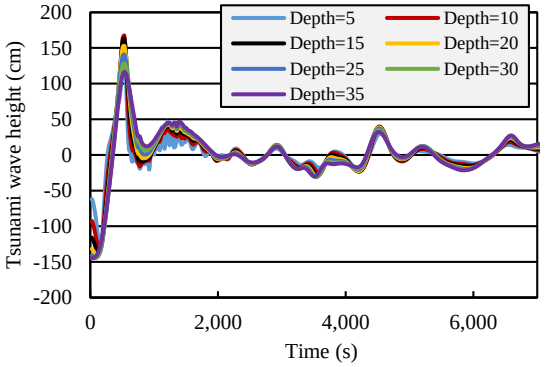

Figure 10. Time series of tsunami waves recorded during the sensitivity analysis of earthquake depth (at the deep water numerical wave station).

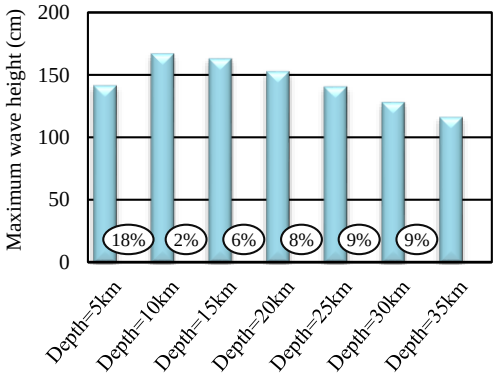

Figure 11. Variation of maximum tsunami wave height with earthquake depth. The numbers inside the circles indicate the amount of change in wave height between successive intervals of earthquake depth (at the deep water numerical wave station).

5. Conclusion

The review of studies on MSZ's tsunami hazard assessment showed that PTHA is currently recognized as an essential approach for conducting these studies. Therefore, due to taking into consideration all of the uncertainties associated with tsunamis in PTHA, the simulation of a large number of possible tsunami scenarios will be inevitable for future MSZ's tsunami studies, which requires high computational costs. The number of these scenarios are a function of the diversity of included uncertain seismic parameters and the

considered intervals for their values. In order to reduce and optimize the number of scenarios in future studies of tsunami assessment in the Makran region, the proposed values of some MSZ's uncertain seismic parameters, including earthquake magnitude and depth as well as dip and rake angles, in previous studies were investigated. After that, using numerical modeling and sensitivity analysis, the effects of variations in the mentioned parameters on the subsequent tsunamis were evaluated. Finally, based on the obtained results, the range and change interval of these seismic parameters are suggested as following:

Earthquake magnitude: Since change in earthquake magnitude in intervals of Mw 0.1 considerably affect the tsunami waves, with an average change of approximately 20% in wave height at each step (Figure 2 and 3), use of a value of Mw 0.1 as the minimum interval of earthquake magnitude variations seems necessary for comprehensive tsunami scenarios in the Makran region. However, considering that tsunamis caused by earthquakes smaller than Mw 8 are less hazardous and have wave heights less than 1 meter (Figure 3), in order to reduce the number of simulation scenarios, it is possible to set slightly larger steps for magnitude variations in this range (Mw <8).

Dip angle: according to the slight changes in tsunami height caused by 3-degree variations in dip angle (Figure 4), considering two or three values in the range of 2º to 20º degrees as possible values for the dip angle seems sufficient for developing MSZ's tsunami scenarios. However, if the minimum number of scenarios is desired, due to the direct relationship between dip angle and tsunami height (Figure 5), a constant value in the range of 10 to 15 degrees can be set for the this angle (with a little overestimation of tsunami waves).

Rake angle: Due to the very slight changes in waves of tsunami height corresponding to variations in rake angle (Figures 6 and 7), it is not necessary to change the rake angle values when possible tsunami scenarios of MSZ is defined. Considering a constant value of 90 degrees for the slope angle, as the value leading to maximum tsunami wave height (Figure 7), in different scenarios seems reasonable.

Earthquake depth: since the 5-kilometer variations in earthquake depth leads to small changes in tsunami height (Figures 8 to 11), larger intervals of depth variations can be applied in MSZ's tsunami scenarios (for example, depth values of 10, 20, and 30 kilometers). Furthermore, as earthquake depth of 10 and 15 kilometers creates the highest tsunami wave height, in order to reduce the number of scenarios, it is possible to consider one of these two values as the fixed earthquake depth value.

8. References

[1] National Centers for Environmental Information (NCEI) (2017), NGDC/WDS Global Historical Tsunami Database.

[2] Heck, N. H. (1947). List of seismic sea waves. Bulletin of the Seismological Society of America, 37(4), 269-286.

[3] Rashidi, A., Shomali, Z. H., Dutykh, D., & Keshavarz Farajkhah, N. (2020). Tsunami hazard assessment in the Makran subduction zone. Natural Hazards, 100(2), 861-875. https://doi.org/10.1007/s11069-019-03848-1

[4] Rajendran, C. P., Rajendran, K., Shah-Hosseini, M., Beni, A. N., Nautiyal, C. M., & Andrews, R. (2013). The hazard potential of the western segment of the Makran subduction zone, northern Arabian Sea. Natural hazards, 65, 219-239. https://doi.org/10.1007/s11069-012-0355-6

[5] Heidarzadeh, M., Pirooz, M. D., Zaker, N. H., & Yalciner, A. C. (2009). Preliminary estimation of the tsunami hazards associated with the Makran subduction zone at the northwestern Indian Ocean. Natural Hazards, 48, 229-243. https://doi.org/ 10.1007/s11069-008-9259-x

[6] Neetu, S., Suresh, I., Shankar, R., Nagarajan, B., Sharma, R., Shenoi, S. S. C., ... & Sundar, D. (2011). Trapped waves of the 27 November 1945 Makran tsunami: observations and numerical modeling. Natural Hazards, 59, 1609-1618. https://doi.org/10.1007/s11069-011-9854-0

[7] Rastgoftar, E., & Soltanpour, M. (2016). Study and numerical modeling of 1945 Makran tsunami due to a probable submarine landslide. Natural Hazards, 83, 929-945. https://doi.org/10.1007/s11069-016-2356-3

[8] Heidarzadeh, M., & Satake, K. (2017). A combined earthquake–landslide source model for the Tsunami from the 27 November 1945 M w 8.1 Makran earthquake. Bulletin of the Seismological Society of America, 107(2), 1033-1040. ttps://doi.org/10.1785/0120160196

[9] Momeni, P., Goda, K., Heidarzadeh, M., & Qin, J. (2020). Stochastic analysis of tsunami hazard of the 1945 Makran subduction zone Mw 8.1–8.3 earthquakes. Geosciences, 10(11), 452. https://doi.org/10.3390/geosciences10110452

[10] Honarmand, M., Shanehsazzadeh, A., & Zandi, S. M. (2020). 3D numerical simulation of tsunami generation and propagation, case study: Makran tsunami generation and penetrating in Chabahar Bay. Ocean Engineering, 218, 108109. https://doi.org/10.1016/j.oceaneng.2020.108109

[11] Heidarzadeh, M., Pirooz, M. D., & Zaker, N. H. (2009). Modeling the near-field effects of the worst-case tsunami in the Makran subduction zone. Ocean Engineering, 36(5), 368-376. https://doi.org/10.1016/j.oceaneng.2009.01.004

[12] Swapna, M., & Srivastava, K. (2014). Effect of Murray ridge on the tsunami propagation from

Makran subduction zone. Geophysical Journal International, 199(3), 1430-1441.

[13] Akbarpour Jannat, M. R., Rastgoftar, E., & Asano, T. (2017). Tsunami assessment for inundation risk management at chabahar bay facilities in Iran. International Journal of Coastal and Offshore Engineering, 1(2), 27-39. https://doi.org/10.22034/ijcoe.2023.340919.0

[14] Heidarzadeh, M., & Kijko, A. (2011). A probabilistic tsunami hazard assessment for the Makran subduction zone at the northwestern Indian Ocean. Natural hazards, 56, 577-593.

[15] Salah, P., Sasaki, J., & Soltanpour, M. (2021). Comprehensive probabilistic tsunami hazard assessment in the Makran subduction zone. Pure and Applied Geophysics, 1-23. https://doi.org/10.1007/s00024-021-02725-y

[16] Zoljoodi, M., & Zoljoodi, R. (2020). Executive management engineering plans for comparison with tsunami damage. International Journal of Coastal, Offshore and Environmental Engineering, 5(4), 19-23. https://doi.org/10.29252/ijcoe.3.4.19

[17] American Society of Civil Engineers. (2017, June). Minimum design loads and associated criteria for buildings and other structures. American Society of Civil Engineers.

[18] Okada, Y. (1985). Surface deformation due to shear and tensile faults in a half-space. Bulletin of the seismological society of America, 75(4), 1135-1154.

[19] Haberland, C., Mokhtari, M., Babaei, H. A., Ryberg, T., Masoodi, M., Partabian, A., & Lauterjung, J. (2021). Anatomy of a crustal-scale accretionary complex: Insights from deep seismic sounding of the onshore western Makran subduction zone, Iran. Geology, 49(1), 3-7. https://doi.org/10.1130/G47700.1

[20] Noson, L. L., Qamar, A., & Thorsen, G. W. (1988). Washington State Earthquake Hazards. Washington State Department of Natural Resources, Washington Division of Geology and Earth Resources Information Circular 85.

[21] Frohling, E., & Szeliga, W. (2016). GPS constraints on interplate locking within the Makran subduction zone. Geophysical Supplements to the Monthly Notices of the Royal Astronomical Society, 205(1), 67-76. https://doi.org/10.1093/gji/ggw001

[22] Smith, G. L., McNeill, L. C., Wang, K., He, J., & Henstock, T. J. (2013). Thermal structure and megathrust seismogenic potential of the Makran subduction zone. Geophysical Research Letters, 40(8), 1528-1533. https://doi.org/10.1002/grl.50374

[23] Wells, D. L., & Coppersmith, K. J. (1994). New empirical relationships among magnitude, rupture length, rupture width, rupture area, and surface displacement. Bulletin of the seismological Society of America, 84(4), 974-1002.

[24] Byrne, D. E., Sykes, L. R., & Davis, D. M. (1992). Great thrust earthquakes and aseismic slip along the plate boundary of the Makran subduction zone. Journal of Geophysical Research: Solid Earth, 97(B1), 449-478.

[25] Heidarzadeh, M., Pirooz, M. D., Zaker, N. H., & Synolakis, C. E. (2009). Evaluating tsunami hazard in the northwestern Indian Ocean. Tsunami Science Four Years after the 2004 Indian Ocean Tsunami: Part I: Modelling and Hazard Assessment, 2045-2058. https://doi.org/10.1007/s00024-008-0415-8

[26] Rajendran, C. P., Ramanamurthy, M. V., Reddy, N. T., & Rajendran, K. (2008). Hazard implications of the late arrival of the 1945 Makran tsunami. Current Science (00113891), 95(12).

[27] Heidarzadeh, M., Pirooz, M. D., Zaker, N. H., & Mokhtari, M. (2007). Modeling the 1945 Tsunami in the south coast of Iran. the 3rd National Congress of Civil Engineering (in Persian)

[28] Gica, E. (2008). Development of the forecast propagation database for NOAA's Short-term Inundation Forecast for Tsunamis (SIFT).

[29] Schlüter, H. U., Prexl, A., Gaedicke, C., Roeser, H., Reichert, C., Meyer, H., & Von Daniels, C. (2002). The Makran accretionary wedge: sediment thicknesses and ages and the origin of mud volcanoes. Marine Geology, 185(3-4), 219-232. https://doi.org/10.1016/S0025-3227(02)00192-5

[30] Polet, J., & Kanamori, H. (2000). Shallow subduction zone earthquakes and their tsunamigenic potential. Geophysical Journal International, 142(3), 684-702. https://doi.org/10.1046/j.1365-246x.2000.00205.x

[31] Synolakis, C. E., Chen, W. F., & Scawthorn, C. (2003). Tsunami and Seiche in Earthquake Engineering Handbook.

[32] Titov, V. V., & Synolakis, C. E. (1998). Numerical modeling of tidal wave runup. Journal of Waterway, Port, Coastal, and Ocean Engineering, 124(4), 157-171. https://doi.org/10.1061/(ASCE)0733-950X(1998)124:4(157)

INTERNATIONAL JOURNAL OF
COASTAL, OFFSHORE & ENVIRONMENTAL ENGINEERING IJCOE Vol.8/No. 4/Autumn 2023 (18-30)

Available online at: www. Ijcoe.org

Uncertainties and Barriers to CCS Acceptance & Implementation

Maryam Shourideh[1], Sirous Yasseri [2]

[1] Maryam Shourideh, Mechanical Engineering, Brunel University London, United Kingdom; maryam.shourideh@brunel.ac.uk
[2] Sirous Yasseri, Mechanical Engineering, Brunel University London, United Kingdom; sirous.yasseri@brunel.ac.uk

ARTICLE INFO

Article History:
Received: 20 Oct. 2023
Accepted: 25 Nov. 2023

Keywords:
Climate change
CCS
Adaptation barriers
System thinking

ABSTRACT

Implementing carbon capture and storage (CCS) technologies is essential to mitigate the damaging effects of climate change due to the earth's temperature increase. However, despite the potential benefits of CCS, its acceptance has been slow. This paper identifies and examines the barriers to CCS acceptance, which include technical, economic, regulatory, and social factors. Economic barriers include the lack of financial incentives while regulatory barriers include the absence of a comprehensive legal framework. Lastly, social barriers include the lack of public awareness and understanding of CCS and the negative perception of technology. Technical barriers include a deficiency of desired infrastructure in all stages of CCS including capture, transportation, and storage.

1. Introduction

Global warming means the average temperature increase on the surface of the earth, which is mainly attributed to human actions e.g. the combustion of fossil fuels [1]. The Paris Agreement (PA) is an internationally voluntary compliance treaty to limit the increase in the global average temperature to less than 2°C above pre-industrial levels, with a further goal of pursuing efforts to maintain the temperature rise below 1.5°C. Recently, the emphasis has been on keeping global warming below 1.5°C by the end of this century, as highlighted by world leaders [2]. Carbon, capture, and storage (CCS) technology has the potential to prolong the operational lifespan of power plants, cement producing plants, and oil refineries that would have been decommissioned because of their high emission levels. It has the potential to lower carbon dioxide emissions by around 80-90% for a typical contemporary conventional power plant [3].

Globally, the current capacity of CCS facilities to capture CO2 is approximately 45 million metric tons. However, to effectively combat climate change, this capacity must be increased to capture over 220 million metric tons of CO2 annually. The total CO2 emissions worldwide are over 34 billion metric tons, highlighting the urgent need for significant improvements in CCS technology and infrastructure [4]. The successful implementation of CCS technologies depends on several important factors, including economic feasibility and public acceptance, as well as technological progress and environmental impact [5]. It can be concluded that CCS is a system of a complex nature that includes not only the technical aspects of capture, transport, and storage but also it is an organizational system that involves a group of people together with workers, managers, and all other stakeholders [6]. The complex system can be divided into four subsystems including:

1. Human and organizational subsystem
2. Capture
3. Transportation
4. Storage

Each of the subsystems has its barriers and obstacles preventing technology acceptance and extensive utilization. In general, the paper is divided into two types of barriers, human and organizational challenges, and technical challenges.

2. Human and Structural Barriers

Studying the social barriers of CCS is as important as studying the technical barriers of CCS technology. **Error! Reference source not found.** shows the triangle of social acceptance. Socio-political acceptance pertains to the broad acceptance of policies and technologies by key social actors such as policymakers and the general public. On the other hand, market acceptance is more specific and considers the diffusion of innovations among consumers and the

decisions by investors who operate in national and/or multinational markets. Lastly, "public acceptance is the acceptance of particular projects at the local level by all stakeholders, which includes residents and local authorities in the area of growth" [7].

Based on a survey, the main challenges attributed to social acceptance revolve around human and organizational behaviors. These obstacles can be summarized as follows [8]:

(1) the cost and recovery of expenses,
(2) the absence of a financial incentive,
(3) the presence of risks of long-term liability, and
(4) the lack of an all-encompassing regulatory framework

The current high cost and uncertainties are two significant obstacles to the implementation of CCS [9]. The key challenge to the extensive utilization of CCS technology is "the expense related to its deployment" [10]. Lowering the cost of CO2 capture is crucial in reducing the overall cost of CCS, as it accounts for around 70% of the total cost. The operating expenses of CCS are considerably higher than its capital costs due to the commercial prices of fuel and electricity. If the energy generated by the facility could be utilized, the operating expenses would significantly decrease [11].

CCS liability is typically categorized as either operational or post-injection. Operational liability pertains to health, safety, and environmental risks associated with the capture, transportation, and injection of CO2. Conversely, post-injection liability covers health, safety, environmental, and climate risks caused by CO2 that travel from the intended storage site to another subsurface unit or back to the atmosphere [12].

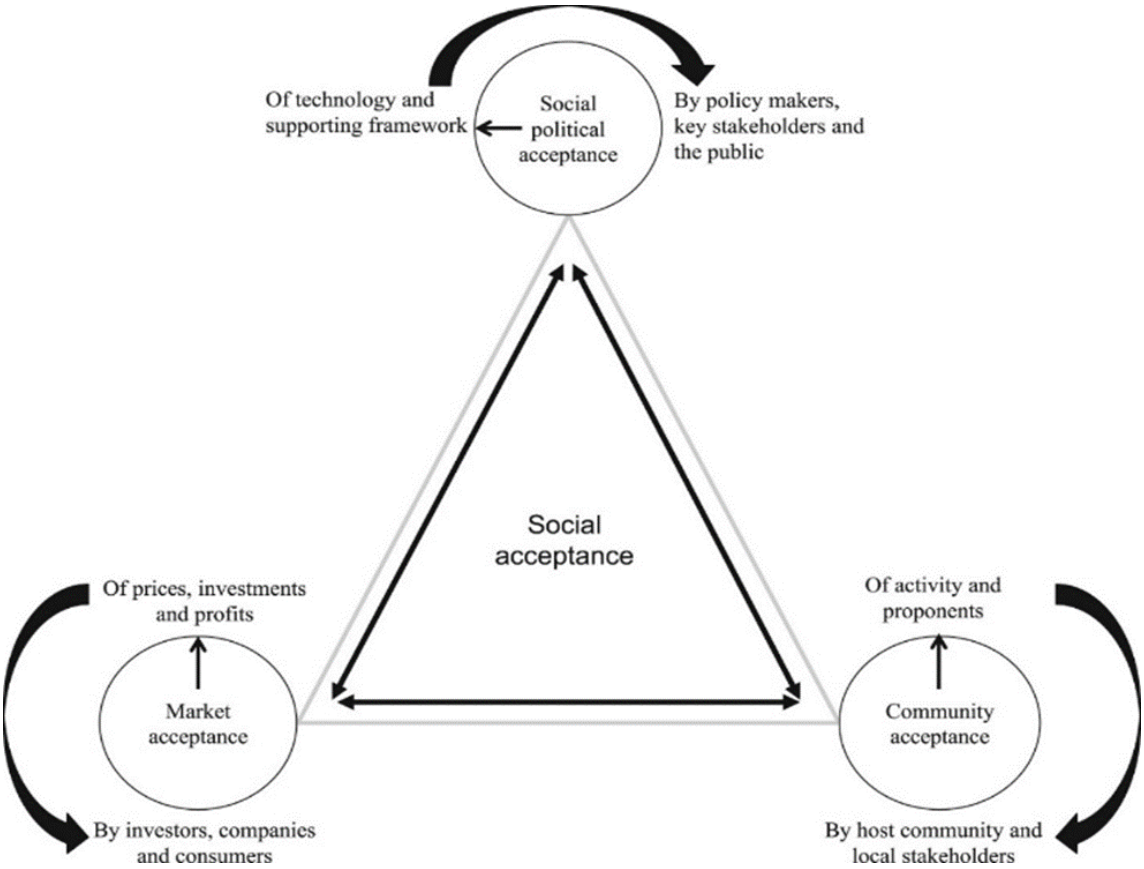

Figure 1. The triangle of social acceptance [7]

"The liability throughout the lifecycle of CCS can pose a significant challenge which eventually can be a barrier to the CCS investment and utilization of the technology" [13]. The storage of significant amounts of CO2 will result in considerable financial obligations. Therefore, entities operating within this sector must have the ability and willingness to take on such responsibilities [14]. Projects usually demand substantial capital investment and infrastructure, leading to a prolonged investment period. As a result, investors who intend to support CCS projects must be prepared to make a long-term investment commitment [15]. Lack of financial inspiration and lack of financial support from the government reduce the investment in technology [16]. Relying solely on public funding as the primary source of investment for CCS is not sufficient to sustain the required level of investment in CCS. CCS facilities require significant capital investments, which leads to high material costs for projects, ultimately reducing their economic viability

[17]. Barriers to investment in CCS are listed as follows [18]:

- Lack of financial motivation for investing in carbon dioxide capture and storage.
- Cross-chain risk is a possible difficulty. This risk can be addressed by the government where the establishment of shared transport and storage infrastructure by either investing in the infrastructure directly or creating a regulatory framework that enables cost-effective network development.
- The absence of a clearly defined legal and regulatory framework that plans the liabilities of carbon dioxide storage operators may pose a long-term liability risk that discourages private sector investment.
- Lack of adequate financial support through grants, concessional loans, accelerated depreciation, or other means to attract private investment in carbon capture and storage projects.
- Failure to identify and evaluate further policy measures that can mitigate specific financial risks.
- Lack of research data and information to measure the influence of various risk categories on the cost of debt discourages private sector investments.

The regulations for enforcement aim to ensure the safety and security of the process, proper storage, and monitoring and verification before and after injection [19] [20]. In Canada, the regulations were designed to promote the development of CCS by eliminating barriers to long-term CO2 storage and security [21]. Insufficient environmental regulations on CO2 emissions have been a significant obstacle to the implementation of carbon capture in power plants [22]. The policy complications such as lack of appropriate supervision and lack of regulations such as dividing the liability between public and non-governmental organizations and insufficient environmental regulations on CO2 all create an unsafe environment for the CCS technology practice and can be barriers to its implementation [16] [22]. Other barriers such as inadequate government support can be an obstacle to the wide use of CCS. Despite some countries, such as China, the USA, and Australia, being able to overcome the obstacles associated with CCS projects, their implementation is currently experiencing a slowdown due to inadequate government support [23]. “Trust in decision-makers and perceptions of procedural and distributive justice are crucial factors that can influence the success of deploying specific projects” [24]. Public trust is higher in non-governmental organizations compared to governmental industrial organizations [25]. The absence of incentives, political will, and public support are among the factors that may lead to public opposition, consequently contributing to discouraging CCS technology usage [26]. Companies in the CCS industry are expected to exhibit a commitment to mitigating potential incidents and hazards through the conduction of environmental and health-related risk assessments. This expectation is placed not only by the public, customers, and governments but also by in-plant personnel [27]. Noting that numerous projects are being pursued jointly by the industry and government, it becomes challenging to determine who should be responsible for leading the communication plan. Some people believe that it is the government’s responsibility to reach out to the public and lead education initiatives. It is acknowledged that a collaborative strategy would yield the best results by creating unified messages from different stakeholder groups, thereby reducing the likelihood of any misunderstandings [28]. Limited and insufficient knowledge of technology as a whole also creates a problem and thus decreases the funding of the technology [16].

Table 1. Number of workers in a carbon capture plant [29]

			Project Jobs	**Operation Jobs**
Carbon capture retrofit	Industry	Steel mill	1,680 – 3,030	170 - 310
		Refinery	440 - 760	40 - 70
		Cement plant	430 – 690	60 – 110
		Hydrogen plant	175 – 300	20 - 30
		Ethanol plant	30 - 50	5- 10
	Power	Coal power plant	1,800 – 3,350	160 – 300
		Natural gas combined-cycle power plant	1,140 – 2, 090	100 – 180
CO2 transport infrastructure		Trunk line (20” diameter pipeline, 200 miles long)	1,250 – 2,190	8 – 20
		Feeder line (12” diameter pipeline, 50 miles long)	250 - 370	2 - 5

According to Table 1, in the short term, there could be a larger pool of available workers because the project jobs need a larger number of skilled workers and as soon as the facilities start to operate, the number of workers decreases during the operating phase [29]. In the long run, a potential obstacle could arise due to the lack of skilled labor [10].

Integrating CCS systems presents challenges both technically and organizationally, and there is currently no clear plan on how this integration will be accomplished. Moreover, it is unclear how mature and

scalable the current CCS technologies are, and the pace at which they can be further developed is uncertain [30].

3. Technical Barriers

"Carbon capture plants are large process plants with impacts relating to appearance, emissions, noise, traffic, safety and environmental hazards and other potential impacts" [14]. All these terms can be a barrier to the development of CCS plants. From a technical perspective, the behavior or quality of one component in a system can affect other components. For instance, the quality of the capture stage can determine the level of impurities in the system. This, in turn, can lead to consequences like "corrosion during transport and injection, as well as the geochemistry of the storage in the long run" [31]. The introduction of CCS in different industries may have an impact on the competitive environment. This is because the cost of implementing CCS is higher, which could affect the competition between sectors that adopt CCS and those in regions that do not face similar restrictions [32]. When it comes to CO2 utilization, there are two primary aims in increasing urea yield. Firstly, the fluctuating prices and demand for urea and NH3 make it difficult to conduct long-term assessments. Secondly, there is the potential issue of high capital costs associated with implementing CO2 capture infrastructure [33]. Utilizing CO2 in the process of concrete curing has a main barrier which is the financial constraints when it comes to adopting new technologies due to operating in a fiercely competitive market where capital is limited [33].

Oil and gas reservoirs that have been depleted are located all over the world. Nevertheless, it is uncertain that people will readily accept the notion of storing CO2 in reservoirs that are situated near residential areas or beneath them. As a result, CO2 must be transported to distant fields, away from the source, which adds to the cost of CCS projects [34]. Infrastructure limitations, including the absence of storage facilities nearby and inadequate connectivity to transportation and storage infrastructure, can pose significant obstacles to the implementation of CCS [32]. The ownership and operation of the various components in a carbon capture chain by different companies can be an obstacle to the project if any of these elements become unavailable during its lifespan [35]. Reliance on the availability of some equipment in the CCS chain could result in extra costs and potentially discourage investment in the project.

Currently, the global storage capacity for CO2 is substantial however determining the portion of the capacity that can be utilized needs considering a range of factors such as geography, injection, as well as the necessary institutional and business capacities [37]. Broadly speaking, areas where storage supply estimates are well-established, indicate that Carbon Capture and Storage (CCS) is not likely to face limitations due to the availability of local storage resources. On the other hand, in areas beyond the developed regions, the availability of storage resources is uncertain. However, considering the global distribution of sedimentary basins, very few sites may experience local storage resource limitations [10].

For retrofit projects, in case the power plant site lacks sufficient space to accommodate the CO2 capture facility, the plant may not be feasible for CCS retrofit from a technical standpoint [37]. Due to the extra energy required for the capture process, there will be an increase in emissions during transportation in the CCS life cycle as a result of the fuel penalty [38]. For example, a significant rise in direct emissions of Ammonia (NH3) is predicted compared to the non-CCS scenario. Ammonia is a poisonous and toxic gas [38].

"This can be a possible barrier since according to energy system transition models that aim to restrict global warming to below 2°C, the consumption of fossil fuel reserves by 2050 is estimated to be 26% if CCS technology is not employed. However, if CCS is employed, the estimated consumption of fossil fuel reserves by 2050 is 37%" [10].

One obstacle to the implementation of CCS is the weak manufacturing ability of certain countries, which obstructs their ability to develop profitable carbon capture technologies. Governments must consider their interest in promoting the growth of domestic CCS technologies against the option of importing potentially better technologies from foreign countries [39]. Moreover, the affordability of decarbonization alternatives can be a barrier to the implementation of carbon capture in certain situations [14].

4. Uncertainties of CCS

There are uncertainties in the deployment of CCS, which include technical, economic, political, and financial issues, as well as acceptance by the communities, without the government's support to make CCS a part of the climate mitigation mix. There is a need to provide evidence and analysis to inform and assure the government and investors, regarding financing climate change mitigation measures. The first step is to identify the known uncertainties and seek solutions to reduce, mitigate, and manage their impact. The effects of some of these uncertainties, together with suggested methods for assessing and their mitigation are summarized in **Error! Reference source not found.**.

Table 2. Uncertainties and recommended actions

	Key uncertainties	References
1	**Diversity of methods** The wide range of methods available in technology poses a challenge for investors and policymakers, as it introduces uncertainty. While choosing a method early on can expedite development, it also carries the risk of committing to less effective technologies.	[40]
2	**Secure storage** The long-term CO2 geological storage safety is uncertain, and there is a lack of confidence in methods for accurately assessing and managing the associated risks.	[41]
3	**Scaling up and timeline for implementation** There is a lack of clarity regarding the feasibility and pace at which CCS technologies can be effectively scaled up, and improved to reach maturity level.	[42]
4	**Integration of CCS systems** It is uncertain how CCS systems would be integrated to act as one system. Integration of elements of CCS is a technical challenge, as well as organization and governance issues.	[43]
5	**Feasibility in terms of economic and financial aspects** The implementation of CCS carries significant uncertainty regarding its future financial implications and risks, with policy factors strongly influencing the level of economic uncertainty.	[9]
6	**Policy, politics, and regulation** The implementation of CCS is significantly impacted by political and regulatory uncertainties, as well as the selection and structure of policies	[44]
7	**Public acceptance** Community acceptance is crucial to CCS development but acceptance is uncertain. Social interactions shape attitudes towards CCS acceptance	[25]
8	**Public knowledge** CCS deployment is directly affected by public knowledge of the technology. The level of uncertainty in technology increases as People's understanding of it decreases.	[44] [45]
9	**Technology Uncertainties** CCS technologies, which can be complex and costly, often involve technologies that have not yet been proven at a commercial scale. The uncertainties decrease with the wider use of technology.	[14]
10	**Other decarbonisation Options** Some possible alternatives for decarbonization include reducing demand, substituting products, electrifying processes, improving efficiency, and switching fuels. It is uncertain how much other decarbonisation methods will develop and how it will affect CCS.	[14]

5. Technology Readiness Level

"Technology Readiness Levels (TRL) are a measurement system utilized to evaluate the level of maturity of a specific technology" [46]. TRLs are commonly used as a standard measure to indicate the readiness level of new technologies or the modification of existing ones for integration into a product [47]. A TRL rating is assigned to each technology project after it is evaluated against the parameters for each technology level, taking into consideration the project's progress. TRL range from 1 to 9, with TRL 1 being the lowest and TRL 9 being the most mature technology as shown in **Error! Reference source not found.** [48] [49].

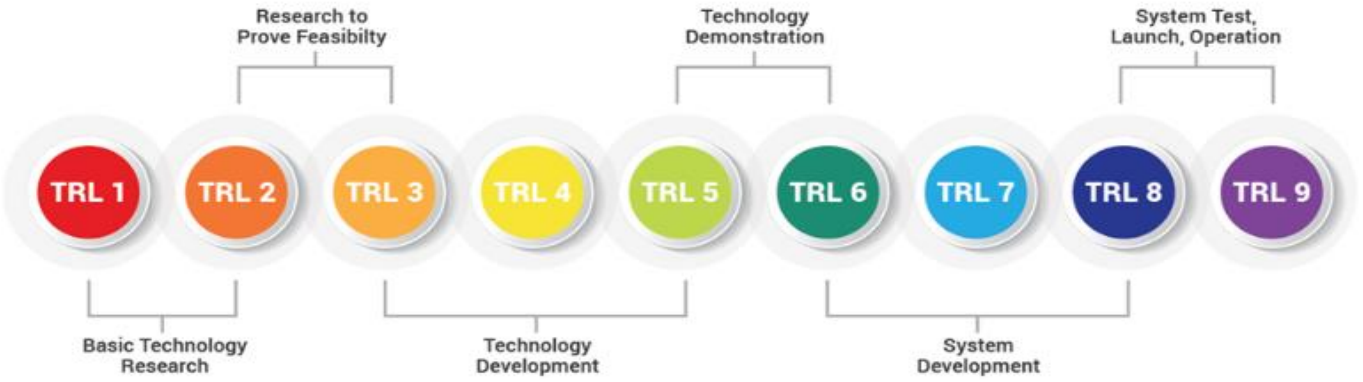

Figure 2. Technology Readiness Level (TRL) [49]

"To ensure that technology developed in science and technology programs, or adopted from industry or any other sources, is considered mature enough for the previous product, then it must be assumed in a new environment at TRL 6 and preferably in an operational environment at TRL 7" [19][47][50][51][52].
Similarly, the technology readiness assessment can be done for CCS technology. **Error! Reference source not found.** shows that congestion is commonly encountered in the development stages of technologies at TRL 3, TRL 6, and TRL 7. "Progressing a technology beyond TRL 3 usually requires additional funding, while improving it beyond TRL 5 and TRL 7 necessitates significant investment and/or commercial interests" [53]. When it comes to CO2 capture technologies, amine solvents and physical solvents have a TRL of 9 and are widely used where encapsulated solvents and ionic liquids have the lowest TRL of 2 to 3 among the liquid solvents [54][55]. TRL 9 means that the technology is mature enough and is in commercial operation.

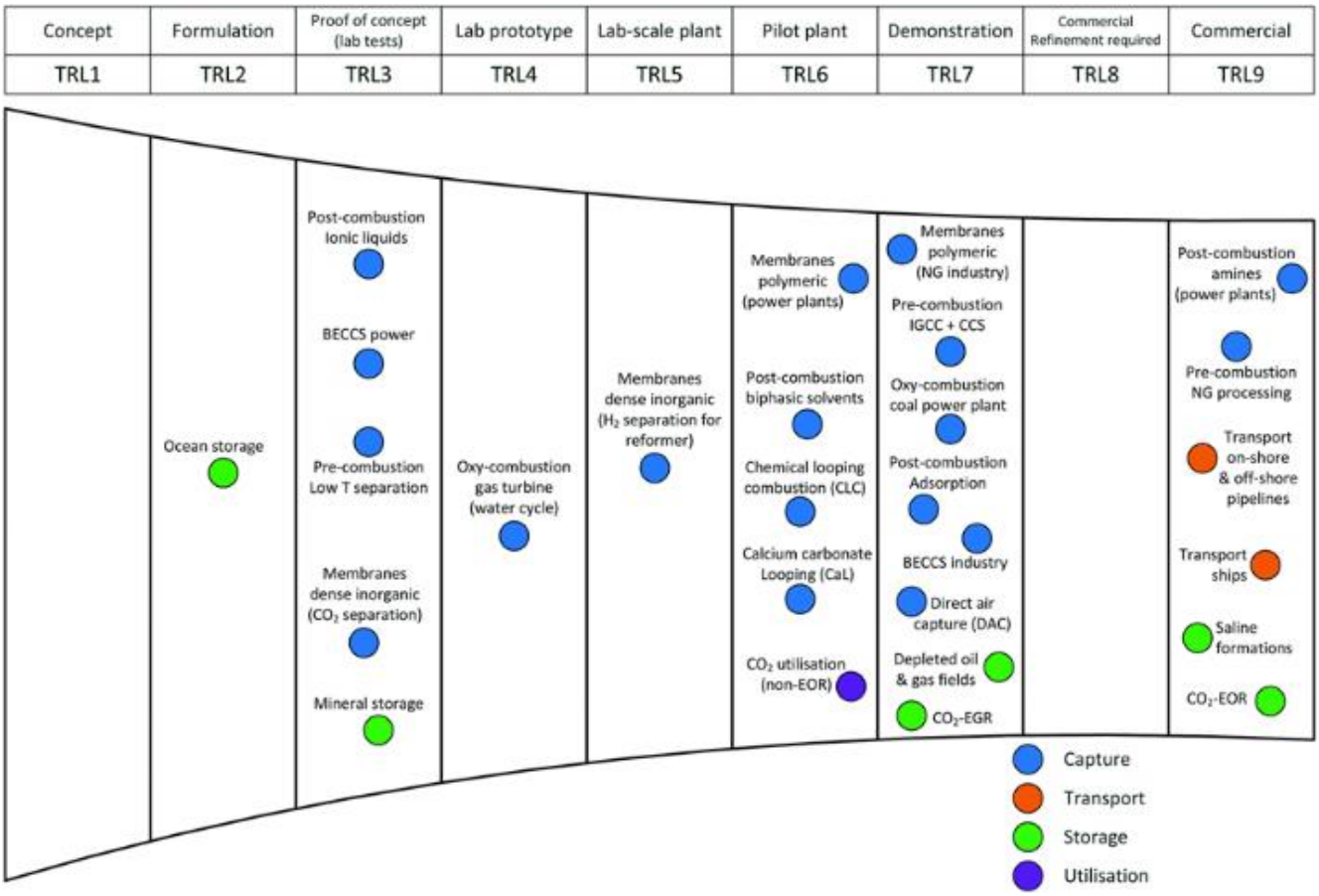

Figure 3. CCS in terms of TRL [53]

An issue with the TRL framework is that it cannot convey the level of effort or difficulty needed to reach the next TRL rank in a development cycle. This deficiency suggests the need for modifying the TRL framework to include the assessment of difficulty to better understand timing and resource allocation [56].

6. Overcoming Barriers

Several countries have had programmes to build large-scale CCS installations during the last two decades. By the second quarter of 2023, 37 operational facilities (equivalent to around 50.6 MtCO2/y) will be operating worldwide [57]. The expenses associated with setting up a pilot plant are typically significantly greater than those of a full-scale installation. This is primarily attributed to several factors, including economies of scale, standardized manufacturing processes, minimized contingencies, more affordable financing options, and the utilization of shared CO2 transport and storage infrastructure. [58][59].

CCS is fundamentally dependent on government intervention in some form of incentive to store CO2 [26]. "In the absence of adequate climate-based incentives, the majority of contemplated projects have used captured CO2 for enhanced oil recovery (EOR), and many are based on the relatively straightforward removal of CO2 from natural gas" [60]. A market-oriented approach, such as implementing an emission cap and credit trading system, can be beneficial. It allows companies that can perform abatement at the lowest cost to take on most of the responsibility while other firms purchase emission credits. This strategy encourages continuous improvement in technology efficiency, unlike command-and-control policies that incentivize minimizing compliance costs with performance or technology standards [22].

The cost of the CCS pilot plant exceeds the available incentives, and this financial gap is worsened by various risks specific to the technology. These risks make the private sector reluctant to invest due to the uncertainty surrounding the investment [18]. These are primarily related to the need for a substantial new infrastructure for CO2 transport and storage. The process of identifying appropriate geological formations for CO2 storage is both time-consuming and expensive. Additionally, the potential cost of CO2 leakage is uncertain and can be considered an uncertain risk under certain regulatory bases [61]. Developers would not be inclined to provide infrastructure for the transport and storage of CO2 without assurances of a reliable and guaranteed source of CO2, even though it would be more efficient to have infrastructure that can accommodate multiple CO2 streams [62]. Therefore, to cover the costs and risks associated with the deployment of CCS infrastructure, it may be necessary for the government to play a larger role by providing financial support, such as regulating a fixed revenue for CO2 storage and funding the assessment of storage sites. Social acceptance is directly influenced by people's trust in CCS shareholders. "People will accept technology more if they have the opportunity to give their opinion. The lack of significant attention given by CCS experts to early and meaningful engagement implies that there is an opportunity to enhance the transfer of knowledge from the research literature on public engagement to those responsible for implementing it" [63].

The close connection between the success of CCS and international commitments to decarbonization highlights the importance of coordinated efforts. "The challenges encountered by the growing CCS industry also indicate potential additional advantages that can be derived from global collaboration" [64].

The Carbon Sequestration Leadership Forum (CSLF), International Energy Agency (IEA), and Global Carbon Capture and Storage Institute (GCCSI) are well-known international organizations that have been actively advocating for increased political commitment towards the deployment of CCS technology. "Their efforts have been primarily directed towards advocating for the advancement of substantial demonstration CCS initiatives, fostering the development of CCS capabilities in non-OECD (Organisation for Economic Cooperation and Development) nations, and enhancing public and political understanding of the technology" [64]. "International organizations have long helped create awareness and tackle the challenges of climate change. They serve three necessary tasks in driving climate mitigation efforts, including" [65]:

1. Spreading research-based knowledge and offering recommendations.
2. Monitoring the progress of nations in achieving climate targets and analyzing data provided by national governments.
3. Enabling collaboration between governmental and non-governmental entities. Merging international funds towards one large project may be an important route toward CCS pilot plants.

The law requires the Department of Energy (DOE) to allocate funds for carbon capture demonstration projects at different levels of technological advancement and to continue funding projects related to carbon storage. "To speed up the implementation of commercial-scale CCS, various regional initiatives have been introduced. These initiatives require knowledge sharing as a prerequisite for receiving public funding support. The idea behind this is to accelerate innovation through experiential learning and make the deployment of CCS more efficient and effective" [66].

An implicit value on emissions has been placed by regulation, which has also contributed to facilitating the implementation of CCS. The possibility of a forthcoming carbon tax has also been a factor in the

decision to implement CCS. “This underscores the significance of future policies, in addition to current ones, in influencing an investor's support for a CCS initiative” [67]. CCS deployment currently returning to the political agenda in many countries, leading to an increase in research funding. However, international activity to date has arguably focused largely on the role of research in finding ways to improve the economics of CCS, but there is a much more fundamental need for political action to encourage private investment in large demonstration projects.

7. System Thinking

In this section, we lay the foundation of an SD model to gain insight into CCS technology diffusion.

Technology diffusion encompasses a range of processes, starting from research and development (R&D) to the successful commercialization of products, which involves promotional and marketing efforts. The diffusion of technology holds significant potential to influence and transform society [68]. The socio-technical systems (STS) approach investigates the connections between social/community aspects and technical processes. STS approach encompasses several levels of interaction, between mechanical (hardware), informational (software), psychological (people), and social (public). By adopting such a comprehensive approach, the goal is to comprehend the interdependent relationships among a range of social and plants. “These elements engage with social motivations and work together to achieve a set of social goals that would otherwise be impossible” [69].

System thinking is an inclusive approach characterized by considering various perspectives and involving multiple stakeholders to adopt teamwork and collaboration in addressing intricate issues. According to Senge “Systems Thinking is a discipline for seeing the entire system with all its connectivity and their strength and feedback” [70].

That is there is a direct relationship between systems thinking and the notion of a system. A system consists of a set of interrelated components (variables). These components together with their inter-relationship define the system behaviour. The principles of systems thinking are listed below [71]:

1) every system is made of subsystems and sub-subsystems

2) The behaviour of a system is governed by the strength of the relationship between its components and feedback

3) There are balancing and reinforcing loops. Balancing loops pushes the system toward stability while reinforcing loops push the system toward extremes, zero or infinity. The role of feedback is to assure the stability and balance of a system,

4) Due to interactions between components they may be emerging behaviour

System-level modelling requires the combination of individual process models to create a comprehensive simulation of the entire CCS system. This approach takes into account the interactions between various components and their influence on the overall performance of the system. Many forms of system dynamic approach exist, that can be characterized using the following concepts [72]:

1. State and force: This concept involves understanding the current state of the system and the forces that influence its behaviour.
2. Feedback loops: Feedback is present when the interaction between elements A and B impacts the manner or strength of B's effect on A.
3. Nonlinearity: Non-linearity is a common characteristic of causal relationships that are not proportional.
4. Deadlines: A situation that initially follows a certain pattern can transform when a factor with a specific deadline is considered by the variable that is affected by it.
5. Structural change: In theory, a structure can experience changes in causalities that can occur at any time. These fluctuations serve as a reflection of the system's history.
6. A system boundary. In regression models, two types of variables can be observed [73]:
   - “Endogenous variables: These are variables that are influenced or determined by other variables present in the model.
   - Exogenous variables: These are variables that are not influenced or explained by other variables within the model. They are external variables.”

The system boundary can help to identify internal or external variables.

Systemic modelling is frequently used in the field of industrial safety to detect potential hazards caused by delays or subtle changes that may be challenging to identify through manual or automated means. Modelling plays a crucial role in connecting technical elements with social or human aspects of organizations [72]. Modelling the human behaviour and non-technical part of CCS is important.

- ❖ It plays a crucial role in offering valuable insights and data that can aid in policy development and decision-making regarding CO2 capture and storage. It enables the assessment of the potential effects of various policy measures, such as carbon pricing or subsidies, on the implementation and efficacy of CCS technologies.

Modelling CCS systems helps in evaluating the environmental impact of the entire process. It enables the evaluation of other environmental aspects, including air pollutants, water usage, and waste generation. This data is crucial for assessing the sustainability and environmental advantages of CCS

projects. The technical part of the technology diffusion includes:

- ❖ Modelling the capture process is important for the assessment of different capture technologies. It is important to find the most cost-effective means of CO2 capture. It assists in determining the effectiveness of CO2 capture, the energy demands involved, and the potential environmental consequences.
- ❖ Modelling the transport of CO2 is crucial for determining the most economical methods of transportation. This can be achieved through simulations of pipeline networks, taking into account factors such as pressure drop, flow rate, and distance to ensure efficiency and cost-effectiveness [74].
- ❖ Understanding the behaviour of CO2 in storage sites is essential to guarantee the stability and safety of the stored CO2 in the long term. This involves analyzing factors like reservoir characteristics, mechanisms that trap the CO2, and pathways that could potentially lead to leakage [74].

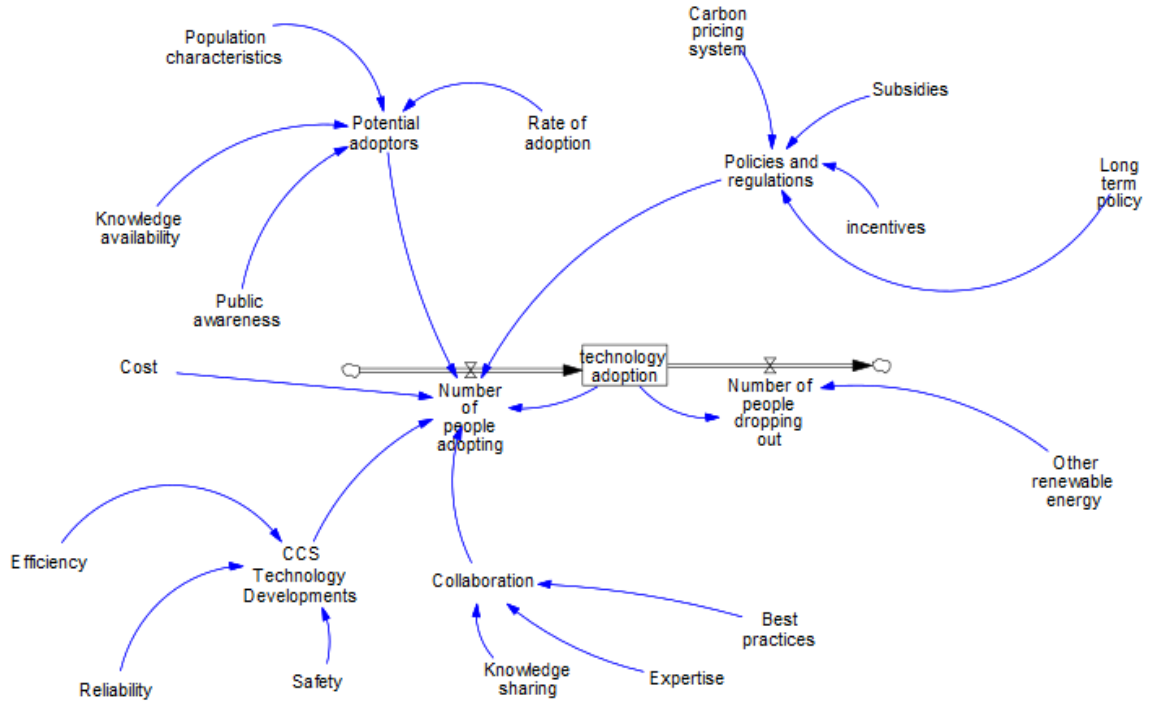

Figure 4. SD model for the analysis of Carbon Capture technology diffusion

To build a system dynamics model for the analysis of carbon capture technology diffusion, you would need to consider several key components.

Several crucial variables are important for the diffusion of carbon capture and storage (CCS) technology:

1. Policies and Regulations: Supportive government policies and regulations are vital in facilitating the widespread adoption of CCS technology. This includes incentives, subsidies, and a carbon pricing system [22][26].
2. Cost and Economics: The cost of implementing CCS technology is a significant factor in its diffusion. "Technological advancements and economies of scale have the potential to reduce the cost of CCS, thereby increasing its request to industries and investors" [16].
3. Technological Developments: It is crucial to continually invest in research and development to enhance CCS technology and facilitate its widespread adoption. Advancements in capture, storage, and monitoring techniques can enhance efficiency, reliability, and safety, making CCS more possible and attractive [42][75].
4. Public Acceptance: Public approval of CCS technology plays a vital role in its diffusion. Raising awareness about the advantages and safety of CCS is important to gather public support and effectively address any concerns or misunderstandings [25].
5. Infrastructure Development: The availability of a well-developed infrastructure for CO2 transportation and storage is critical for the diffusion of CCS technology. With increased

usage and advancements in technology and further improvements and innovations, the cost of the technology is likely to drop, and therefore it can be more widely adopted. "Constructing pipelines, storage sites, and related infrastructure can facilitate the successful deployment of CCS projects" [76].

6. Collaboration: Collaboration between countries, various CCS projects, and research institutions is fundamental for the diffusion of CCS technology. Sharing knowledge, expertise, and best practices can facilitate the global implementation of CCS at an accelerated pace [77].
7. Long-term stable policy: Attracting investments heavily relies on the presence of stable and enduring policies and regulations. CCS liability is typically categorized as either operational or post-injection. A long-term, stable policy that covers post-injection liability is necessary to provide comprehensive. Figure 4 shows a system dynamic model for the analysis of carbon capture technology diffusion.

8. Conclusions

Judging from the literature surveyed, one can conclude that there are several barriers to the acceptance and implementation of CCS technology. Some of the obstacles that implead the acceptance and implementation of CCS technology are the following: the high costs and financing uncertainties, insufficient public awareness and trust, legal and regulatory barriers, as well as technical and operational challenges. Additionally, the lack of a clear policy framework and political support might stop the deployment of CCS projects in many countries. Overcoming the aforementioned barriers requires addressing the economic, social, and environmental aspects of CCS and engaging stakeholders in a transparent and participatory process. Furthermore, policymakers need to provide a supportive regulatory and financial environment to encourage the deployment of CCS technology. Finally, public awareness is required to raise awareness about the benefits and risks of CCS and to build trust in technology.

List of Symbols

CCS	Carbon Capture and Storage
CO2	Carbon Dioxide
COP	United Nations Climate Change Conferences
CSLF	Carbon Sequestration Leadership Forum
DoE	Department of Energy
EOR	Enhanced Oil Recovery
GCCSI	Global Carbon Capture and Storage Institute
IEA	International Energy Agency
IEAGHG	IEA Greenhouse Gas R&D Programme
NH3	Ammonia
OECD	Organisation for Economic Cooperation and Development
PA	Paris Agreement
R&D	Research and Development
STS	Socio-Technical System
TRL	Technology Readiness Level

9. References

[1] Abbass, K., Qasim, M. Z., Song, H., Murshed, M., Mahmood, H., & Younis, I. (2022). *A review of the global climate change impacts, adaptation, and sustainable mitigation measures.* Environmental Science and Pollution Research, 29, 42539–42559. https://doi.org/https://doi.org/10.1007/s11356-022-19718-6

[2] Skjærseth, J. B., Andresen, S., Bang, G., & Heggelund, G. M. (2021). The Paris Agreement and key actors' domestic climate policy mix: Comparative patterns. *International Environmental Agreements: Politics, Law and Economics*, *21*(1), 59–73. https://doi.org/10.1007/s10784-021-09531-w

[3] Butt, T. E., Giddings, R. D., & Jones, K. G. (2012). Environmental sustainability and climate change mitigation-CCS technology, better having it than not having it at all! *Environmental Progress & Sustainable Energy*, *31*(4), 642–649. https://doi.org/10.1002/ep.10590

[4] Ritchie, H., Roser, M., & Rosado, P. (2017). CO_2 and Greenhouse Gas Emissions. *Our World in Data*. https://doi.org/https://ourworldindata.org/co2-and-greenhouse-gas-emissions

[5] Karayannis, V., Charalampides, G., & Lakioti, E. (2014). Socio-economic aspects of CCS Technologies. *Procedia Economics and Finance*, *14*, 295–302. https://doi.org/10.1016/s2212-5671(14)00716-3

[6] Samadi, J., & Garbolino, E. (2012). *Development of a Systemic Risk Management Approach for CO2 Capture, Transport and Storage Projects* (thesis). Sciences et génie des activités à risques, Paris.

[7] Van Os, H. W. A., Herber, R., & Scholtens, B. (2013). Not under our backyards? A case study of social acceptance of the Northern Netherlands CCS initiative. Renewable and Sustainable Energy Reviews, 30, 923–942. https://doi.org/10.1016/j.rser.2013.11.037

[8] Davies, L. L., Uchitel, K., & Ruple, J. (2013). Understanding barriers to commercial-scale carbon capture and sequestration in the United States: An

empirical assessment. *Energy Policy*, *59*, 745–761. https://doi.org/10.1016/j.enpol.2013.04.033

[9] Roussanaly, S., Ouassou, J. A., Anantharaman, R., & Haaf, M. (2020). Impact of uncertainties on the design and cost of CCS from a waste-to-energy plant. *Frontiers in Energy Research*, *8*. https://doi.org/10.3389/fenrg.2020.00017

[10] Budinis, S., Krevor, S., Dowell, N. M., Brandon, N., & Hawkes, A. (2018). An assessment of CCS costs, barriers and potential. *Energy Strategy Reviews*, *22*, 61–81. https://doi.org/10.1016/j.esr.2018.08.003

[11] Kimura , S. A. S., Shinchi, K., Coulmas, U., & Saimura, A. (Eds.). (2022). (rep.). *Study on the Potential for Promoting Carbon Dioxide Capture, Utilisation, and Storage (CCUS) in ASEAN Countries Vol. II*. Jakarta: ERIA.

[12] International Risk Governance Council. (2023). (rep.). *Policy Brief: Regulation of Carbon Capture and Storage*. Geneva.

[13] Havercroft, I. (2019). (rep.). *Lessons and Perceptions: Adopting a Commercial Approach to CCS Liability*. Global CCS Institute.

[14] AECOM. (2022). (rep.). *Next Generation Carbon Capture Technology: Mobile Demonstration Plant Work Package 4*. Glasgow.

[15] Department for Business Energy and Industrial Strategy. (2020). (rep.). *CCS deployment at dispersed industrial sites.*

[16] Stigson, P., Hansson, A., & Lind, M. (2012). Obstacles for CCS deployment: An analysis of discrepancies of perceptions. *Mitigation and Adaptation Strategies for Global Change*, *17*(6), 601–619. https://doi.org/10.1007/s11027-011-9353-3

[17] Rassool, D. (2019). (rep.). *Investing in CCS: What Do Financiers Need?* Global CCS Institute.

[18] Zapantis, A., Townsend, A., & Rassool, D. (2019). (rep.). *Policy Priorities to Incentivise Large-Scale Deployment of CCS*. Global CCS Institute.

[19] Yasseri, S., & Bahai, H. (2018). System readiness level estimation of oil and gas production systems. *International Journal of Coastal and Offshore Engineering*, *2*(2), 31–44. https://doi.org/10.29252/ijcoe.2.2.31

[20] Yasseri, S. (2019). A systems engineering approach to the physical security of oil & gas installations. *International Journal of Coastal and Offshore Engineering*, *3*(3), 17–31. https://doi.org/10.29252/ijcoe.3.3.17

[21] Romasheva, N., & Ilinova, A. (2019). CCS Projects: How Regulatory Framework influences their deployment. *Resources*, *8*(4), 181. https://doi.org/10.3390/resources8040181

[22] Kothandaraman, A. (2010). *Carbon dioxide capture by chemical absorption: A solvent comparison study* (thesis). Massachusetts Institute of Technology, Mumbai.

[23] Tcvetkov, P., Cherepovitsyn, A., & Fedoseev, S. (2019). Public perception of carbon capture and storage: A state-of-the-art overview. *Heliyon*, *5*(12). https://doi.org/10.1016/j.heliyon.2019.e02845

[24] Jones, C. R., Olfe-Kräutlein, B., Naims, H., & Armstrong, K. (2017). The social acceptance of carbon dioxide utilisation: A review and research agenda. *Frontiers in Energy Research*, *5*. https://doi.org/10.3389/fenrg.2017.00011

[25] Terwel, B. W., Harinck, F., Ellemers, N., & Daamen, D. D. L. (2011). Going beyond the properties of CO2 Capture and Storage (CCS) technology: How trust in stakeholders affects public acceptance of CCS. *International Journal of Greenhouse Gas Control*, *5*(2), 181–188. https://doi.org/10.1016/j.ijggc.2010.10.001

[26[Janipour, Z., Swennenhuis, F., de Gooyert, V., & de Coninck, H. (2021). Understanding contrasting narratives on carbon dioxide capture and storage for Dutch industry using system dynamics. *International Journal of Greenhouse Gas Control*, *105*, 103235. https://doi.org/10.1016/j.ijggc.2020.103235

[27] Oraee-Mirzamani, B., Cockerill, T., & Makuch, Z. (2013). Risk assessment and management associated with CCS. *Energy Procedia*, *37*, 4757–4764. https://doi.org/10.1016/j.egypro.2013.06.385

[28] Ashworth, P. (2010). (rep.). *Communication of Carbon Capture and Storage: Outcomes from an International Workshop to Summarise the Current Global Position.*\. Global CCS Institute.

[29] Carbon Capture Coalition. (2020). (rep.). *Carbon Capture Jobs and Project Development Status.*

[30] Morgan, N. (2012). (rep.). *Policy Briefing: Carbon Capture and Storage Analysing Uncertainty*. UK Energy Research Center.

[31] Paltrinieri, N., Wilday, J., Farret, R., Hebrard, J., & Breedveld, L. (2011). 22nd Institution of Chemical Engineers. In *Carbon Capture and Storage: A Case Study of Emerging Risk Issues in the iNTeg-Risk Project* (Ser. Symposium Series No. 156). Liverpool; Hazards XXII

[32] Napp, T., Sum, K. P. S. 1 S., Hills, T., & Fennell, P. S. (2014). (tech.). *Attitudes and Barriers to Deployment of CCS from Industrial Sources in the UK*. Imperial College London.

[33] Hong, W. Y. (2022). A techno-economic review on carbon capture, utilisation and storage systems for achieving a net-zero CO2 emissions future. *Carbon Capture Science & Technology*, *3*, 100044. https://doi.org/10.1016/j.ccst.2022.100044

[34] Farajzadeh, R., Eftekhari, A. A., Dafnomilis, G., Lake, L. W., & Bruining, J. (2020). On the sustainability of CO2 storage through CO2 – Enhanced Oil Recovery. *Applied Energy*, *261*,

114467. https://doi.org/10.1016/j.apenergy.2019.114467

[35] IEA. (2012). (rep.). *A Policy Strategy for Carbon Capture and Storage*.

[36] Research Center for Greenhouse Gas Innovation. (2019). (rep.). *Experts state that barriers to carbon capture and storage are political, social, and commercial.*

[37] IEA. (2016). (rep.). *Ready for CCS retrofit: The potential for equipping China's existing coal fleet with carbon capture and storage.*

[38] European Environment Agency. (2011). (tech.). *Air pollution impacts from carbon capture and storage (CCS)*. Copenhagen.

[39] Bowen, F. (2010). Barriers to carbon capture and storage may not be obvious. *Nature Research*, *464*(7286), 160–160. https://doi.org/10.1038/464160c

[40] Fasihi, M., Efimova, O., & Breyer, C. (2019). Techno-Economic Assessment of CO2 Direct Air Capture Plants. *Journal of Cleaner Production*, *224*, 957–980. https://doi.org/10.1016/j.jclepro.2019.03.086

[41] Lichtschlag, A., Haeckel, M., Olierook, D., Peel, K., Flohr, A., Pearce, C. R., Marieni, C., James, R. H., & Connelly, D. P. (2021). Impact of CO2 leakage from sub-seabed carbon dioxide storage on sediment and Porewater geochemistry. *International Journal of Greenhouse Gas Control*, *109*, 103352. https://doi.org/10.1016/j.ijggc.2021.103352

[42] Khosroabadi, F., Aslani, A., Bekhrad, K., & Zolfaghari, Z. (2021). Analysis of carbon dioxide capturing technologies and their technology developments. *Cleaner Engineering and Technology*, *5*, 100279. https://doi.org/10.1016/j.clet.2021.100279

[43] Watson, J., Kern, F., & Markusson, N. (2014). Resolving or managing uncertainties for carbon capture and storage: Lessons from historical analogues. *Technological Forecasting and Social Change*, *81*, 192–204. https://doi.org/10.1016/j.techfore.2013.04.016

[44] Xenias, D. (2017). 19th EGU General Assembly. In *Public engagement with CCS: barriers, key issues and ways forward* (Vol. 19, p. 1812). Vienna; Cardiff University.

[45] Global CCS Institiute. (2020, July 30). Carbon capture and storage: Challenges, enablers and opportunities for deployment. Retrieved August 30, 2023,.

[46] Neill, S. P., & Hashemi, M. R. (2018). Introduction. In *Fundamentals of Ocean Renewable Energy: Generating electricity from the sea* (pp. 1–30). essay, Elsevier Academic Press.

[47] GAO. (2016). (rep.). *Technology readiness assessment guide: Best practices for evaluating the readiness of technology for use in acquisition programs and projects*. U.S. Government Accountability Office.

[48] Dunbar, B. (2015, May 6). *Technology readiness level*. NASA. https://www.nasa.gov/directorates/heo/scan/engineering/technology/technology_readiness_level

[49] Biominas Brasil. (2021, June 4). *Technology readiness level (TRL)*. https://biominas.org.br/blog/technology-readiness-level-trl-2/

[50] Yasseri, S. (2013). Subsea system readiness level assessment. *Underwater Technology*, *31*(2), 77–92. https://doi.org/10.3723/ut.31.077

[51] Yasseri, S. (2016). A measure of Subsea Systems' readiness level. *Underwater Technology*, *33*(4), 215–228. https://doi.org/10.3723/ut.33.215

[52] Yasseri, S., & Bahai, H. (2020). Case studies in estimating Subsea Systems' readiness level. *Underwater Technology*, *37*(1), 13–27. https://doi.org/10.3723/ut.37.013

[53] Bui, M., Adjiman, C. S., Bardow, A., Anthony, E. J., Boston, A., Brown, S., Fennell, P. S., Fuss, S., Galindo, A., Hackett, L. A., Hallett, J. P., Herzog, H. J., Jackson, G., Kemper, J., Krevor, S., Maitland, G. C., Matuszewski, M., Metcalfe, I. S., Petit, C., … Dowell, N. M. (2018). Carbon capture and storage (CCS): the way forward. *Energy & Environmental Science*, *11*, 1062–1176. https://doi.org/10.1039/C7EE02342A

[54] Kearns, D., Liu, H., & Chonsoli, chris. (2021). (rep.). *Technology readiness and cost of CCS*. Global CCS Institute.

[55] Haines, M. (2014). (tech.). *Assessment of emerging CO2 capture technologies and their potential to reduce costs* (Vol. 2014/TR4). IEAGHG.

[56] Freeman, B. C., & Brown, A. S. (2011). Assessment of the technology readiness of post-combustion CO2 Capture Technologies. *Energy Procedia*, *4*, 1791–1796. https://doi.org/10.1016/j.egypro.2011.02.055

[57] Global CCS Institute. (2023, August 26). *Q2 2023: CCS Facilities Update*. Global CCS Institute. https://www.globalccsinstitute.com/news-media/latest-news/q2-2023-ccs-facilities-update/

[58] Rubina, E. S., Davison, J. E., & Herzog, H. J. (2015). The cost of CO2 capture and storage. *International Journal of Greenhouse Gas Control*, *40*, 378–400. https://doi.org/https://doi.org/10.1016/j.ijggc.2015.05.018

[59] Global CCS Institute. (2015, November 15). *Recent funding of pilot-scale testing of carbon capture technologies reflects a commitment to drive down costs*. Global CCS Institute. https://www.globalccsinstitute.com/news-media/insights/recent-funding-of-pilot-scale-testing-of-carbon-capture-technologies-reflects-commitment-to-drive-down-

costs/#:~:text=Budgets%20for%20the%20Phase%20I%20efforts%20range%20from,million%2C%20with%20approximately%2080%20percent%20DOE%20cost%20share.

[60] Al-Shargabi, M., Davoodi, S., Wood, D. A., Rukavishnikov, V. S., & Minaev, K. M. (2022). Carbon dioxide applications for enhanced oil recovery assisted by nanoparticles: Recent developments. *ACS Omega*, *7*(12), 9984–9994. https://doi.org/10.1021/acsomega.1c07123

[61] Zoback, M., & Smit, D. (2023). Meeting the challenges of large-scale carbon storage and hydrogen production. *Proceedings of the National Academy of Sciences*, *120*(11). https://doi.org/10.1073/pnas.2202397120

[62] Ma, Z., Chen, B., & Pawar, R. J. (2023). Phase-based design of CO2 Capture, transport, and storage infrastructure via SIMCCS3.0. *Scientific Reports*, *13*(1). https://doi.org/10.1038/s41598-023-33512-5

[63] Xenias, D., & Whitmarsh, L. (2018). Carbon capture and storage (CCS) experts' attitudes to and experience with public engagement. *International Journal of Greenhouse Gas Control*, *78*, 103–116. https://doi.org/10.1016/j.ijggc.2018.07.030

[64] IEA - Clean Coal Center. (2018). (rep.). *Overcoming barriers to carbon capture and storage through international collaboration* (Vol. 54).

[65] Elazari, E. (2022, April 20). *The Role of International Organizations in Climate Governance*. Global Risk Insights. https://globalriskinsights.com/2022/04/the-role-of-international-organizations-in-climate-governance/

[66] Global CCS Institute. (2010). (rep.). *Global Knowledge Sharing Framework*.

[67] Global CCS Institute. (2019). (rep.). *Carbon Neutrality: Scenarios for Deep Decarbonization*.

[68] Tsai, J.-M., & Hung, S.-W. (2014). A novel model of technology diffusion: System dynamics perspective for cloud computing. *Journal of Engineering and Technology Management*, *33*, 47–62. https://doi.org/10.1016/j.jengtecman.2014.02.003

[69] Feldman, S. S. (2023). Health Information Exchange—the Value Proposition: A Case Study of the US Social Security Administration. *Health Information Exchange*, 333–349. https://doi.org/10.1016/b978-0-12-803135-3.00031-1

[70] Zhang, B. H., & Ahmed, S. A. M. (2021). Systems Thinking—Ludwig Von Bertalanffy, Peter Senge, and Donella Meadows. In *Science education in theory and practice: An introductory guide to learning theory* (pp. 419–436). essay, Springer.

[71] Kauffman, D. (1980). *Systems 1: An Introduction to Systems Thinking*. Future Systems.

[72] Guarnieri, F., & Garbolino, E. (2019). *Safety Dynamics Evaluating Risk in Complex Industrial Systems*. Springer International Publishing.

[73] Zach. (2021, March 25). *Endogenous vs. exogenous variables: Definition & examples*. Statology. https://www.statology.org/endogenous-vs-exogenous-variables/

[74] Ogland-Hand, J. D., Cohen, S. M., Kammer, R. M., Ellett, K. M., Saar, M. O., Bennett, J. A., & Middleton, R. S. (2022). The Importance of Modeling Carbon Dioxide Transportation and Geologic Storage in Energy System Planning Tools. *Frontiers in Energy Research*, *10*. https://doi.org/10.3389/fenrg.2022.855105

[75] Martin-Roberts, E., Scott, V., Flude, S., Johnson, G., Haszeldine, R. S., & Gilfillan, S. (2021). Carbon capture and storage at the end of a lost decade. *One Earth*, *4*(11), 1569–1584. https://doi.org/10.1016/j.oneear.2021.10.002

[76] Zhai, H. (2019). Advanced membranes and learning scale required for cost-effective post-combustion carbon capture. *iScience*, *13*, 440–451. https://doi.org/10.1016/j.isci.2019.03.006

[77] Takase, H., McKinley, I. G., West, J. M., Kumagai, T., & Akai, M. (2011). Advanced KMS for knowledge sharing and building confidence in CCS. *Energy Procedia*, *4*, 6202–6209. https://doi.org/10.1016/j.egypro.2011.02.632

INTERNATIONAL JOURNAL OF
COASTAL, OFFSHORE & ENVIRONMENTAL ENGINEERING IJCOE Vol.8/No. 4/Autumn 2023 (31-35)

Available online at: www. Ijcoe.org

Investigation of the effects of rubble mound structures on coastal bed profile over the Southern Coasts of Caspian Sea (Field study: Astara Port)

Sahar Javansamadi [1],Ali Karami Khaniki*[2],Abbaas Ali Aliakbar Bidokhti[3],Kamran Lari[4] ,Majid Ghodsi hassanabad [5]

[1] Department of Natural Resources and Environment, Science and Research Branch, Islamic Azad University, Tehran, Iran

[2*]Soil Conservation and Watershed Management Research Institute (SCWMRI), Tehran, Iran
Akk7239@yahoo.com

[3] Institute of Geophysics, University of Tehran, Tehran, Iran

[4] Department of Marine Science and Technology, Tehran North Branch, Islamic Azad University, Tehran, Iran

[5] Department of Marine Industries, Science and Research Branch, Islamic Azad University, Tehran, Iran

ARTICLE INFO

Article History:
Received: 16 Sep. 2023
Accepted: 02 Nov. 2023

Keywords:

Coastal bed profile
Caspian Sea
Dean's equation
Cross-shore bed profile
Rubble mound structures

ABSTRACT

Coastal protection engineering works may result in changes in characterization of the hydrodynamics and bottom topography of the near shore domain. Since measuring the changes in underlying bathymetric is very costly, developing equilibrium beach profiles which can demonstrate the important features of the bottom topography is of importance. In order to assess the bottom topography of the Caspian Sea in vicinity of Astara Port, some field measurements of beach profiles were carried out. The purpose of this paper is to investigate the influences of the breakwaters of Astara Port on beach morphological evolution in the vicinity of them to identify how the extension of breakwaters altered the sea bed topography. To describe evolving cross-shore profiles in the study area, beach profile surveys were conducted by a single-beam echo sounder. Results showed that the breakwaters considerably affected their surroundings. Furthermore, comparisons of measured beach profiles with Dean's profile model for the equilibrium beach profile illustrated that: while the Dean's profile can precisely represent the time-mean profiles in the coastal area, it must be used with care in the structure vicinity. As a result, the coefficient, A, in Dean's equilibrium equation in the front of the breakwater will be about two or three times more than as when it used for the coast without the structure. It is because of the presence of coarser grains in front of the breakwater. It is while the power term in Dean's equation is the same for both the cases without and with the structure which is 2/3.

1. Introduction

Coastal protection engineering works, such as breakwaters, influencing waves, wave-induced near shore currents, and sediment transport, are carried out to protect coasts or harbors against the effects of waves and long shore drift [19].The structures can affect bottom topography and the shoreline contour, resulting in overall and local deformations that would not evolve without the presence of them [13].Overall deformations can cause morphological evolution owing to the disturbance of long shore sediment movement, and the second ones can bring about changes in movements of sediments in the vicinity of the coastal structures during a given storm event [8,15].In an article [18] showed that the strongest coastal current prevails in the autumn season and the calm current prevails in the summer in the coastal area of Astara. 93% of the days of the year the waves come from the northeast and the prevailing current is from north to south.differences of Hydrodynamic factors cause a variety of coastal conditions in the northern and southern coastal regions of Iran. In this research, the morphodynamic classification of Iranian coasts has been investigated [17].Analysis of wind, sea Current characteristics, and wave height on the southern shores of the Caspian Sea, especially on offshore shores It was done in the north of Iran. According to the main factors Affecting the waves caused by the wind, the

atmospheric framework in the studied area with High pressure was identified as the main factor that should be considered in the formation of waves [14] . [10] showed that As the wave's steepness rises, the location of the formation of the bars moves toward the coast, and the depth of water decreases at the beginning and the ends of the bars; also, in terms of lowering in the water level with the change in the height of the waves, the position and the geometric shape of the bars will not follow a certain trend. Numerous investigations have been carried out to evaluate the effects of coastal structures on beach morphologies [15]. Identified how breakwaters with different layout alter asymmetry of the salient [1]. Based on 14 years of data, they found that the berm lowering rate was marginally larger at sea walled sections in comparison to dune/beach sections. Also, they didn't find any convincing evidence to prove the claim that seawalls had caused higher shoreline recession rates in the study area. However, measuring changes in underlying bathymetric is so expensive that numerous reliable numerical models have been developed to simulate morphological changes. As a result, many numerical studies have been performed to understand the morphological evolution around coastal structures. Since waves, wave-induced nearshore currents have decisive effects on sediment transport, these studies have placed considerable importance on correctly modelling waves and wave-induced nearshore currents. The results obtained from this approach look encouraging [2,5,9]. Furthermore, an understanding of equilibrium beach profiles may be useful in some problems of coastal engineering [7]. Using equilibrium beach profiles, which approximately demonstrate the important features of cross-shore profiles a beach, the response of beach profiles under changing hydrodynamic conditions can be shown [12].

The best known and most commonly used equilibrium beach profile form is Dean's profile, which determines the shape of equilibrium beach profile with regard to the distance from the coastline and the sediment size. The profile does not consider the effects of wave climate, and coastal currents [7,11]. Some equilibrium beach profiles have been characterized to represent cross-shore profiles subject to different conditions [3,7].

Beach profiles are likely to stay the same under long-term wave climate and persistent sediment size, which means that the long shore sediment transport is equal to zero[4]. [6] proposed the power law approach, most used form of equilibrium beach profile, but it is commonly known as Dean's profile. It can mathematically define the shape of equilibrium beach profile:

$$h=Ax2/3 \quad (1)$$

Where h is water depth, x is seaward distance from the shoreline and A is the sediment-dependent scale parameter[7].

2. Study Area

Astara port (38.4069 °N and 48.8815°E) is located at the southwest of the Caspian Sea, North of Iran (Figure 1). In 1996, Astara port was mainly built as a port for fishing, trading, and travelling. Due to the positive effects the port had on the development of the region, it has been enlarged. As a result, the northern breakwater with a length of 470 m and the southern breakwater with a length of 187 m have been built (Figure 1).

Figure 1. **Location of Astara Port**

The study area is exposed to Mediterranean climate with warm summers, moderate and rainy winters. The annual prevailing winds in the area are northerly, northwesterly, and northeasterly. The water level of the port, like that of the Caspian Sea, is currently around 27 m below the level of open seas. Since there are no tides in the Caspian Sea [16] the tidal water-level fluctuations are negligible in the port. Wave rose for study site shows that the prevailing wave direction is from the north-east. In addition, the dominating current direction is southward (Figure 2).

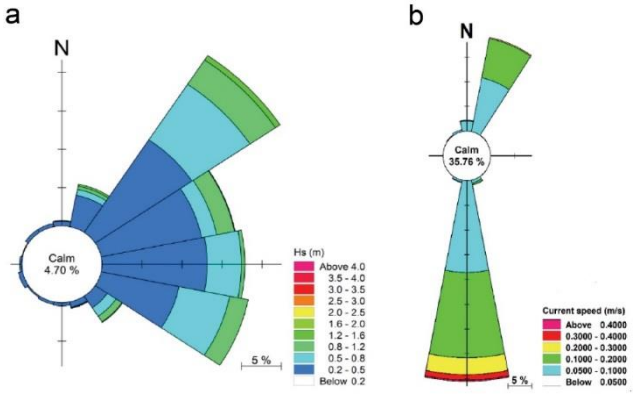

Figure 2. **(a) Wave rose and (b) current rose for study area**

The sea bed in the study area is mostly sand, with grain size changing from 0.02 to 4 mm. To investigate the effect of sediment size on the bed profile, about 22 samples were taken and tested for grain size distribution. Figure 3 shows the grain size distribution of bed sediment for samples 1-5 and 1-6 typically. Then, the average sediment size, D_{50}, was computed for all samples (Figure 4).

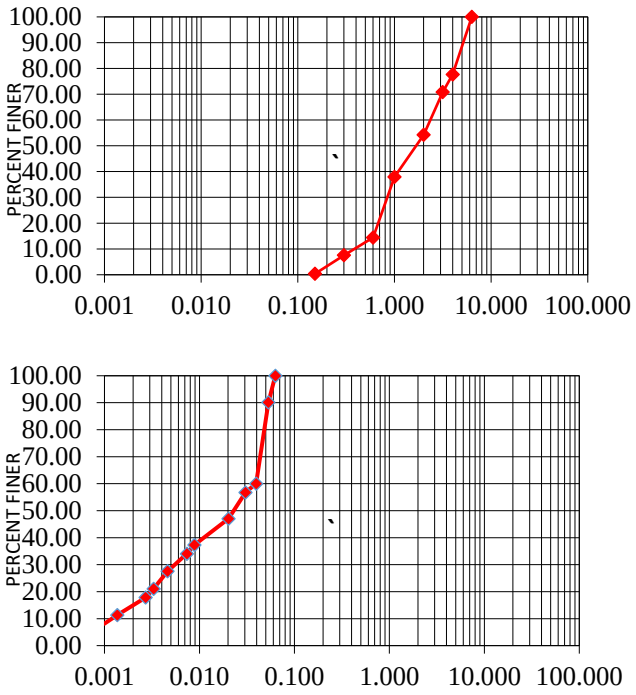

Figure 3. **Typical Grain size distribution of sediments: Samples 1-5 (left) and 1-6 (Right)**

Sample ID	D50 (mm)
1-1	0.28
1-2	1.7
1-3	0.08
1-4	0.05
1-5	1.7
2-1	0.16
2-2	0.16
2-3	0.12
2-4	0.09
2-5	0.11
2-6	0.10
3-1	0.10
3-2	0.15
3-3	0.11
3-4	0.09
3-5	0.52
3-6	3.4
4-1	0.2
4-2	0.11
4-3	0.1
4-4	0.11
4-5	0.15

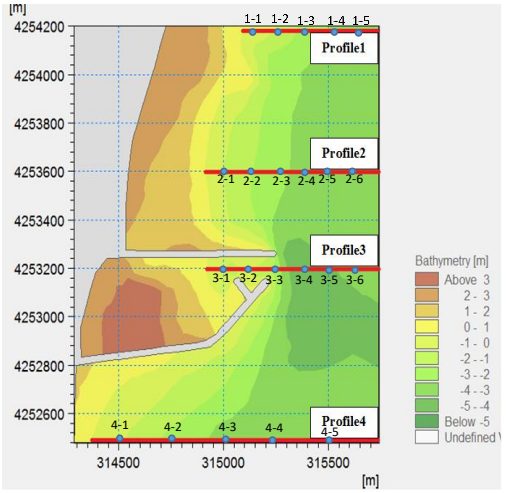

Figure 4. **Average diameter of sediment size along the Profile 1 to 4**

3. Methodology

In this study, morphological evolution in the vicinity of the breakwaters constructed in Astara Port was monitored to investigate the effects of the structures on beach morphological evolution. For this purpose, changes in the bottom topography around the structure were observed in different years. Besides, measured profiles were compared with Dean's profile in the study area. In order to assess changes in the bottom topography due to the extension of breakwaters of Astara Port, bathymetric surveys which surveyed by the Iran National Cartographic Center (INCC) in 2009, 2011 and 2012 were used. Then four cross-shore bathymetric profiles were extracted for each year to represent the cross-shore profiles of the study area (Figure 5). The data had a vertical accuracy of ± 5 cm and a horizontal accuracy of 1 m. The profiles are spaced at intervals of approximately 400 m, with an offshore extension of 1400 m.

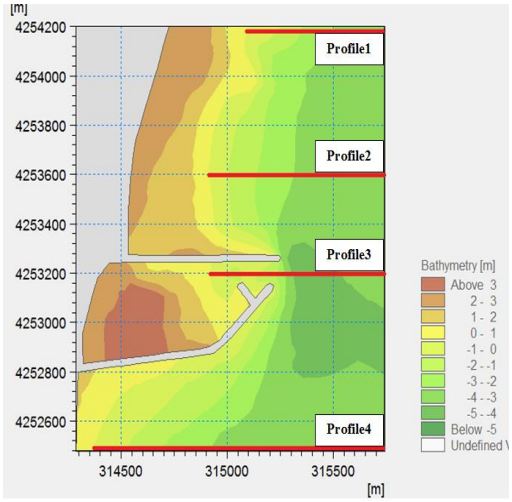

Figure 5. **Locations of transects where cross-shore profiles were measured**

4. Results

Figures 6 to 8 compare cross-shore measured profiles with relative Dean's profiles which were determined based on the best fit to measured profiles . The equations for the best-fit profiles were extracted which obey the Dean's equation with different 'A' coefficients (Figures 6 to 8). As can be seen from Figure 6, the cross-shore profiles for sections 1, 2, and 4, in the year 2009, are closed to each other which can be represented by the Dean's equation $y=A\,x^{2/3}$, where A=0.047 for these cases. While, for Section 2 which crosses the port structure, the shape of the profile is completely different. It shows a deposition area inside the port basin, and a desertion area outside the basin in front of the breakwater (Figures 6 and 9). In this case, the bed profile inside the port basin cannot be represented by the Dean's equation, while outside the basin it is well represented by Dean's equation with parameter A=0.156 (Fig 6). Figure 9 also shows an active area which extends about 700 meters from the coastline toward the sea, where the depth is about 3.7 meter and all bed profiles meet each other.Like the year 2009, the profile pattern was repeated for the years 2011 and 2012. As shown in figures 7 and 8, the bed profiles for sections 1, 2, 4 can fairly be represented by Dean's formula, however, for section 2 which crosses the port structure, the Dean's formula is only applicable to the offshore part of the profile which is steeper and completely submerged. As shown in these figures, the coefficient 'A' of Dean's formula is increasing when we're getting closer to the port structure along the coast. Especially, for the sections crosses the breakwater, the coefficient 'A' increased

rapidly. Since the A value depends on the sediment size (D), it can be concluded that the size of sediments in the neighborhood of the port structure is greater than the area located far from the port. This fact is shown in Fig.10, which is a plot of A versus D. As shown in this figure, the position on A-D plot for profiles 1, 2 and 4 (sections which are far from the port structure) are apart from for profile 3 (which is close to port breakwater).

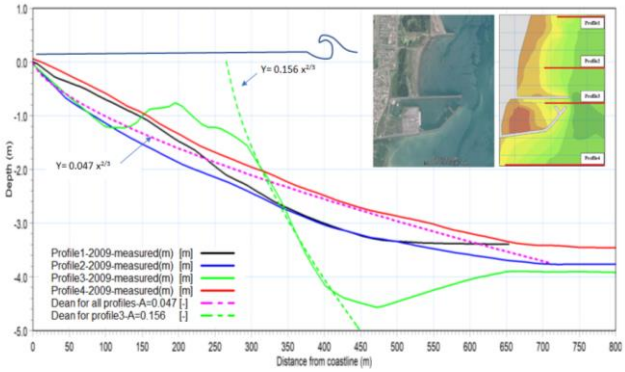

Figure 6. Measured Bed Profiles around the Astara Port (Year 2009) in Comparison with Dean's Formula

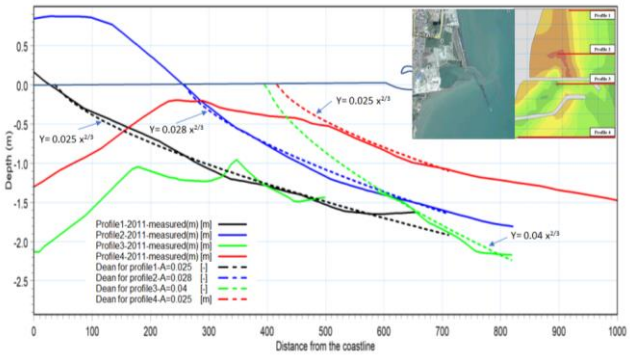

Figure 7. Measured Bed Profiles around the Astara Port (Year 2011) in Comparison with Dean's Formula

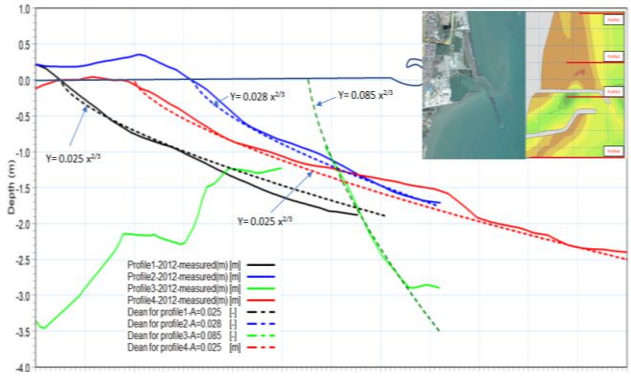

Figure 8. Measured Bed Profiles around the Astara Port (Year 2012) in Comparison with Dean's Formula

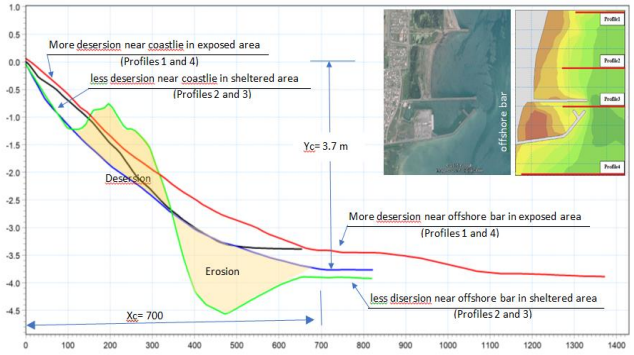

Figure 9. Erosion and Deposition in cross-shore Profiles (Year 2009)

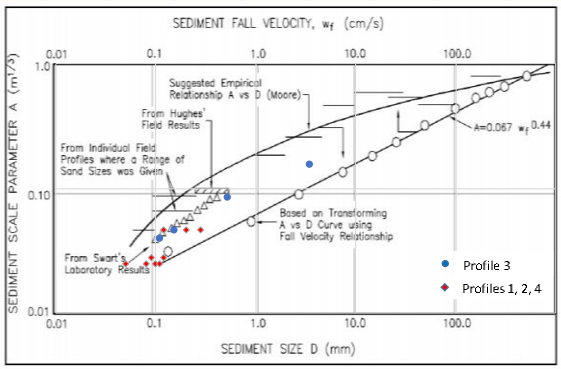

Figure 10. A-D plot for Profiles 1,2,3 (far from the structure) and Profile 3 (in front of the structure)

5. Conclusion

Coastal protection engineering works may result in changes in characterization of the hydrodynamics and bottom topography of the nearshore domain. Since measuring the changes in underlying bathymetric is very costly, developing equilibrium beach profiles which can demonstrate the important features of the bottom topography is of importance. In order to assess the bottom topography of the Caspian Sea in vicinity of Astara Port, some field measurements of beach profiles were carried out. The agreement between the profiles and the equilibrium profile described by Dean was investigated. In addition, investigating profiles in the vicinity of Astara Port showed that the breakwaters have caused the disturbance to the southward long shore sand transport, leading to beach accretion on the northern side and shoreline erosion in the lee of the structures. It can be concluded that, the Dean's formula ($y=A\,x^{2/3}$) can be applied for all parts of the coast even for the areas in vicinity of the coastal structures, while the power term in the formula is (2/3) for all cases but the coefficient 'A' for structure neighborhood is inherently more than the other areas. The shape of bed profile in structure neighborhood is steeper than the other areas which resulted from the accumulation of bigger sediments around the structure.

6. References

[1] Basco, D. R., Bellomo, D. A., & Pollock, C. (1992). Statistically significant beach profile change with and without the presence of seawalls. In *Coastal Engineering 1992* (pp. 1924-1937).

[2] Birben, A. R., Özölçer, İ. H., Karasu, S., & Kömürcü, M. İ. (2007). Investigation of the effects of offshore breakwater parameters on sediment accumulation. *Ocean Engineering*, *34*(2), 284-302.

[3] Bodge, K. R. (1992). Representing equilibrium beach profiles with an exponential expression. *Journal of coastal research*, 47-55.

[4] Bowen, A. J. (1980). Simple modes of nearshore sedimentation beach profiles and longshore bars. *The coastline of Canada*

[5] Broker, I., Johnson, H. K., Zyserman, J. A., Ronberg, J. K., Pedersen, C., Deigaard, R., & Fredsoe, J. (1995). Coastal profile and coastal area morphodynamic modelling. MAST 68-M Final Workshop, Gdansk.

[6] Bruun, P. (1954). *Coast erosion and the development of beach profiles* (Vol. 44). US Beach Erosion Board.

[7] Dean, R. G. (1991). Equilibrium beach profiles: characteristics and applications. Journal of coastal research, 53-84.

[8] DOLPHIN, T., TAYLOR, J., VINCENT, C., BACON, J., Pan, S., & O'CONNER, B. R. I. A. N. (2005). Storm-scale effects of shore-parallel breakwaters on beaches in a tidal setting (LEACOAST). In Coastal Engineering 2004: (In 4 Volumes) (pp. 2849-2861).

[9] Du, Y., Pan, S., & Chen, Y. (2010). Modelling the effect of wave overtopping on nearshore hydrodynamics and morphodynamics around shore-parallel breakwaters. Coastal Engineering, 57(9), 812-826.

[10] Ghanbari, F., Adjami, M., & Ataei H, S. (2019). An Analytical Study on the Formation of Submerged Bars in the Southern Coasts of Caspian Sea. International Journal Of Coastal, Offshore And Environmental Engineering, 4(3), 1-8.

[11] González, M., Medina, R., & Losada, M. A. (1999). Equilibrium beach profile model for perched beaches. Coastal Engineering, 36(4), 343-357.

[12] Holman, R. A., Lalejini, D. M., Edwards, K., & Veeramony, J. (2014). A parametric model for barred equilibrium beach profiles. Coastal engineering, 90, 85-94

[13] Kristensen, S. E., Drønen, N., Deigaard, R., & Fredsoe, J. (2013). Hybrid morphological modelling of shoreline response to a detached breakwater. *Coastal Engineering*, *71*, 13-27.

[14] Lama, G. F. C., Sadeghifar, T., Azad, M. T., Sihag, P., & Kisi, O. (2022). On the Indirect Estimation of Wind Wave Heights over the Southern Coasts of Caspian Sea: A Comparative Analysis. Water 2022, 14, 843.

[15] Jackson, N. L., Harley, M. D., Armaroli, C., & Nordstrom, K. F. (2015). Beach morphologies induced by breakwaters with different orientations. Geomorphology, 239, 48-57.

[16] Ranjbar, M. H., & Hadjizadeh Zaker, N. (2018). Numerical modeling of general circulation, thermohaline structure, and residence time in Gorgan Bay, Iran. *Ocean Dynamics*, *68*, 35-46.

[17]Shiea-Ali, M., & Valipour, A. (2021). Morphodynamic Classification of Beaches in some parts of the Iranian Coasts. International Journal Of Coastal, Offshore And Environmental Engineering, 6(3), 26-39.

[18]Sh.Hazrati, M.Torabi, K. Lari, A. A.Bidokhti, (2018). Numerical simulation of coastal currents caused by wind on the coast of Astara port. Journal of Meteorology and Atmospheric ciences,271-258.

[19] Tang, J., Lyu, Y., Shen, Y., Zhang, M., & Su, M. (2017). Numerical study on influences of breakwater layout on coastal waves, wave-induced currents, sediment transport and beach morphological evolution. Ocean Engineering, 141, 375-387.

INTERNATIONAL JOURNAL OF
COASTAL, OFFSHORE & ENVIRONMENTAL ENGINEERING IJCOE Vol.8/No. 4/Autumn 2023 (36-48)

Available online at: www. Ijcoe.org

Tidal components along the north of Oman Gulf and Persian Gulf

Maryam Soyuf Jahromi[1*]

[1*] *Assistant Professor of physical oceanography, Department of Nonliving Resources of Atmosphere and Ocean, Faculty of Marine Science and Technology, University of Hormozgan, Bandar Abbas, Iran; soyufjahromi@yahoo.com.au*

ARTICLE INFO

Article History:
Received: 05 Oct. 2023
Accepted: 16 Jan. 2024

Keywords:
Tides
Tidal constituents
Persian Gulf
t-tide Library
Matlab

ABSTRACT

This study concentrates on the 61 tidal constituents of 17 stations on the north of Oman Gulf (OG), Strait of Hormuz (SH) and Persian Gulf (PG). Five-years tidal data (2014-2018, 30-minutes intervals) was achieved by Iran National Cartographic Center to calculate mean levels of stations. Then, t_tide library was used to calculate 61 tidal constituents by 95% of confidence in Matlab for 2018 data. Then, they sorted by the magnitude of the amplitude to express the most significant ones in each stations. Results shows that the mean levels of the northwest and northeast of PG are mirror images. Although the major diurnal and semidiurnal tidal constituents of 11 stations are M_2, K_1, S_2 and O_1, by changes in order of importance; in 6 stations, N_2 constituent is more important than O_1. These exceptions go back to the stations of SH and northwest of PG, which shows the importance of the SH bending and the shallowing of the northwest of PG. Moreover, the top ten components of all stations are not 10 unique components and they include 21 components. Due to the Form factor, F, all the studied stations are mainly mixed semidiurnal type. The predicted t-tide tides show small errors compare with the original ones. The results also showed that the range and components of harmonic astronomical tides are influenced by local geography. On the head of PG, the Emam Khomeini's tides is sharp due to the shallow water, and the semidiurnal components (S_2 and N_2) are much stronger than the diurnal components (O_1 and P_1). The Pol Port's tides is effected by narrowing of SH. Therefore, in some ports, non-tidal parameters such as geographical shape or shallow water are effective while considering astronomical components of moon and sun.

1. Introduction

For thousands of years, tides have been so important economically and scientifically that have entered our everyday language, and a saying like "time and tide wait for no one" is a clear example. Tide is important for navigation and ocean mixing. In the vertical mixing of coastal waters with a horizontal scale of 10 km or less and a time interval shorter than 24 hours, tides plays an effective role [1]. Tides can suspend bed sediments even in deep oceans. In addition, it can cause internal waves on seamounts, continental slopes, and midoceanic ridges, which dissipate lethal energy. In tidal history, real oceanic tides are considered stable because of their close association with astronomical motions [2]. Since the earth's crust is elastic and rotates counter-clockwise around its axis [3], due to the difference in the gravity of the moon, sun, and other celestial bodies, the earth's crust is bent under the influence of the tidal potential [4] and as a result, the ocean fluctuates semidiurnal, diurnal or with other frequencies.

In classical analysis, it is customary to decompose the recorded tidal observations into its components, and the tidal signal is modeled as a finite sum of a sinusoidal terms with specific frequencies, related to astronomical parameters. These parameters are related to many factors such as latitude, the north deviation of the moon/sun from the equator, the hour angle of the moon/sun, the deviation of the earth's rotation axis, the inclination of the earth's rotation axis with respect to the stars, the rotation of the plane of the celestial sphere, and the temporal variations of the elliptic inclination of the earth's rotation in the plane of the celestial sphere and the angle of the moon's ellipse in a plane depend on the plane of the celestial sphere [5-7]. These processes cause changes in tidal potential.

Fourier analysis is used to determine frequencies of tidal spectrum. The spectrum does not look like the oceanic wave spectrum. Oceanic waves have all

possible frequencies by a continuous spectrum while tides have precise discontinuous frequencies. It consists of discrete lines related to astronomical motions and harbor properties. Doodson (1922) [8] expanded tidal potential as Fourier series using the cleverly chosen frequencies, leads to an elegant decomposition of tidal constituents into groups with similar frequencies and spatial variability. Doodson's expansion included 399 constituents, of which 100 are long period, 160 are daily, 115 are twice per day, and 14 are thrice per day. Although most constituents had very small amplitudes, but the amplitude accuracy of 10^{-3} of the largest term requires at least 39 frequencies be determined.

The Standard list of tidal constituents was prepared by Mr. Bernard Simon of SHOM (Service hydrographique et océanographique de la marine) and Cdr John Page of the UKHO (The United Kingdom Hydrographic Office) on behalf of IHO (The International Hydrographic Organization) Tidal Committee, now it is called the Tide, Water Level and Current Working Group (TWCWG) [9]. By evolving tides at diverse rates, there is not sometimes any apparent relationship to astronomical force [10-13] and may change major diurnal and semidiurnal tides (eg. Eastern Pacific [14], Gulf of Maine [15], North Atlantic [16-17], China [18-19] and Japan [20]).

Non-tidal variability introduces large errors into the calculated amplitudes and phases of weaker tidal constituents. The weaker tides have amplitudes smaller than variability at the same frequency due to the other processes such as wind set up and currents near the tide gauge.

This research is planned to examine the tidal constituents on major ports along the north Oman Gulf (here after, OG) towards Persian Gulf (here after, PG). These basins have different tidal variability that may affects their tidal constituents.

The tidal circulation in PG was modeled by a homogeneous two dimensional shallow-water model with free surface and forced by seven tidal components at its southern boundary [21]. The model accurately reproduced the tidal phase and amplitude observed at 42 tidal gauges in the region. This accuracy was attributed to the presence of seven components which are able to interact nonlinearly. The amphidromic points were also well positioned by the model due to a proper choice of bathymetry. The tidal currents could be strong in the Straits of Hormuz (here after, SH) and in shallow areas; thus they would have an effect of the hydrology of the region. The residual currents were weak so that they were negligible for the large-scale circulation on long periods. Finally, the sea-surface elevation forecast by the model was in close agreement with *insitu* measurements of pressure, performed during the GOGP99 experiment [21].

Akbari et al., (2016) [22] were also simulated three tidal semidiurnal (M_2, S_2, K_2) and diurnal (K_1, O_1, Q_1) amplitudes in PG and OG by FVCOM (Finite Volume Coastal Ocean Model). They clearly showed that the different characteristics of PG and OG. The semidiurnal constituents (M_2, S_2, K_2) has two amphidromic points while diurnal constituents (K_1, O_1, and Q_1) had only one amphidromic points on PG. None of them had amphidromic points on OG. The tide simultaneously happens on OG is unlike PG. The model showed that tides of PG is a constant wave with two semi-diurnal and one diurnal amphidromic point. But tides of OG and the Arabian Sea is a progressive wave that moves on surfaces. The most important semidiurnal and diurnal components in the entire domain was M_2 and k_1 [22].

As can be seen, there are few near-shore studies of various components on PG, OG and SH. This study examines the components (61 constituents) near the coast of PG and OG by a library function named t-tide. These components will be checked on different ports of area to see if they have non-tidal effects by their geometric position.

2. Materials and Methods

2.1. Study area

The study area (48-62°E, 22-30°N) is a coastal area along the north of OG and PG with their connection through SH. Coastlines of the study area achieved by Iranian Army Geographic Agency as a shape file with the resolution of 30 seconds and plotted by ArcGIS 9.2 [23] software (Figure 1). The study area divided into three parts: OG, SH and PG. PG also divided into two parts of northeast and northwest because of its geometric shape.

OG (also named Macran or Mecran in native language), is a kind of strait (not an actual gulf) that connects the Arabian Sea to the SH which then runs to PG. OG is linked from three sides to the land by depths less than 1000 m and to the open ocean on the other side by depths more than 3000 m [24].

PG itself is a semi-enclosed marginal sea by total area of 240,000 km^2 [25], completely located on a continental shelf and downhill of OG. PG is a water catchment area drawn from the northwest to the southeast. Its length is 990 km while the width differs from 56 km to 338 km by the mean depth of 35 meters [1]. Its morphology is asymmetrical and the coastal slope is more relaxed on the southern coast than the northern coast [25]. SH, a curved waterway, separates Iran's plateau from the Arabian Peninsula and links the PG waters to OG and the Indian Ocean (here after, IO). Since PG is located on the subtropical high-pressure-zone, it is characterized by low precipitation (0.07–0.1 m yr^{-1}[26]) and high aridity, resulting high evaporation rates (above 2 m yr^{-1} [27]; 1.4–2.1 m yr^{-1} [28-29]), 1.5 meters of the surface in a year [30-33]) by seasonal Sea Surface Temperature (SST) changes [34]. High precipitation is rare in this area [35-36]. This makes PG as one of the most saline water of the world (36.6 to

40.6 [37]) because of high evaporation, less precipitation (less than 5 mm yr^{-1}) and less river inflow

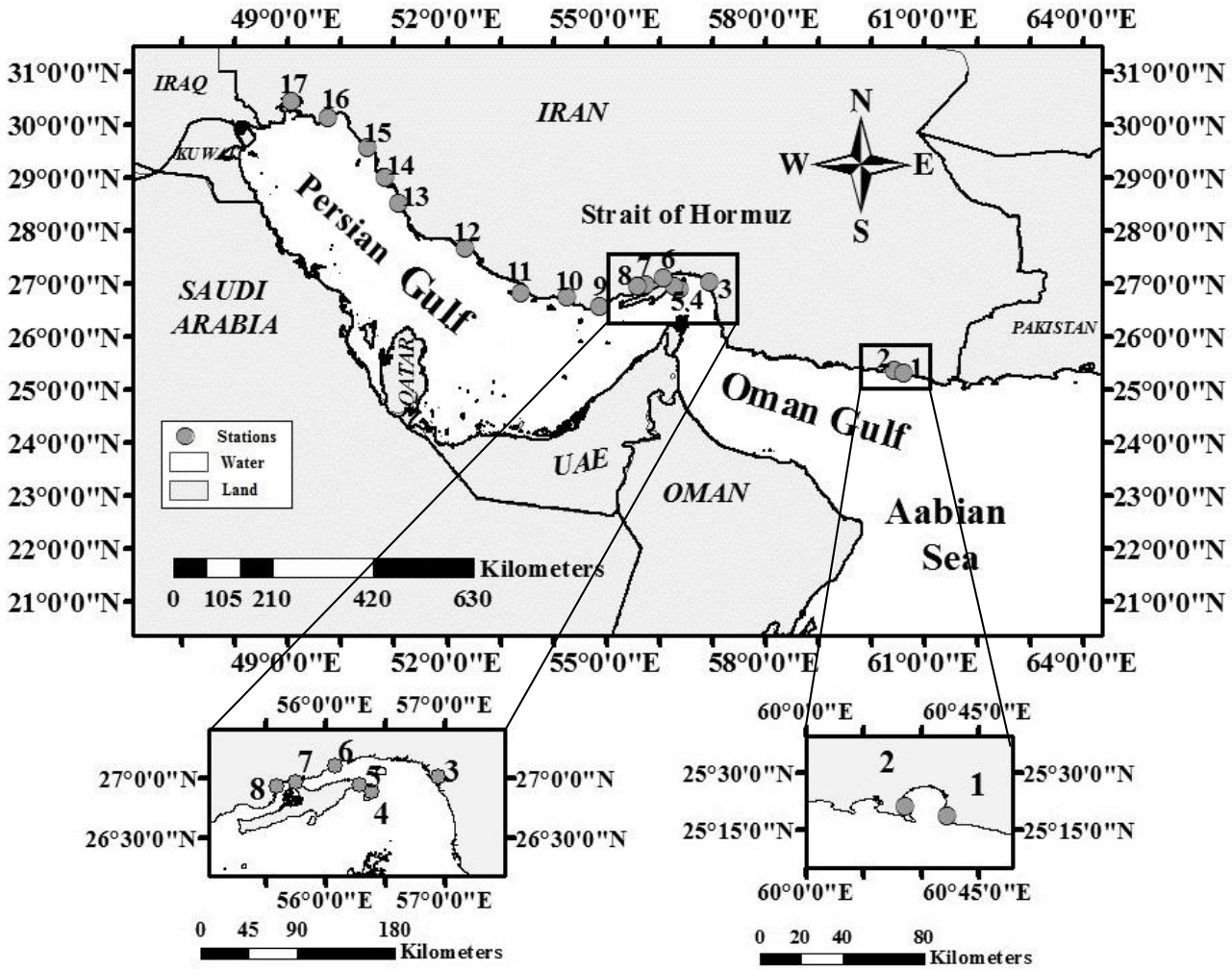

Figure 1. The study area. Oman Gulf (OG), Strait of Hormuz (SH), and Persian Gulf (PG). Gray circle marks are tidal stations (Table 1). The map is generated by ArcGIS [23] and the coastlines are achieved by Iranian Army Geographic Agency.

(0.15 m yr^{-1} [29]). The salinity is higher near the southern part [1, 32]. The saline water forms a very dense water especially in early November, when the air temperature decreases and wind speed increases [37]. It can also make some mesoscale eddies by the diameters less than 50 meters [38]. The dense flow of PG travels to OG by seasonal changes [39-43] to depths of 150 to 350 meters [44] through the south of SH. It makes changes on the thermoclines of OG [45] and deepen it to 1200 meters [46]. The less saline water of OG enters PG through the north of SH and replaces the outflow of PG [44, 47] for equilibrium [48]. This water is warmer than surrounding waters [49-50].

Tides are complicated on PG and OG. Tides of PG co-oscillate with SH while tides of OG co-oscillate with the Arabian Sea [1] and they make different tidal conditions in PG, SH and OG [51]. Due to the complex geometric shape of the coastline, tides of PG fluctuates [52] and has potential extracted energy [53]. PG has a diurnal and semidiurnal fluctuations, which initially emitted energy from SH into OG [52]. The tidal patterns of PG change from semidiurnal to diurnal tides [1]. The tidal range is more than one meter (three meters on the head of PG and one meter on the other parts) [54]. The dimensions of PG are such that the resonance amplification of the tides occur [1]. Therefore, PG tides are kinds of standing tidal waves [1] by different amphidromic points (nodes) of constituents. There are two amphidromic points for semidiurnal constituents (M_2 and S_2) and one amphidromic point for diurnal constituents (K_1 and O_1) [55-57]. The magnitude of M_2 is approximately 0.3 m to 0.5 m at each point of PG and its maximum is 0.8 m to 0.9 m at the head of PG and near SH. The magnitude of S_2 is about 30% of M_2. The O_1 amphidromic point is in the north of Bahrain by the amplitude of about 0.3 m. The K_1 amphidromic point is near Bahrain by the amplitude of about 0.5 m on the head of PG [52]. Near the amphidromic points of the diurnal components (K_1 and O_1), where the diurnal tidal component is zero, it is the semidiurnal tidal type, and near the amphidromic points of the semidiurnal components (M_2 and S_2), tides is diurnal [21]. According to the information of the National Oceanic and Atmospheric Administration (NOAA) organization, the next effective recorded

components of the world are M_4, N_2, M_6, MK_3, S_4, MN_4, NU_2, S_6, MU_2, $2N_2$. If PG and GO assumed as a unit basin, the longitudinal axis of the area must be considered as a channel with two gaps that may affect the independent tides, where the phase of the tide-generating force would depend upon the longitudinal direction of this unified basin [51].

2.2. The tidal data

Seventeen tidal stations were chosen on the north of OG, SH and PG (Figure 1). Two stations were located on OG (Station 1-2: Chabahar and Konarak), six stations are located on SH (Station 3-8: Bandzak, Larak, Bahman Port, Shahid Rajaee Port, Pol Port, and Khamir Port), four stations are located on the northeast of PG (Station 9-12: Lengeh Port, Charak Port, Lavan, and Taheri) and five stations are located on the northwest of PG (Station 13-17: Ameri Port, Bushehr, Genaveh Port, Butaheri, and Emam Khomeini Port), respectively. Table 1 shows the location of station.

Table 1. Tidal stations of the study along the northern coasts of OG, SH and PG

Basin		Station No. and Name	Longitude (°E)	Latitude (°N)
Oman Gulf (OG)		St. 1 Chabahar	60.6165619	25.3133678
		St. 2 Konarak	60.4328461	25.3552799
Strait of Hormuz		St. 3 Bandzak	56.9478073	27.0106392
		St. 4 Larak	56.3899193	26.8866272
		St.5 Bahman Port	56.2816048	26.9481812
		St. 6 Shahid Rajaee Port	56.0767288	27.1017857
		St. 7 Pol Port	55.7470436	26.9729309
		St. 8 Khamir Port	55.5921097	26.9380035
Persian Gulf (PG)	North-East	St. 9 Lengeh Port	54.8850327	26.5486584
		St. 10 Charak Port	54.2820778	26.7251301
		St. 11 Lavan	53.4027261	26.8010977
		St. 12 Taheri	52.3495789	27.6610126
	North-West	St. 13 Ameri Port	51.0914993	28.5146675
		St. 14 Bushehr	50.8374710	28.9896507
		St. 15 Genaveh Port	50.5117722	29.5597763
		St. 16 Butaheri	49.7747765	30.1060658
		St. 17 Emam Khomeini Port	49.0720100	30.4219837

Tidal information was achieved by Iran National Cartographic Center, Water Management and Tidal Affairs [58] by every 30 minutes' interval for five continuous available years (January 1, 2014 to December 31, 2018). Mean Level (ML) achieved by the average of these five years for each station. Since long-term data are affected by the harbor modifications [59-64] or changes of internal tide [65-66], only one-year data (2018) was used to analysis tidal constituents.

2.3. Data Analysis

The tidal signal is simulated as the sum of finite sets of sinusoids at specific frequencies related to astronomical parameters. Since each tidal constituent is assumed to be a harmonic function and couched in the cosine term, it can be rewrite in a vectorization form of a time series (Eq. 1) as formulated by [67]:

$$\varepsilon(t) = \Sigma_{i=0}^{n} H_i^{'} \cos(E_i^{'} - g_i) \quad (1)$$

Consequently, the number of parameters is related to the number of used (significant) constituents. The t_tide Matlab library allows the calculation of various tidal constituents by the projection of series of harmonic functions on the data. t_tide library was written first on January 2011 [68], and then revised [69]. It is available online [70] and used in other recent studies [71-75].

In this research, the first 61 significant constituents are used. Therefore, a set of programs has been rewritten in MATLAB [76] to perform the harmonic analysis for each station in 2018. This library is based on the Fortran based tidal packages developed for the Canadian government [77]. Outputs of the t_tide library consists of 61 tidal constituents as SSA, MSM, MM, MSF, MF, ALP1, 2Q1, SIG1, Q1, RHO1, O1, TAU1, BET1, NO1, CHI1, PI1, P1, K1, PHI1, THE1, J1, SO1, OO1, UPS1, OQ2, EPS2, 2N2, MU2, N2, NU2, M2, MKS2, LDA2, L2, S2, K2, MSN2, ETA2, MO3, M3, SO3, MK3, SK3, MN4, M4, SN4, MS4, MK4, S4, SK4, 2MK5, 2SK5, 2MN6, M6, 2MS6, 2MK6, 2SM6, MSK6, 3MK7, M8, M10 with frequencies ranging from 0.0015 (MM constituents) to 0.3220 (M8 constituents) cycles per hour [69] (hereafter cph). It was also used the shallow water constituents [78-79] for OG and PG which was not previously used on the documents of this area.

Frequencies, amplitudes and errors for each constituent on each station was calculated by the 95% of confidence intervals (here after 95% CI). Then, tidal constituents sorted by the magnitude of the amplitude to expresses the most significant constituents of the stations.

New tides were also made according to the extracted 61-components to calculate the difference between the predicted tides and the original ones [58] for seven selected stations (Station 1: Chabahar, Station 4: Larak, Station 8: Khamir Port, Station 9: Lengeh Port, Station 12: Taheri, Station 14: Bushehr, Station 17: Emam Khomeini Port). Since Mean level on PG have shown monthly [80] and seasonally [81] changes, therefore, the predicted water levels by components are corrected by the mean achieved water level of the time series of 2014-2018 for each station.

Form factor (F) was also calculated to classify stations according to the nature of tides as Eq. 2 [82-84]:

$$F = \frac{K_1 + O_1}{M_2 + S_2} \quad (2)$$

where the symbols of the constituents indicate their respective amplitudes. Type of tide was determined as diurnal, semidiurnal and mixed by F factor (Table 2).

Table 2: The classification of tides due to the form factor values, F [82-84].

Value of F	Type of tide
0-0.25	Semidiurnal
0.25-1.5	Mixed, mainly semidiurnal
1.5-3	Mixed, mainly diurnal
>3	Diurnal

3. Results and Discussion

3.1. The tidal times series

Figure 2 shows the mean value of stations (2014-2018). It is obvious that Mean Level (ML) is not constant; it is less on OG, becomes higher in SH, fall down in the northeast of PG and again rises on the northwest of PG. The highest values are referred to Emam Khomeini Port (2.94 m) located on the northwest of PG (Station 17) and Pol Port (2.54 m) located on the SH (Station 7). Emam Khomeini Port is a shallow port, and in other studies such as [85], its tidal range was reported large in compared with other regions of PG. Pol Port, which is the shortest distance between Iran's southern coast line and Qeshm Island, experiences high values of tides due to the narrowness of the area, which is in agreement with studies such as [53] and [86].

The lowest one is Lavan (0.96 m) located on the northeast of PG (Station 11, Figure 2). The northwest and northeast side of PG evokes a kind of mirror image in the mind in terms of tidal mean levels.

Figure 3 represents the comparisons of 17 stations for the first solar month of 2018 (January 1, 2018-January 31, 2018). Full moon was on 2 and 31 and new moon was 17 of January 2018 during this month. As it is obvious, tidal heights of stations, located on OG, are approximately small. The SH tidal ranges are higher. PG shows different styles. On the northeast, tidal ranges are very small (Table 3), but it becomes higher as it travels into the head of PG and it reaches to the highest value on the 17th station, Emam Khomeini Port (5.151 m).

Table 3. Tidal stations of the study along the north coasts of OG, SH and PG.

Basin		Station No. and Name	Min. (m)	Max. (m)	Range (m)
Oman Gulf (OG)		St. 1 Chabahar	-0.236	2.896	3.132
		St. 2 Konarak	-0.022	3.065	3.087
Strait of Hormuz (SH)		St. 3 Bandzak	0.045	3.959	3.914
		St. 4 Larak	0.072	3.222	3.15
		St.5 Bahman Port	-0.180	3.588	3.768
		St. 6 Shahid Rajaee Port	-0.159	3.951	4.11
		St. 7 Pol Port	-0.075	4.526	4.601
		St. 8 Khamir Port	-0.185	4.578	4.763
Persian Gulf (PG)	North-East	St. 9 Lengeh Port	0.011	2.629	2.618
		St. 10 Charak Port	0.107	2.200	2.093
		St. 11 Lavan	0.047	1.744	1.697
		St. 12 Taheri	-0.027	1.953	1.98
	North-West	St. 13 Ameri Port	0.285	2.264	1.979
		St. 14 Bushehr	0.133	2.214	2.081
		St. 15 Genaveh Port	0.303	2.701	2.398
		St. 16 Butaheri	-0.039	3.313	3.352
		St. 17 Emam Khomeini Port	-0.176	4.975	5.151

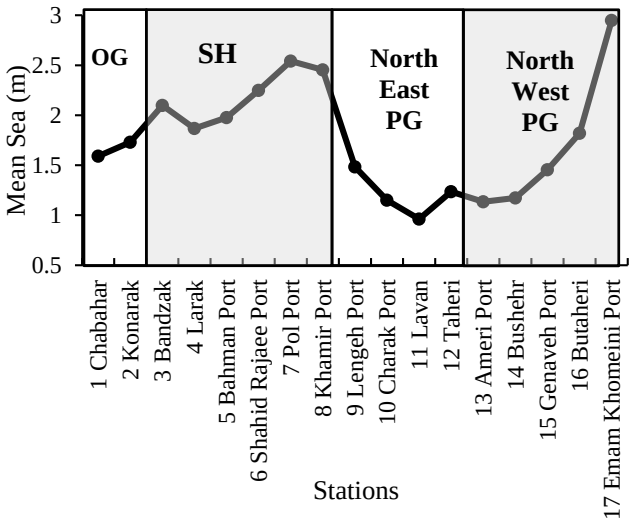

Figure 2. The Mean Level of each Station (January 1, 2014 to December 31, 2018) calculated by tidal data [58].

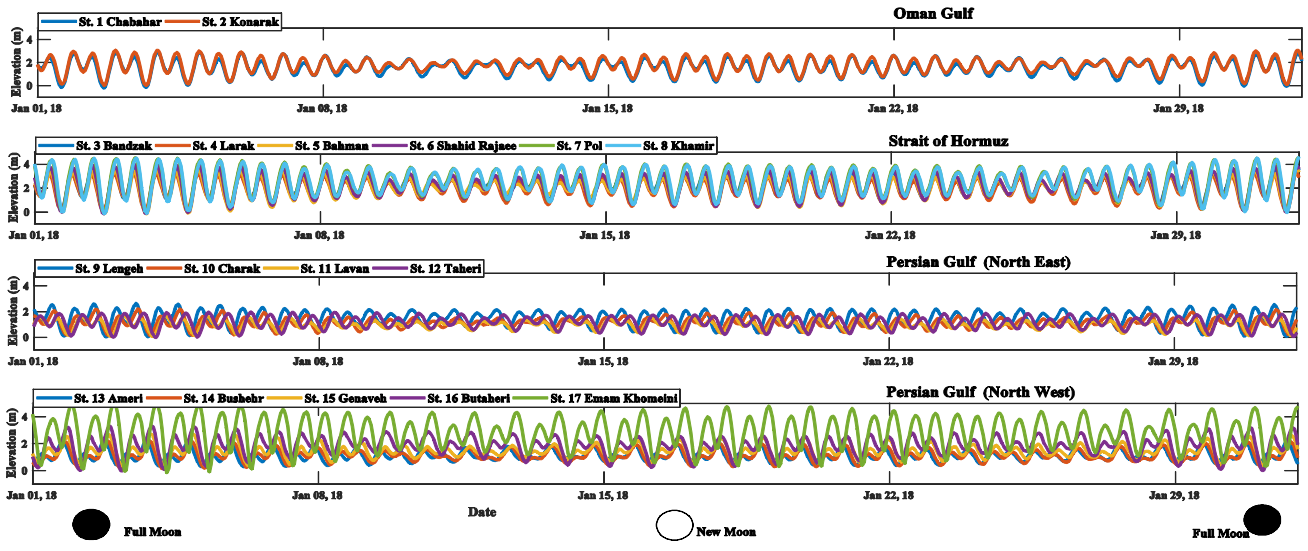

Figure 3. Tides in January 1, 2018 to January 31, 2018. The tide information was achieved by [58], with 30 minutes' interval.

The results of a one-year (2018) t-tide analysis from the Iran National Cartographic Center, Water Management and Tidal Affairs [58] and the predicted t-tide [69] tides by 61 tidal constituents have been prepared for seven random stations (Chabahar, Larak, Khamir Port, Lengeh Port, Taheri, Bushehr and Emam Khomaine Port) located on OG, SH and PG on Figure 4. It is obvious that the two-time series (the original time series and the predicted one by 61 constituents) have small differences.

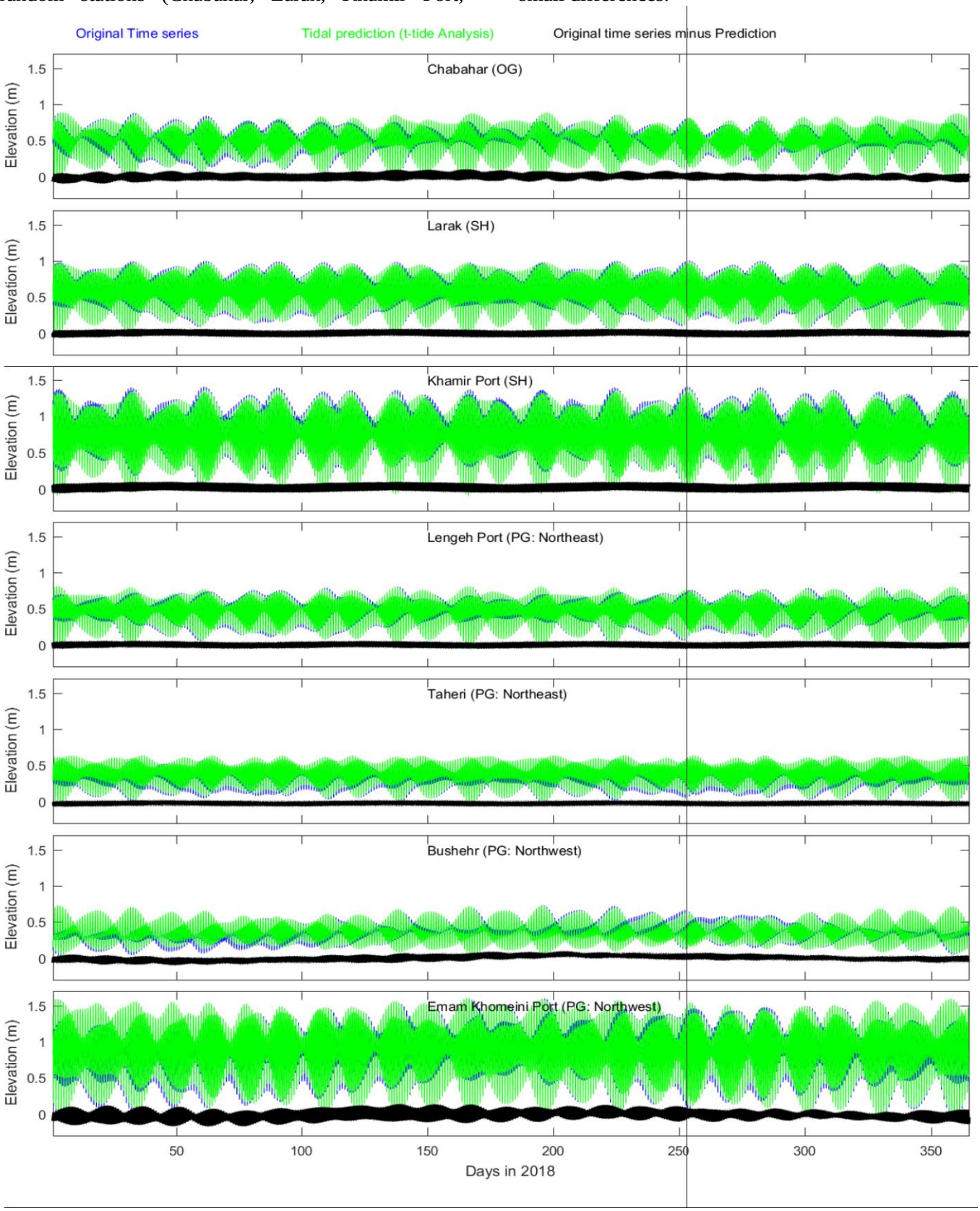

Figure 4. The original (blue) and predictional (green) tidal amplitudes (in meters) and their differences (origin-prediction) (black) for Chabahar (located on OG), Larak and Khamir Port (located on SH), Lengeh Port and Taheri (located on the northeast of PG), Bushehr and Emam Khomaine Port (located on the northwest of PG) for 2018.

The difference between the actual tide and the predicted tide in all stations is less than 0.2 meters. This difference is even less than 0.1 meters in stations like Lark, Langeh Port, Taheri and Bushehr. Comparing Figure 2 and Figure 4 shows that the water level of these stations are insignificant. In a station like Emam Khomeini Port, which has a significant tidal range, the predicted tide with 61 components has a significant error, and therefore, more components should be considered in the construction of Emam Khomeini tides especially in spring tides.

3.2. The tidal constituents

Amplitude of each tidal constituent are provided on Figure 5. The important point of Figure 5 is the discreteness of the frequency of the components, which is acceptable in the characteristics of tides.

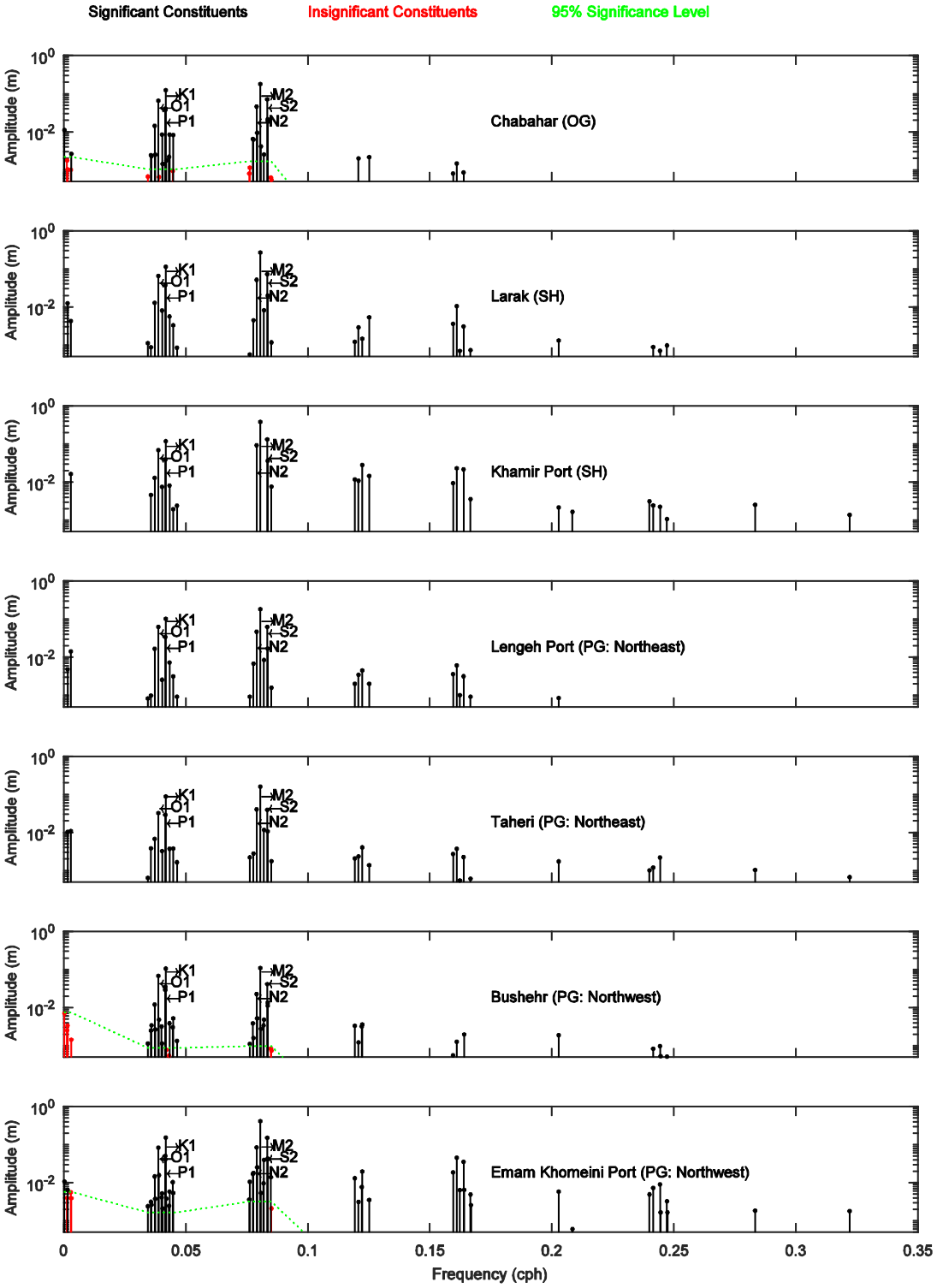

Figure 5. The predicted components of the selected station for Chabahar (located on OG), Larak and Khamir Port (located on SH), Lengeh Port and Taheri (located on the northeast of PG), Bushehr and Emam Khomaine Port (located on the northwest of PG) by t-tide library for 2018.

By the comparison of stations, it can be clearly seen that the tidal components in different stations do not have the same values and their types may also differ from one station to another. The main components (K_1, O_1, P_1, M_2, S_2, and N_2) with a frequency less than 0.1 cph in all stations are of the order greater than 10^{-2} m. Components with a frequency of more than 0.2 cph are variable in each station and some components may not be seen in some stations in even the order less than 10^{-2} m.

Table 4 shows the first ten tidal components at each station. It can be seen that the tidal components M_2, S_2, K_1, and O_1 are the top four components in ten stations. There are also seven exception stations that are related to SH and PG. In the Bandzak, Shahid Rajaei Port, Pol Port and Khmir Port stations on SH, the O_1 component is less important than the N_2 component, and N_2 occupies the fourth rank in the components. In the northeast of the PG, the N_2 component reaches the third level of importance at Taheri station. In the northwest of PG, in Emam Khomeini Port station (station 17), the N_2 component has the fourth position and the O_1 component has the fifth position. In Butahari port (station 16), component S_2 ranks fifth, and components M_2, K_1, O_1, and N_2 occupy the positions of the first to fourth ranks, respectively.

These exception stations go back to SH and northwest of PG, which shows the importance of the bending of SH and the shallowing of the northwest of PG. Emami et al., (2019) showed that the shape of the coastline is effective in the tidal pattern [86]. This study confirm that the type of tidal component is different, especially in SH because of its bend which is in agreement with [87].

From the fifth to the tenth component, there are many changes in the type of important components' rank (Table 4). The top ten components of stations include 21 components in total. If we consider these 21 components, the importance of the components changes again.

Figure 6 shows the classification of stations according to the region and type of importance. It can be seen that some of the components are not prioritized in some stations, so the investigation of one station can be different from another station and cannot be generalized.

In many ports of the world, the tide is non-linear and many other components of the tide become important. On the head of PG, it can be seen that the tidal waves in Emam Khomeini port (Station 17) are very sharp (Table 3 and Figure 6) due to the shallowing of the area and after the M_2 and K_1 components, the semi-diurnal S_2 and N_2 components are stronger than the diurnal components of O_1 and P_1 (Table 4). Other components of the order of seven to ten are also semidiurnal or quarterdiurnal. In extreme cases, the incoming waves steepens so much the leading edge is nearly vertical, and the wave propagates as solitary wave and can form a tidal bore. These tides steepen and become non-linear.

The calculated t-tide amplitudes of four major semidiurnal (M_2, S_2) and diurnal (O_1, K_1) constituents (as reported by [1, 21-22]) is shown on Figure 6. At some stations (Bandzak, Shahid Rajaei Port, Pol Port, Khamir Port, Taheri, Ameri Port, Bushehr, Butaheri and Emam Khomeini Port), one of these constituents is missing as the four top tidal constituents.

3.3. F factor

Figure 7 also shows the form factor, F, according to Eq. 2, for the stations. The comparison of Table 2 and Figure 7 clearly shows that in no station the F factor is greater than 1.5 m and none of them are less than 0.25, therefore, therefore, all the studied stations on Iranian coasts are mainly mixed semidiurnal tides.

Table 4. The first 10 top tidal constituents achieved by the tidal analysis of 2018 for stations by at-tide along the north coasts of OG, SH and PG

Basin		No. Stations Names	Order of Importance									
			1	2	3	4	5	6	7	8	9	10
Oman Gulf (OG)		1 Chabahar	M2	K1	S2	O1	N2	P1	K2	Q1	SSA	NU2
		2 Konarak	M2	K1	S2	O1	N2	P1	K2	NO1	Q1	MU2
Strait of Hormuz (SH)		3 Bandzak	M2	K1	S2	N2	O1	P1	K2	MU2	ETA2	Q1
		4 Larak	M2	K1	S2	O1	N2	P1	K2	Q1	MM	M4
		5 Bahman Port	M2	K1	S2	O1	N2	P1	J1	K2	Q1	MSF
		6 Shahid Rajaee Port	M2	S2	K1	N2	O1	P1	K2	NU2	Q1	L2
		7 Pol Port	M2	K1	S2	N2	O1	P1	K2	MK3	M4	Q1
		8 Khamir Port	M2	S2	K1	N2	O1	P1	K2	MK3	M4	MS4
Persian Gulf (PG)	North East	9 Lengeh Port	M2	K1	O1	S2	N2	P1	K2	Q1	MSF	L2
		10 Charak Port	M2	K1	O1	S2	N2	P1	MSF	NO1	Q1	K2
		11 Lavan	M2	K1	O1	S2	P1	N2	K2	MSF	Q1	NO1
		12 Taheri	M2	K1	N2	S2	O1	P1	L2	MSF	K2	MM
	North West	13 Ameri Port	M2	K1	O1	S2	P1	N2	MSF	Q1	K2	OO1
		14 Bushehr	M2	K1	O1	S2	P1	N2	K2	Q1	SSA	OO1
		15 Genaveh Port	M2	K1	O1	S2	P1	N2	NO1	MSF	K2	MK3
		16 Butaheri	M2	K1	O1	N2	S2	P1	MSF	MM	Q1	MK3
		17 Emam Khomeini Port	M2	K1	S2	N2	O1	P1	M4	K2	L2	MS4

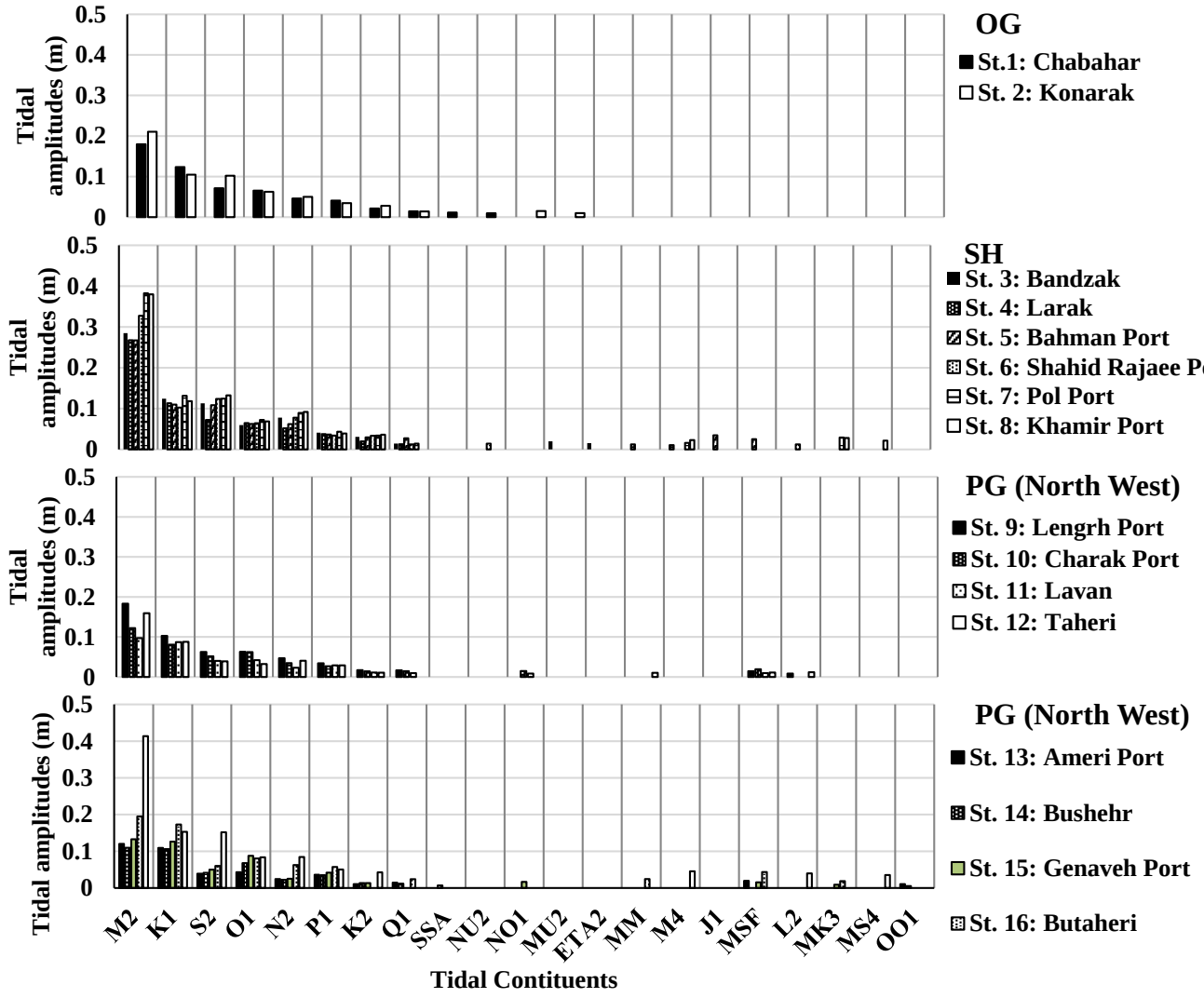

Figure 6. The amplitudes (in meters) of the first major tidal constituents achieved by the analysis of 2018 data of t-tide for all stations.

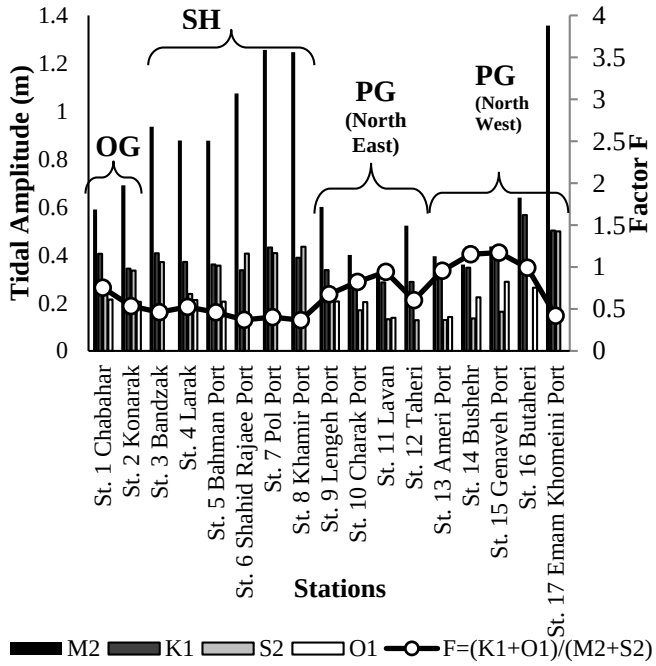

Figure 7. (Left axis:) The tidal calculated amplitudes of four major semidiurnal (M_2, S_2) and diurnal (O_1, K_1) constituents as reported by different researches [1, 21-22] by t-tide. (Right axis:) The form factor, F, (Eq. 2), calculated by M_2, S_2, O_1 and K_1 without consideration the rank of importance of that tidal constituents.

5. Conclusions

The body forces act directly on deep oceanic waters, but not directly in coastal regions. In open ocean, the tidal range is less than one meter. At the entrance opening of special points such as gently sloping surfaces, funnel-like or chimney-like surfaces is higher due to the reflection of the wave and its Refraction. The tidal range can be enhanced in funnel-like or chimney-like surfaces due to the shape of the coastline and the narrowness of the entrance opening. In this study, two areas with different appearances have been examined via tides. Persian Gulf (PG) connects Oman Gulf (OG) through the Strait of Hormuz (SH) as a narrow funnel-like shape.

Results show that the range and components of harmonic astronomical components are strongly influenced by local geography especially on SH and PG. On the head of PG, tides are strong because tides propagate into very shallow water e.g. river estuary. Tides steepen and become non-linear. Emam Khomainei Port is a good example of the shallow water condition because of the estuary of Khur-e-Mousa. Semidiurnal tides are very important components on this station.

Contrary to the studies mentioned four important tidal components are M_2, S_2, K_1 and O_1 on PG, this study clearly showed that in the stations like Bandazk, Shahid Rajaee Port, Pol Port, Khamir Port, Taheri, and Imam Khomeini Port, the N_2 component is more important than the O_1 component. Except for the M_2 component, which is the most important component of all studied area, the order of importance of other components changes on the stations. This issue is related to the geographical changes of the region in terms of appearance shape or depth. Further studies regarding the wave reflection by the coastline which is effective in increasing the range, or the rotation of the tidal waves in the mouth of the strait which increases the energy of the tidal wave, or atmospheric effects such as wind, pressure and precipitation is recommended.

List of Major Symbols

F	Form Factor
K_1	Lunar-Solar, diurnal
K_2	Lunar-Solar, semidiurnal
M_2	Main Lunar, semidiurnal
N_2	Lunar elliptic, semidiurnal
O_1	Main Lunar, diurnal
P_1	Main Solar, diurnal
S_2	Main Solar, semidiurnal

8. References

[1] Reynolds, R.M., (1993). *Physical oceanography of the Gulf, Strait of Hormuz, and the Gulf of Oman—Results from the Mt Mitchell expedition*, Marine Pollution Bulletin, Vol.27, p.35-59. DOI: 10.1016/0025-326x(93)90007-7

[2] Cartwright, D.E., and Tayler, R.J., (1971), *New computations of the tide-generating potential*, Geophysical Journal of the Royal Astronomical Society, Vol.23(1), p.45-74, DOI: 10.1111/j.1365-246X.1971.tb01803.x

[3] Darwin, G.H., (1911), *The Tides and Kindred Phenomena in the solar system*, Nature, Vol. 88(2193), p.35-36. DOI: 10.1038/088035a0

[4] Symon, K.R., (1971), *Mechanics addison-wesley*. Reading, MA, 1.

[5] Pond, S. and Pickard, G.L., (1983), *Introductory dynamic oceanography*, 2nd Edition, Pergamon Press.

[6] Hammons, T.J., (1993), Tidal power. Proceedings of the IEEE, Vol.81(3), p.419-433. DOI: 10.1109/5.241486

[7] Bryden, I.G. and Macfarlane, D.M., (2000), *The utilisation of short term energy storage with tidal current generation systems*. Energy, Vol.25(9), p.893-907. DOI: 10.1016/s0360-5442(00)00020-7

[8] Doodson, A.T., (1922), *Harmonic development of the tide-generating potential*. Proceedings of the Royal Society of London, Series A, Vol.100(704), p.305–329. DOI: 10.1098/rspa.1921.0088

[9] SHOM and UKHO, (2017), *Tidal Constituents*, Date modified May 8, 2017. Retrieved August 12, 2018, from https://www.iho.int/mtg_docs/com_wg/IHOTC/IHOTC_Misc/TWCWG_Constituent_list.pdf.

[10] Woodworth, P.L., (2010), *A survey of recent changes in the main components of the ocean tide*, Continental Shelf Research, Vol.30(15), p.1680-1691. DOI: 10.1016/j.csr.2010.07.002

[11] Müller, M., Arbic, B.K. and Mitrovica J., (2011), *Secular trends in ocean tides: observations and model results*. Journal of Geophysical Research, Vol.116(C05) p.013. DOI: 10.1029/2010jc006387

[12] Haigh, I.D., Wijeratne, E.M.S., MacPherson, L.R., Pattiaratchi, C.B., Mason, M.S., Crompton, R.P. and George S., (2014), *Estimating present day extreme water level exceedance probabilities around the coastline of Australia: tides, extra-tropical storm surges and mean sea level*, Climate Dynamics, Vol.42(1-2), p.121-138. DOI: 10.1007/s00382-012-1652-1

[13] Mawdsley, R.J., Haigh, I.D. and Wells N.C., (2015), *Global changes in tidal high water, low water and range*. Earth's Futures, Vol.3(2), p.66-81. DOI: 10.1002/2014ef000282

[14] Jay, D.A., (2009), *Evolution of tidal amplitudes in the eastern Pacific Ocean*, Geophysical Research Letters, Vol.36(4), p.L04603, DOI: 10.1029/2008gl036185

[15] Ray, R.D., (2006), *Secular changes of the M2 tide in the Gulf of Maine*, Continental Shelf Research, Vol.26(3), p.422-427, DOI: 10.1016/j.csr.2005.12.005

[16] Ray, R. D. (2009), *Secular changes in the solar semidiurnal tide of the Western North Atlantic Ocean*, Geophysical Research Letters, Vol.36(19), p.L19601, DOI: 10.1029/2009gl040217

[17] Müller, M., (2011), *Rapid change in semi-diurnal tides in the North Atlantic since 1980*. Geophysical Research Letters, 38(11), p. L11602. DOI: 10.1029/2011gl047312

[18] Feng, X., Tsimplis, M.N. and Woodworth, P.L., (2015), *Nodal variations and long-term changes in the main tides on the coasts of China*. Journal of Geophysical Research: Oceans, Vol.120(2), p.1215-1232. DOI: 10.1002/2014jc010312

[19] Feng, X., and Tsimplis, M.N., (2014), *Sea level extremes at the coasts of China*, Journal of Geophysical Research: Oceans, Vol.119(3), p.1593–1608, DOI: 10.1002/2013jc009607

[20] Rasheed, A. S., and Chua, V.P., (2014), *Secular trends in tidal parameters along the coast of Japan*. Atmosphere-Ocean, Vol.52(2), p.155-168. DOI: 10.1080/07055900.2014.886031

[21] Pous, S., Carton, X. and Lazure, P., (2012), *A Process Study of the Tidal Circulation in the Persian Gulf*, Open Journal of Marine Science, Vol.2(04), p.131-140. DOI: 10.4236/ojms.2012.24016

[22] Akbari, P., Sadrinasab, M., Chegini, V., Siadatmousavi, M., (2016), *Tidal constituents in the Persian Gulf, Gulf of Oman and Arabian Sea: a numerical study*, Indian Journal of Geo-Marine Sciences, Vol.45(8), p.1010-1016.

[23] ESRI, (2011), *ArcGIS Desktop*, 64-bit, Version 10.3, Released 2011, Redlands, CA: Environmental Systems Research Institute.

[24] Randall, J.E., (1995), *Coastal fishes of Oman*, University of Hawaii Press- Hawaii.

[25] Barth, H.J. and Khan, N.Y., (2008), *Biogeophysical setting of the Gulf*, Protecting the Gulf's marine ecosystems from pollution, p. 1-21. DOI: 10.1007/978-3-7643-7947-6_1

[26] Nadim, F., Bagtzoglou, A.C. and Iranmahboob, J., (2008), *Coastal management in the Persian Gulf region within the framework of the ROPME programme of action*. Ocean and Coastal Management, Vol.51(7), p.556-565. DOI: 10.1016/j.ocecoaman.2008.04.007

[27] Barth, H.-J. (1998). *Sebkhas als Ausdruck von Landschaftsdegradation im zentralen Küstentiefland der Ostprovinz Saudi-Arabiens*. Regensburger Geographische Schriften-Regensburg.

[28] Sugden, W., (1963), *The hydrography of the Persian Gulf and its significance in respect to evaporative deposition*. American Journal of Science, Vol.261(8), p.741–55. DOI: 10.2475/ajs.261.8.741

[29] Johns, W.E., Yao, F., Olson, D.B., Josey, S.A., Grist, J.P. and Smeed, D.A., (2003), *Observations of seasonal exchange through the Straits of Hormuz and the inferred freshwater budgets of the Persian Gulf*, Journal of Geophysical Research, Vol.108(C12), p.3391. DOI: 10.1029/2003jc001881

[30] Privett, D.W. (1959), *Monthly charts of evaporation from the North Indian Ocean, including the Red Sea and the Persian Gulf*, Quarterly Journal of the Royal Meteorological Society, Vol.85(366), p.424–428. DOI: 10.1002/qj.49708536614

[31] Hastenrath, S. and Lamb, P.J., (1979). *Climatic atlas of the Indian Ocean*, Part 2, The ocean heat budget, University of Wisconsin Press, Madison-Wisconsin.

[32] Brewer, P.G. and Dyrssen, D., (1985), *Chemical Oceanography of the Persian Gulf*, Progress in Oceanography, Vol.14, p.41–55. DOI: 10.1016/0079-6611(85)90004-7

[33] Ahmad, F. and Sultan, S.A.R., (1991), *Annual mean surface heat fluxes in the Arabian Gulf and the net heat transport through the Strait of Hormuz*, Atmosphere-Ocean, Vol.29(1), p.54–61. DOI: 10.1080/07055900.1991.9649392

[34] Soyuf Jahromi, M., (2022), *The spatial and temporal monitoring of the sea surface temperature anomaly of the Strait of Hormuz*. International Journal Of Coastal, Offshore And Environmental Engineering (ijcoe), Vol.7(4), p.1-6. DOI: 10.22034/ijcoe.2022.164980

[35] Pourkarimian, A., Soyuf Jahromi, M., and Malakooti, H. (2021). *Tracking of the oceanic water content resources of the precipitation in Dayyer Port (March 2017*). Journal of Marine Science and Technology, Vol.20(3), p.31-49. DOI: 10.22113/jmst.2019.182862.2282

[36] Pourkarimian, A., Soyuf Jahromi, M., and Malakooti, H. (2022). *Investigation and study of flood moisture transfer (Case study: March 2017 in south and southwest of Iran).* Amphibious Science and Technology, Vol.2(4), p.40-61. DOI: 10.22034/jamst.2022.543537.1050

[37] Swift, S.A. and Bower, A.S., (2003), *Formation and circulation of dense water in the Persian/Arabian Gulf*, Journal of Geophysical Research, Vol.108(C1), p.3004, DOI: 10.1029/2002jc001360

[38] Darskhan, S. and Soyuf Jahromi, M., (2022) *Numerical solution of the geostrophic mesoscale eddy in the shallow water model*, Journal of Oceanography, Vol.13(49), p.81-91, (In Persian) DOI: 10.52547/joc.13.49.81

[39] Ramak, H., Soyuf Jahromi, M. and Akbari, P., (2021), *Using surface temperature data of the Oman Sea to identify subsurface water of the Persian Gulf*, Hydrophysics, Vol.7(2), p.79-93. (In Persian)

[40] Ramak, H., Soyuf Jahromi, M. and Akbari, P., (2022a), *Persian Gulf Water mass tracking by surface temperature and salinity properties*, Journal of Oceanography, Vol.12(48), p.13-28. (In Persian) DOI: 10.52547/joc.12.48.13

[41] Ramak, H., Soyuf Jahromi, M. and Akbari, P., (2022b), *Persian Gulf Water mass tracking by surface temperature and salinity properties*, Journal of Oceanography, Vol.12(48), p.13-28. (In Persian) DOI: 10.52547/joc.12.48.13

[42] Ramak, H., Soyuf Jahromi, M. and Akbari, P., (2023a) *Investigating the downwelling of Persian Gulf Water in the Gulf of Oman*. International Journal Of Coastal, Offshore And Environmental Engineering (ijcoe), Vol.8(1), p.1-9. DOI: 10.22034/ijcoe.2023.166317

[43] Ramak, H., Soyuf Jahromi, M. and Akbari, P., (2023b), *Investigation of salinity and temperature of Persian Gulf water by FVCOM Model*. Journal of Oceanography, Vol.13 (52), p.106-120, (In Persian) DOI: 10.52547/joc.13.52.8

[44] Lashkari, S., Soyuf Jahromi, M., and Hamzei, S., (2023), *Seasonal changes of the Persian Gulf water mass in the Gulf of Oman*. Journal of Oceanography,

14 (53) :103-122, (In Persian) DOI: 10.52547/joc.14.53.9

[45] ROPME, 2004. *State of the Marine Environment Report, 003*. The Regional Organization for the Protection of the Marine Environment (ROPME)-Kuwait, p.217.

[46] Soyuf Jahromi, M., Sadrinasab, M. Aliakbari Bidokhti, A.A., (2014), *3D simulation of measured Oman data at late winter, 2005*. Journal of Marine Science and Technology, Vol.13(3), p.21-31. (In Persian), DOI: 10.22113/jmst.2014.7821

[47] Lashkari, S., Soyuf Jahromi, M., and Hamzei, S., (2022), *The temperature changes of WOA data in upper layers of Gulf of Oman*. 1st international marine science conference with the approach of innovation in aquatic ecosystems based on sea-based economy, p.383-395. (In Persian)

[48] Al-Majed, N. and Preston, M., (2000), *An assessment of the total and methyl mercury content of zooplankton and fish species tissue collected from Kuwait territorial waters*. Marine Pollution Bulletin, Vol.40(4), p.298–307. DOI: 10.1016/s0025-326x(99)00217-9

[49] Mohammadpoor, F., Soyuf Jahromi, M., and Hamzei, S., (2022), *Comparison of the vertical temperature distribution on the east of the strait of Hormuz*. 1st international marine science conference with the approach of innovation in aquatic ecosystems based on sea-based economy, p.176-188. (In Persian)

[50] Mohammadpour, F., Soyuf Jahromi, M. and Hamzei, S., (2023), *Winter study of the stability and Double diffusion convection in the east of the Strait of Hormuz*, Hydrophysics, Vol.8(2), p.79-93. (In Persian)

[51] Defant A., (1960), *Physical Oceanography*, (Pergamon Press LTD) Vol. 2, p. 571.

[52] Hunter, J.R., (1982), *The physical oceanography of the Arabian Gulf: a review and theoretical interpretation of previous observations*. 1st Arabian Gulf conference on marine environment and pollution. Kuwait University, Faculty of Science, Kuwait, p. 1-23.

[53] Soyuf Jahromi, M. and Emami, M., (2021), *The role of different positions of tidal turbines for energy extraction in Qeshm channel*. International Journal Of Coastal, Offshore And Environmental Engineering(ijcoe), Vol.6(5), p.1-9. DOI: 10.22034/ijcoe.2021.152602.

[54] Lehr, W.J., (1984), *A brief survey of oceanographic modelling and oil spill studies in the KAP region*. NESCO Reports in Marine Science, Vol.28, p.4–11.

[55] Najafi, H.S. (1979), *Modelling tides in the Persian Gulf using dynamic nesting*, PhD thesis, University of Adelaide, Adelaide, South Australia.

[56] Lardner, R.W., Belen, M.S. and Cekirge. H.M., (1982), *Finite difference model for tidal flows in the Arabian Gulf*. Computers & Mathematics with Applications, Vol.8(6), p.425–444. DOI: 10.1016/0898-1221(82)90018-9

[57] Teubner, M.D., Najafi, H.S., Noye, B.J. and Rasser, P.E., (1999), *Modelling tides in the Persian Gulf using dynamic nesting*, Modelling Coastal Sea Processes, p.57-80. DOI: 10.1142/9789814350730_0003

[58] http://iranhydrography.ncc.org.ir

[59] Bowen, A.J., (1972), *The tidal regime of the River Thames; long-term trends and their possible causes*, Philosophical Transactions of the Royal Society of London, Series A: Mathematical, Physical and Engineering Sciences, Vol.272(1221), p.187-199. DOI: 10.1098/rsta.1972.0045

[60] Amin, M., (1983), *On perturbations of harmonic constants in the Thames Estuary*. Geophysical Journal International, Vol.73(3), p.587-603. DOI: 10.1111/j.1365-246x.1983.tb03334.x

[61] Jay, D.A., Leffler, K. and Degens, S., (2011), *Long-term evolution of Columbia River tides*, Journal of Waterway, Port, Coastal, and Ocean Engineering, Vol.137(4), p.182-191. DOI: 10.1061/(asce)ww.1943-5460.0000082

[62] Vellinga, N.E., Hoitink, A.J.F., van der Vegt, M., Zhang, W. and Hoekstra, P., (2014), *Human impacts on tides overwhelm the effect of sea level rise on extreme water levels in the Rhine–Meuse delta*, Coastal Engineering, Vol.90, p.40–50. DOI: 10.1016/j.coastaleng.2014.04.005

[63] Chernetsky, A.S., Schuttelaars, H.M. and Talke, S.A., (2010), *The effect of tidal asymmetry and temporal settling lag on sediment trapping in tidal estuaries*. Ocean Dynamics, Vol.60(5), p.1219-1241. DOI: 10.1007/s10236-010-0329-8

[64] Familkhalili, R. and Talke S.A., (2016), *The Effect of Channel Deepening on Storm Surge: Case Study of Wilmington, NC*, Geophysical Research Letters, Vol.43(17), p.9138-9147. DOI: 10.1002/2016gl069494

[65] Colossi, J.A. and Munk, W., (2006), *Tales of the Venerable Honolulu Tide Gauge*, Journal of Physical Oceanography, Vol.36(6), p.967–996, DOI: 10.1175/jpo2876.1

[66] Müller, M., Cherniawsky, J.Y., Foreman, M.G.G. and Storch J.S. (2012), *Global M2 internal tide and its seasonal variability from high resolution ocean circulation and tide modeling*. Geophysical Research Letters, Vol.39(19), p.L19607. DOI: 10.1029/2012gl053320

[67] Forrester, W.D., (1983), Tidal analysis and prediction, In: Canadian tidal manual. Ottawa, Ont. Department of Fisheries and Oceans, Canada, p.39-54.

[68] Pawlowicz, R., (2002), *Observations and linear analysis of sill-generated internal tides and estuarine flow in Haro Strait*, Journal of Geophysical Research: Oceans, Vol.107(C6), p.9-1. DOI: 10.1029/2000jc000504

[69] Pawlowicz, R., Beardsley, B. and Lentz, S., (2002), *Classical tidal harmonic analysis including error estimates in MATLAB using T_TIDE*. Computers and Geosciences, Vol.28(8), p.929-937. DOI: 10.1016/s0098-3004(02)00013-4

[70] http://www.eos.ubc.ca/~rich/t_tide/t_tide_v1.3beta.zip

[71] Desyari, M., (2019), *Analisis Karakteristik Pasang Surut Perairan Dermaga Tempat Pelelangan Ikan (TPI) Palopo Sulawesi Selatan dengan Menggunakan Metode Admiralty, T-Tide, TMD, dan NAOTide*, PhD thesis, Universitas Brawijaya-Brawijaya.

[72] Hennon, T.D., Alford, M.H. and Zhao, Z., (2019), *Global assessment of semidiurnal internal tide aliasing in Argo profiles*. Journal of Physical Oceanography, Vol.49(10), p.2523-2533. DOI: 10.1175/jpo-d-19-0121.1.

[73] Suharyo, O. S., Setiadi, J., Sukoco, N. B., & Kuncoro, K. (2020). *The analysis formulation of the Lowest Astronomical Tide (LAT) based on the time observation (The case study of Benoa Waters)*. Journal ASRO, Vol.11(1), p.77-87. DOI: 10.37875/asro.v11i1.205

[74] Marques, O.B., Alford, M.H., Pinkel, R., MacKinnon, J.A., Klymak, J.M., Nash, J.D., Waterhouse, A.F., Kelly S.M., Simmons, H.L. and Braznikov, D., (2021), *Internal tide structure and temporal variability on the reflective continental slope of Southeastern Tasmania*. Journal of Physical Oceanography, Vol.51(2), p.611-631. DOI: 10.1175/jpo-d-20-0044.1

[75] Wan, Y., (2023), *Harmonic analysis in tide analysis*. 2nd International Conference on Statistics, Applied Mathematics, and Computing Science (CSAMCS 2022), Vol.12597, p.768-774.

[76] The MathWorks Inc. (2016), *MATLAB and Statistics Toolbox 64-bit*, Version 2016a, Release 2016a, Natick, Massachusetts, USA.

[77] Foremann, M., (1977). *Manual for tidal heights analysis and prediction*, Pacific marine science report, Vol.10, p.66-77.

[78] Stal, C., Poppe, H., Vandenbulcke, A. and De Wulf, A., (2016), *Study of post-processed GNSS measurements for tidal analysis in the Belgian North Sea*. Ocean Engineering, Vol.118, p.165-172. DOI: 10.1016/j.oceaneng.2016.04.014

[79] Lin, H., Hu, J., Zhu, J., Cheng, P., Chen, Z., Sun, Z., and Chen, D., (2017), *Tide-and wind-driven variability of water level in Sansha Bay, Fujian, China*. Frontiers of Earth Science, Vol.11(2), p.332-346. DOI: 10.1007/s11707-016-0588-x

[80] Soyuf Jahromi, M. and Shahmansoori, Z. (2021), *The monthly sea-level anomaly patterns on the Persian Gulf*. Iranian journal of Marine technology, Vol.7(4), p.97-106. (In Persian)

[81] Soyuf Jahromi, M. and Shahmansoori, Z. (2022), The seasonal changes of sea-level anomalies on the Persian Gulf (1993-2017). Journal of Marine Science and Technology, Vol.*21*(1), p.1-15. (In Persian) DOI: 10.22113/jmst.2021.197166.2303

[82] Lisitzin, E., (1974), *Sea-level changes*: Elsevier Oceanography Series (Vol. 8).

[83] Pugh, D., (1987), *Tides, Surges and Mean Sea Level: A Handbook for Engineers and Scientists*. John Wiley & Sons, Chichester.

[84] Pugh, D., (2004), *Changing Sea Levels-Effects of Tides, Weather and Climate*. Cambridge University Press, Cambridge.

[85] Yeknami, S.R., Soltanpour, M., and Ranji, Z. (2016). *Analysis of nearshore local effects on tidal behaviour at imam Khomeini port and Musa bay*. Coastal Engineering Proceedings, Vol.(35), p.7-7. DOI: 10.9753/icce.v35.currents.7

[86] Emami, M., Soyuf Jahromi, M. and Behmanzadegan, A., (2019), *Coastline Effect on Tidal Flow Pattern*. Journal of Marine Science and Technology, Vol.18(2), p.12-25. (In Persian), DOI:0.22113/jmst.2019.122581.2137

INTERNATIONAL JOURNAL OF
COASTAL, OFFSHORE & ENVIRONMENTAL ENGINEERING IJCOE Vol.8/No. 4/Autumn 2023 (49-58)

Available online at: www. Ijcoe.org

Underwater Image Enhancement Using FPGA-Based Gaussian Filters with Approximation Techniques

Mehrnaz Monajati[1]

[1] *Assistant professor, Graduate University of Advanced Technology, Kerman; m.monajati@kgut.ac.ir*

ARTICLE INFO

Article History:
Received: 02 Jan 2022
Accepted: 05 Oct. 2022

Keywords:
Underwater image
Gaussian filter
Low power
High speed
FPGA

ABSTRACT

The major challenge in marine environment imaging lies in addressing the haziness induced by natural phenomena, such as absorption and scattering in underwater scenes. This haze significantly impacts the visual quality of underwater images, necessitating improvement. This paper presents a novel approach aimed at enhancing the efficiency of Gaussian filters for reducing Gaussian noise in underwater images. The method introduces a pipeline structure in the Gaussian filter implementation and evaluates the influence of employing approximate adders on overall performance. Simulation results reveal a notable speed enhancement exceeding 150%, coupled with a substantial reduction in power consumption exceeding 34%. However, these advantages are tempered by an increase in spatial requirements. The study recognizes the inherent tradeoff between output quality and power, highlighting the applicability of the proposed design in error-resilient applications, particularly in image and video processing domains. In essence, the presented approach offers a compelling solution where the benefits of accelerated speed and reduced power consumption outweigh spatial constraints, contributing to the advancement of underwater image enhancement techniques.

1. Introduction

Underwater imaging instruments are essential for remote sensing due to Earth's significant water coverage. Optical sensors capture acoustic signals, but resulting images suffer from issues like limited light range, lighting disruptions, low contrast, and color degradation. These disturbances necessitate pre-processing before crucial image processing tasks. Edge-preserving filters help denoise images without compromising quality or edges. Pre-processing involves correcting illumination, suppressing noise, enhancing contrast, and adjusting colors. Underwater images require pre-processing due to degradation caused by light transmission properties, environmental factors, and video capture challenges. Identifying suitable filters for effective pre-processing is a key focus in addressing these issues.

Exploring the underwater environment through video and images is a complex and fascinating endeavor, marked by challenges such as noise, limited visibility, light scattering, attenuation issues, non-uniform lighting, and other inherent factors of seawater [1, 2]. The use of artificial light sources exacerbates problems, introducing issues like image blur, haziness, and the presence of bluish or greenish hues in underwater images. This leads to absorption, scattering, color distortion, and noise [3]. These challenges pose a significant hurdle for researchers seeking to harness computer technology for in-depth studies, especially in the classification, recognition, and segmentation of coral reef components and various fish species.

Understanding underwater ecology is crucial for effective marine resource management and monitoring. Consequently, image analysis techniques rooted in computer vision and image processing technologies have been developed to facilitate proper monitoring of marine resources. Despite these advancements, there has been no comprehensive quantitative or qualitative assessment of all underwater marine resources, as noted in [4, 5].

Underwater images often exhibit poor visibility, a foggy appearance, and misty issues, with blurring occurring due to wave surfaces during object acquisition. Additionally, these images are prone to unwanted noise and increased scattering effects. Distortions vary across images acquired at different

times. Researchers globally are exploring a range of techniques, from simple approaches to multilayered deep techniques, to mitigate distortion effects on underwater images. The ideal technique should strike a balance between effectiveness and complexity.

The PCA fusion-based method integrates homomorphic filters, adaptive histogram equalization, and median filters for individual color channels. This technique is applied to fuse two images, enhancing color contrast and resulting in improved qualitative outcomes [6]. CLAHE proves effective in enhancing the visual quality of underwater images by addressing issues such as uneven illumination. It achieves adaptability through the application of adaptive histogram equalization and introduces a weighted map to enhance the visibility of distant objects [7]. The combination method involves integrating CLAHE and dark channel prior for image enhancement. This approach includes identifying the presence of artificial light, removing it if detected, and subsequently applying CLAHE to improve the overall quality of underwater images [8].

Histogram equalization image enhancement method was introduced to advance CLAHE, involving the conversion of RGB input images to the HSV color space. Individual components (Hue, Saturation, and Value) underwent histogram equalization, leading to improved visual quality in the output image compared to the input [9]. Additionally, a method named mixture contrast limited adaptive histogram equalization was developed, where the RGB input image was transformed into the HSV color space [10]. Both CLAHE-RGB and CLAHE-HSV images were generated and combined using Euclidean norm, contributing to enhanced underwater image quality.

In addressing the challenge of edge identification in acoustic underwater images, the study detailed in [11] enhanced these images by utilizing Wiener filtering to reduce speckle noise while preserving high-frequency components. Furthermore, a median filter was applied to eliminate small objects. Performance evaluation included the extraction of local minimum and maximum values through morphological operations. The resulting edge maps, when compared with Canny and Sobel algorithms, demonstrated superior performance over conventional methods, although some noise contamination persisted.

In [12], an approach to identify edges in underwater images was proposed, utilizing fractional order differentiation. The study introduced a texture enhancement filter based on the Grünwald-Letnikov (G-L) fractional differential operator. An analysis was conducted on diverse underwater images using both conventional and fractional differential operators, with results compared to the Riemann-Liouville fractional differential operator technique (R-L). The suggested method demonstrated superior performance compared to traditional and R-L-based approaches, particularly in recognizing edges in low-contrast underwater images. It offered heightened accuracy, improved brightness, and increased information extraction.

In [13], the enhancement of underwater image quality was pursued through the application of edge detection methods and the utilization of the Lab color model. The authors executed edge detection subsequent to color correction and contrast enhancement. Faced with challenges such as light illumination, water velocity, and suspended particles, the preference was given to color detection instead of direct edge recognition, aiming for improved results in underwater image processing. Although their approach successfully identified object shapes, some residual noise remained. To enhance future edge detection outcomes, the authors conveyed their intention to incorporate deep networks for automated operations.

Numerous underwater image enhancement algorithms have been proposed, leveraging texture and color features for feature database creation and improved image attribute description [14-16]. While histogram equalization is a common method for visual cue equalization, its simplicity often results in less appealing enhanced images. Model-based algorithms introduce some complexity, and recent deep neural network-based methods, although offering better quality, demand significant computational resources. The challenge lies in striking a balance between image quality and computational complexity. In this context, we propose an approximate pipeline Gaussian filter for enhanced underwater image improvement, aiming for an optimal trade-off.

2. Hardware Platforms for Image Processing

Multiple hardware platforms are accessible for deploying vision algorithms, including general-purpose computers, digital signal processors (DSPs), graphical processing units (GPUs), and reconfigurable devices like field-programmable gate arrays (FPGAs). In the field of image processing, FPGAs exhibit superior performance in complex computations, while GPUs excel in simpler tasks. Modern FPGAs empower system designers to create high-performance computing applications with significant parallelism [17].

Recent advances in computer vision, particularly in object detection, motion tracking, and semantic segmentation, have heightened interest in digital image processing (DIP) techniques. To address the need for rapid prototyping, low power consumption, and low latency, hardware accelerators, such as custom processors and co-processors, offer an alternative to software implementations. Meeting the demands of real-time image processing requires more processing power than conventional processors can provide. FPGA implementations outperform DSPs

and GPPs for algorithms leveraging substantial parallelism [18, 19]. Traditional DSP arrays, with fixed architectures and relatively short lifespans, can be expensive to program line by line with thousands of lines of code [20]. The memory bandwidth of contemporary FPGAs far exceeds that of GPPs or DSPs, running at two to ten times the speed of the FPGA [21]. Beyond their capability for highly parallel arithmetic architecture, FPGAs are well-suited for tasks such as digital filtering, Fast Fourier Transform, and image processing. FPGAs are a common choice for rapid prototyping, provide a favorable trade-off among design metrics, ensuring a swift time-to-market compared to other integrated circuit (IC) technologies [22]. FPGAs also find applications in control and communication [23]. Developing hardware accelerators in FPGA involves exploring various architectures, considering aspects such as the arithmetic used [24, 25], approximate computing techniques [26], and hardware/software communication architecture [27]. Features and techniques like these play a crucial role in implementing digital image processing algorithms on hardware. In this context, assessing potential implementation models and comparing their impact on system metrics is essential. Such evaluations assist hardware designers in making informed decisions about their designs. In [28], the mix module implementation of underwater image enhancement on FPGA relies on fusion by wavelet decomposition. This method significantly improves the visibility of underwater images, and qualitative results illustrate the enhanced quality of hazy underwater images.

In [29], the focus is on optimizing the preprocessing of optical images from autonomous underwater vehicles in challenging conditions. It highlights the efficiency of FPGAs for correcting image degradation through non-linear filtering, implementing two-dimensional FFT, its inverse, and logarithmic computation. Demonstrating FPGA effectiveness in parallel architectures, the study improves histograms in underwater image preprocessing via frequency-based filtering and introduces a method applicable in digital signal processing tasks.

In [30], a benchmarking analysis compared three Retinex model-based algorithms (SSR, MSR, MSRCR) on five embedded systems—Beagle Board, Odroid-XU4, Raspberry Pi 4, Jetson Nano, and Jetson TX2—for enhancing underwater images. Quality metrics (UIQM, UCIQUE, BRISQUE, Entropy) without a reference image were utilized. MSRCR performed best on Jetson TX2, with a 0.46s processing time difference compared to a high-performance PC. Implementing these algorithms on embedded systems proved cost-effective and held promise for artificial vision-equipped underwater vehicles.

[31] presented a low-cost, high-throughput design of the retinex video enhancement algorithm, renowned for restoring naturalness, especially in dark areas. Historically burdened by computational complexity, the hardware (HW) design was implemented on a field-programmable gate array (FPGA), achieving a throughput of 60 frames/s for a 1920×1080 image with minimal latency. The design optimized HW resources by utilizing a small line buffer, applying approximate computing for the Gaussian filter, and introducing a novel exponentiation operation. This approach significantly reduced HW resources (up to 79.22% of total resources) compared to existing systems while ensuring compatibility with commercial devices through standard HDMI/DVI video ports.

3. Approximate Computing

In error-resilient applications like multimedia, data mining, image processing, and machine learning, exact precision is not always essential [32]. Acceptable results with some accuracy degradation suffice for these applications. This flexibility enables trade-offs between accuracy and electrical performance, allowing for gains in power dissipation, occupied area, and delay by sacrificing a degree of accuracy [33].

Voltage over-scaling is a solution to reduce circuit power dissipation [34]. However, operating a circuit under normal voltage levels may lead to timing-induced failures, causing significant errors in the most significant bits. Approximate computing is an efficient paradigm to lower power consumption and enhance embedded system performance. Allowing errors at the outputs of a complex circuit simplifies logic expressions, reducing logic counts. This approach results in savings in areas, dynamic power dissipation, and shortened circuit delays [35].

In image and video processing, where error tolerance is permissible, adopting approximate computing techniques offers significant improvements in speed and power efficiency, albeit with a trade-off in output quality. The diverse accuracy requirements of various applications, coupled with the dynamic nature of accuracy needs within the same application at different processing stages or over time, underscore the flexibility and adaptability of approximate computing in meeting specific computational demands [36].

4. Gaussian Filter

In image processing, noise filtering is a crucial element designed to eliminate noise and its effects from the original image while striving to minimize distortion. However, these filtering operations typically involve intensive arithmetic operations, contributing to increased energy consumption in the

system. The Gaussian filter (GF) is a convolution operator employed for image blurring and noise removal [37]. The Gaussian filter, crucial for image smoothing, is a fundamental component in the initial stages of noise-sensitive edge detection algorithms like Canny, Sobel, and Laplace. Its primary role is to reduce distortions, ensuring the optimal performance of these algorithms.

Smoothing filters act as low-pass filters by suppressing the high-frequency components of an image. These components include characteristics like object contours, where the frequency increases with the abruptness of contour direction changes [37]. Consequently, smoothing filters work to alleviate these transitions, making them useful for tasks such as reconstructing incomplete contours caused by distortions from low resolution.

Eq.(1) represents a two-dimensional Gaussian function frequently employed in image and signal processing.

$$f(x.y) = \frac{1}{2\pi\sigma^2} e^{\left(-\frac{x^2+y^2}{2\sigma^2}\right)} \quad (1)$$

The equation f(x,y) denotes the value of the Gaussian function at the coordinates (x,y). σ is the standard deviation parameter, influencing the width or spread of the Gaussian function. The standard deviation (σ) controls the width of the bell-shaped curve generated by the Gaussian function. Larger values of σ result in a broader curve. This Gaussian function is commonly applied in image processing for blurring and smoothing, emphasizing central values while suppressing those farther from the center

The Gaussian filter possesses the valuable property of separability. This means that filters with a size of n×n can be split into two masks with sizes n×1 and 1×n. This separation enables the convolution to be performed in two operations, promoting temporal parallelism by initiating the second operation before the completion of the first.

4. Proposed Architecture

To develop an efficient image processing algorithm for FPGA stream-based processing, a typical architecture combines row buffers (line buffers) capable of storing one image row and window buffers, 2D arrays storing a local image area required for computing the current output pixel. This setup enables sequential reading of input image/video pixels, optimizing the use of the FPGA's limited memory. Only the minimum pixels necessary for computing the current pixel's filtered value are stored at any given time. The required number of line buffers is estimated as H - 1, with H representing the vertical size of the kernel. The window buffer matches the kernel size (e.g., a 3×3 window buffer for a Gaussian filter with a 3×3 kernel). The overall architecture is illustrated in Figure 1.

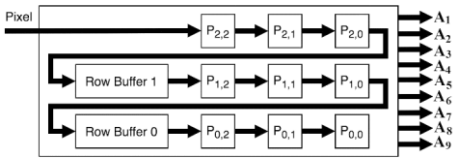

Figure 1. Delay line buffer structure

The delay line buffer optimizes memory access during convolution by storing recently accessed pixel values. In a typical digital image setup, pixels are stored sequentially in a frame buffer. The delay line buffer, using shift registers, retains the last values read, focusing on local storage for pixels still in use within upcoming convolution windows. This approach minimizes the need for continuous memory access. The structure involves nine 1-pixel registers for the current window and two row buffers storing additional pixels from the first two rows in the sliding window. The window buffer must match the size of the kernel.

To observe the filter's impact on the image, the mask must traverse all pixels, determining the brightness intensity of each new pixel based on Eq. (2) as illustrated in Figure 2.

$$h[i.j] = AP_1 + BP_2 + CP_3 + DP_4 + EP_5 + FP_{62} + GP_7 + HP_8 + IP_9 \quad (2)$$

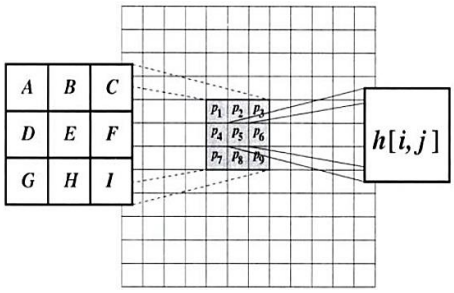

Figure 2. Convolution Operation on an image with a 3x3 kernel

4.1 Pipeline Gaussian Filter (PGF)

In this study, Figure 3 displays the Gaussian filter kernel, while Figure 4 presents the block diagram of the Gaussian filter implementation. The multiplication by 2 and 4 is achieved through left-shifting the pixel value by 1 and 2 bits, respectively. Similarly, division by 16 is performed by right-shifting the desired number by 4 bits. The Gaussian filter architecture consists of eight adders and six shifters for multiplication operations. However, the critical path from input to output includes fout adders and two shifters, leading to a slower calculation speed.

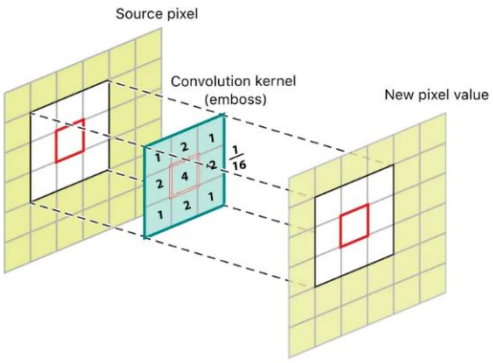

Figure 3. Application of the weighted kernel corresponding to the standard 3×3 Gaussian filter on the image

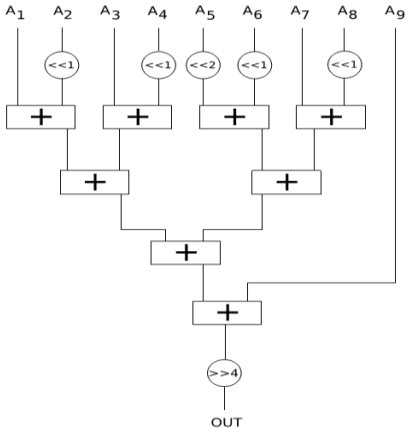

Figure 4. Block diagram of gaussian filter

A pipeline structure enhances processing speed by dividing the computation task into stages, allowing simultaneous execution of different stages. Each stage of the pipeline handles a specific aspect of the computation. As one stage completes its task, the results are seamlessly transferred to the next stage, enabling continuous processing. This concurrent operation minimizes idle time and optimizes resource utilization.

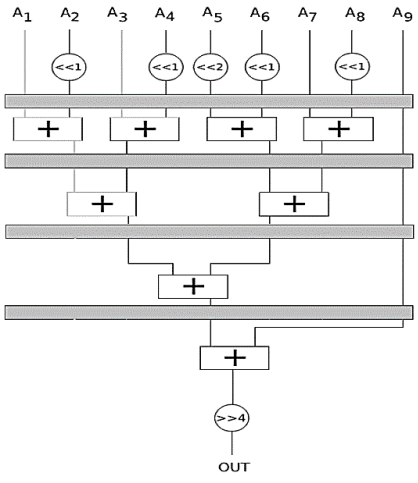

Figure 5. Pipeline Gaussian filter

To improve the speed of the Gaussian filter, a pipeline structure with four stages is implemented, as illustrated in Figure 5. This design approach ensures seamless computation, with each stage playing a role in enhancing the overall processing speed.

4.3 Approximate Adders

To implement various types of approximate Gaussian filters, we employed different approximate adders. Reducing the logic complexity of adders at the bit level offers enhanced power savings compared to conventional low-power design methods. The reduction in logic complexity for a conventional full adder (FA) cell was attained by minimizing the number of transistors. Several simplified versions of the FA were tested based on this logic complexity reduction.

The approximate full adders (APFAs) employed in the design of the Gaussian filter exhibit distinct characteristics. We employ some approximate adders in [38]. APFA1 approximates both Sum and Cout, with Sum being precise for 6 out of 8 cases and Cout for 7 out of 8 cases, excluding specific input combinations. In contrast, APFA2 focuses on approximating Sum alone, ensuring precision for 6 out of 8 cases and Cout for all cases. APFA3 involves approximation in both Sum and Cout, with Sum being precise for 5 out of 8 cases and Cout for 7 out of 8 cases. APFA4 approximates Sum and Cout, achieving precision in Sum for 5 out of 8 cases and Cout for 6 out of 8 cases at the logic level. APFA5 approximates both Sum and Cout, achieving precision in Sum for 4 out of 8 cases and Cout for 6 out of 8 cases, excluding specific input combinations. Meanwhile, APFA6 approximates both Sum and Cout, with Sum being correct for 5 out of 8 cases and Cout for 6 out of 8 cases. APFA7 demonstrates that Sum is correct for 6 out of 8 cases, and Cout is correct for all 8 cases, indicating a lower probability of error compared to APFA6. APFA8 introduces three errors in Sum, with Sum being correct for 5 out of 8 cases. APFA9 shows Sum is correct for 7 out of 8 cases. Lastly, APFA10 introduces three errors in Sum, with Sum being correct for 5 out of 8 cases, and Cout is correct for all 8 cases in APFA10. Table 1 displays the logic equations for different approximation methods. "None" indicates a precise full adder with no approximation applied.

Approximations are introduced to 16-bit adders through a carry ripple structure (Figure 1), specifically focusing on the least significant bits in each FA block. Evaluation reveals that acceptable output quality is sustained up to an 8-bit approximation, with a decline in quality beyond this threshold.

Table 1. Logical functions of approximate full adders

16-Bit FA	Logic function Sum	C_{out}
FA	$A'B'C_{in} + ABC_{in} + AB'C'_{in} + A'BC'_{in}$	$AB + BC_{in} + AC_{in}$
APFA1	$ABC_{in} + C'_{out}C_{in}$	$AC_{in} + B$
APFA2	C'_{out}	$AB + BC_{in} + AC_{in}$
APFA3	C'_{out}	$AC_{in} + B$
APFA4	$ABC_{in} + C'_{out}C_{in}$	A
APFA5	B	A
APFA6	$A' + BC_{in}$	A
APFA7	$A'(B + C_{in}) + BC_{in}$	$AB + BC_{in} + AC_{in}$
APFA8	$(A' + B)C_{in}$	$AB + BC_{in} + AC_{in}$
APFA9	$B'C'_{in} + ABC + A'C'_{in} + A'B'$	$AB + BC_{in} + AC_{in}$
APFA10	$A' + BC_{in}$	$AB + BC_{in} + AC_{in}$

The simulation results in Section 5 illustrate the impact of varying the number of least significant bits (LPL) on which the approximation is applied, shedding light on its influence on the output quality.

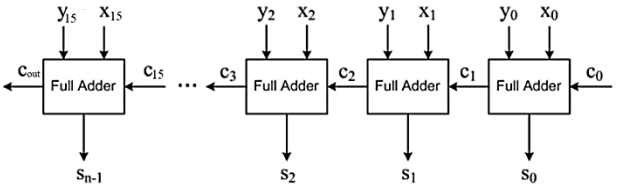

Figure 6. 16-bit carry ripple adder

5. Simulation Results

To evaluate the effect of utilizing an approximate adder on the output image quality, a 16-bit model of the Gaussian filter is designed in the MATLAB environment. Gaussian noise is then introduced to the original image, serving as input for both the exact Gaussian filter and the approximate Gaussian filters.

In the context of image quality assessment, several metrics are commonly employed to quantitatively evaluate the performance of image processing algorithms. The Peak Signal-to-Noise Ratio (PSNR) measures the ratio between the maximum possible power of a signal and the power of corrupting noise, providing insight into the fidelity of the reconstructed image. PSNR is calculated form Eq.(3). Mean Square Error (MSE) quantifies the average squared difference between corresponding pixel values in the original and reconstructed images, offering a measure of the overall image distortion. It is described in Eq.(4). Structural Similarity Index (SSIM) , which is computed using Eq.(5) , evaluates the similarity between two images, considering luminance, contrast, and structure, and providing a comprehensive measure of perceptual quality [39]. μ and σ denote the mean and variance of the image intensities respectively. C_1 and C_2 are constants. ω is Gaussian weighting function that is normalized to unit sum ($\sum_{i=1}^{N} \omega_i = 1$).

Error Distance (ED), Mean Error Distance (MED), and Normalized Error Distance (NED) gauge the spatial discrepancies between corresponding pixels in the original and reconstructed images, offering insights into the accuracy of the reconstructed image at both individual and average levels [40]. the Error Distance (ED) between two points ($x_{original}$, $y_{original}$) and ($x_{reconstructed}$, $y_{reconstructed}$) in an image can also be expressed using the Euclidean distance formula in the Eq.(6). NED is calculated by dividing the Euclidean distance by the diagonal length of the image. MED provides a measure of the average error distance between corresponding points in the original and reconstructed images. These metrics collectively contribute to a comprehensive evaluation of the performance of image processing algorithms.

$$PSNR(f.g) = 20\,log_{10}\left(\frac{2^B-1}{MSE(f.g)}\right) \quad (3)$$

$$MSE(f.g) = \frac{1}{MN}\sum_{i=1}^{M}\sum_{j=1}^{N}\left(f_{ij} - g_{ij}\right)^2 \quad (4)$$

$$SSIM(f.g) = \frac{(2\mu_f\mu_g + C_1)(2\sigma_{fg} + C_2)}{\left(\mu_{f+}^2\mu_{f+}^2 + C_2\right)\left(\sigma_{f+}^2\sigma_{f+}^2 + C_2\right)} \quad (5)$$

$$ED = \sqrt{f^2 - g^2} \quad (6)$$

$$MED = \frac{\sum_{i=1}^{N} ED_i}{N} \quad (7)$$

Where, N represents the total number of pixels in the image, and i denotes the pixel index. The formulas provide quantitative measures for assessing the quality and accuracy of reconstructed images.

We selected two real-world underwater images [41] to simulate genuine underwater conditions. Gaussian noise was introduced to these images. The addition of noise was accomplished using the 'imnoise' function in MATLAB, incorporating a Gaussian distribution with a mean (m) of 0.0005 and a variance (v) of 0.005.

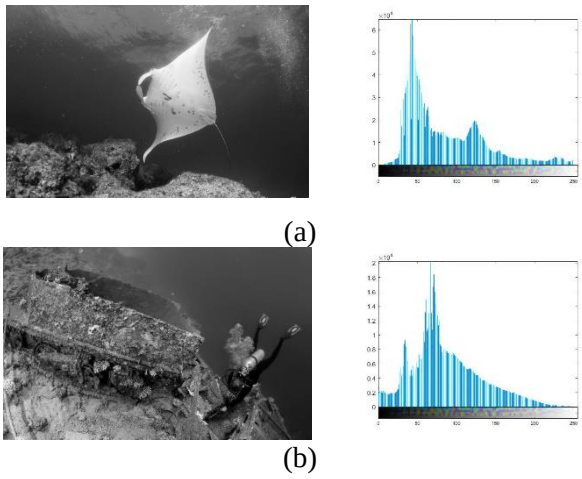

(a)

(b)

Figure 7. Two raw underwater images taken in diverse underwater scenes and their histograms. (a) flatfish, (b) diver [41]

Referring to Figure 8, it is evident that approximate adders up to 5 bits contribute to satisfactory image quality in the Gaussian filter output. However, an additional increase in the LPL causes a sudden decline in output quality, rendering the approximation ineffective. Significantly, the utilization of APFA9

and APFA2 results in the highest output quality, while employing APFA1 leads to the lowest. This observation underscores the critical role of both the approximation method and LPL in determining the balance between approximation and output quality in the Gaussian filter.

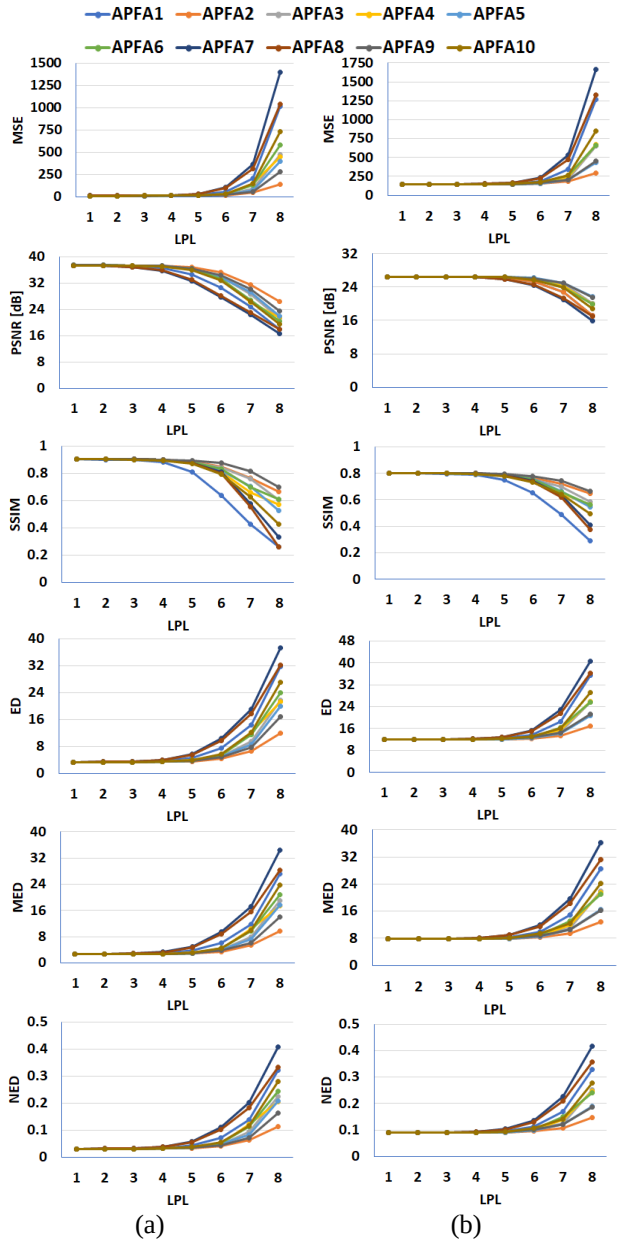

Figure 8. Evaluation Metrics for Image Enhancement of (a) flatfish and (b) diver

Approximate pipeline Gaussian filters (APGF) demonstrate effective performance up to a 5-bit approximation for both images, with the diver image showing satisfactory results up to 6 bits. The success is attributed to the Gaussian filter's role in smoothing and reducing image noise, especially in cases with a wide dynamic range of pixel intensities. When the histogram is concentrated within a narrow intensity range, the filter's impact may be more subtle due to fewer high-frequency components to smooth. Beyond smoothing, the Gaussian filter influences image contrast based on pixel intensity distribution in the histogram. In instances of low contrast, where pixels concentrate around a specific intensity, the filter enhances contrast by smoothing intensity transitions, contributing to overall image quality improvement.

6. Synthesis Results

To assess the physical characteristics of our approximate Gaussian filters, we developed a parameterizable and synthesizable Verilog HDL model for each architecture dedicated to the Gaussian filter. These models underwent validation through simulations using the ModelSim simulator and physical prototyping on the MAX10 device from Intel® FPGA using Quartus. Power consumption was estimated using the Power Analysis tool with a VCD file generated in post-synthesis simulation with 100,000 random inputs. Line buffers, essential for window-based spatial filters (see Figure 1) are excluded from synthesis results as their size depends on the input image size.

As per Table 2, the implementation of the pipeline method has proven to be instrumental in enhancing the efficiency of the Gaussian filter. This improvement is reflected in a notable 48% increase in speed and a commendable 12% reduction in power consumption. However, it comes at the cost of a 27% increase in the required area.

Table 2. Comparison on physical properties of gaussian filter (GF) and pipeline GF (PGF)

	Power (mW)	Delay (ns)	Logic
GF	119.45	9.82	414
PGF	104.96	5.09	529

Table 3 presents the hardware specifications of Gaussian filters implemented with approximate adders. The table highlights the power-efficient characteristics of certain approximate filters. The notation APFAiLj denotes the ith approximation of APFA, where j least significant bits are computed approximately. Filters utilizing approximate adders with the sum bit derived from the output carry bit exhibit slower performance. Notably, APFA5 stands out as the least power-consuming approximate filter, achieving a power reduction of over 20%. Additionally, APFA6, APFA7, and APFA8 significantly enhance the speed of the Gaussian filter by more than 70%.

The Power-Delay Product (PDP) is a metric used to evaluate the power efficiency of a digital circuit. It is calculated by multiplying the power consumption of the circuit by its propagation delay. The power delay product is particularly relevant in digital design because it provides insights into how efficiently a circuit performs in terms of both speed and power consumption. A lower PDP value indicates better

power efficiency because it signifies that the circuit achieves a balance between low power consumption and fast operation. Designers often aim to minimize the power-delay product to enhance the overall performance and energy efficiency of digital systems. Based on the data presented in Figure 9, it is evident that APFA 4, 5, and 6 exhibit the most favorable Power-Delay Product (PDP) values, indicating superior power efficiency and speed performance. On the other hand, APFA2 is identified as having the least favorable PDP among the analyzed approximate adders. This observation underscores the importance of considering the trade-off between power consumption and delay in the selection of approximate adders for specific applications.

Table 3. Comparative Analysis of Physical Properties between Gaussian Filter (GF) and Pipeline Gaussian Filter (PGF)

APGF	Power reduction%	Speed up %	Area reduction %
APFA1L8	4.09	31.19	6.62
APFA2L2	4.33	4.33	21.55
APFA2L3	5.81	5.81	20.04
APFA2L4	8.39	8.39	19.09
APFA2L8	4.92	4.92	13.80
APFA3L5	6.77	38.96	1.51
APFA3L6	7.85	47.05	1.70
APFA3L7	7.45	49.12	2.27
APFA3L8	5.81	62.55	2.27
APFA4L4	7.45	-7.64	-14.74
APFA4L6	5.81	-9.10	-14.93
APFA5L5	4.50	-28.64	-16.82
APFA5L6	10.49	-21.26	-21.36
APFA5L7	15.14	0.47	-25.90
APFA5L8	21.34	-12.81	-30.43
APFA6L4	4.10	-18.51	-10.78
APFA6L7	4.96	-30.26	-10.78
APFA6L8	4.95	-14.93	-10.78
APFA7L1	9.25	50.12	9.07
APFA7L3	5.31	68.02	18.34
APFA7L4	4.47	72.40	17.01
APFA7L5	7.45	70.45	15.88
APFA7L7	7.16	69.88	15.12
APFA8L1	4.06	50.59	26.47
APFA8L4	6.65	61.06	27.22
APFA9L1	4.06	50.59	26.47
APFA9L4	6.65	61.06	27.22
APFA10L6	9.91	59.92	29.30

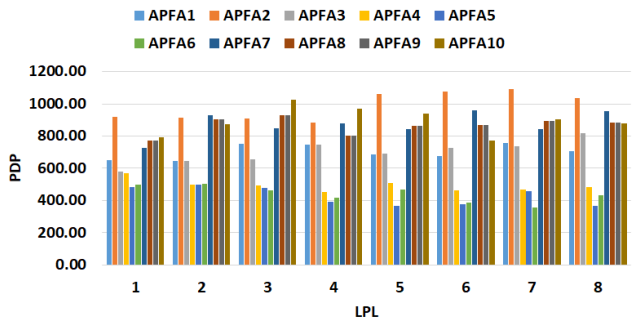

Figure 9. PDP values for different approximate gaussiaan filters

7. Conclusion

In this paper, we propose a novel architecture aimed at enhancing the efficiency of the Gaussian filter for the removal of Gaussian noise in underwater images. The key innovation lies in the utilization of a pipeline structure for the implementation of the Gaussian filter. Additionally, we conduct a comprehensive evaluation of the impact of employing ten approximate adders on the filter's performance.

The simulation results demonstrate that adopting the pipeline structure along with 2 to 8-bit approximation in adders leads to a significant improvement in the speed of the Gaussian filter, exceeding 150%. Moreover, this approach yields a noteworthy enhancement in power consumption, surpassing 34%. However, it is essential to note that these advantages come with an associated increase in the required area. While acknowledging the tradeoff between output quality and power, our design holds particular relevance for error-resilient applications, such as image and video processing. The proposed structure provides a valuable solution for scenarios where the benefits of heightened speed and reduced power consumption outweigh the increase in spatial requirements.

8. References

[1] Fatan, M., Daliri, M. R., & Shahri, A. M. (2016). Underwater cable detection in the images using edge classification based on texture information. Measurement, 91, 309-317.

[2] Saini, A., & Biswas, M. (2019). Object detection in underwater image by detecting edges using adaptive thresholding. 2019 3rd International Conference on Trends in Electronics and Informatics (ICOEI),

[3] Princess, P. J. B., Silas, S., & Rajsingh, E. B. (2019). Performance analysis of edge detection algorithms for object detection in accident images. 2019 Global Conference for Advancement in Technology (GCAT),

[4] Oliveira, A. J., Ferreira, B. M., & Cruz, N. A. (2021). A performance analysis of feature extraction algorithms for acoustic image-based underwater navigation. Journal of Marine Science and Engineering, 9(4), 361.

[5] Prasenan, P., & Suriyakala, C. (2022). A Study of Underwater Image Pre-processing and Techniques. In Computational Vision and Bio-Inspired Computing: Proceedings of ICCVBIC 2021 (pp. 313-333). Springer.

[6] Borker, S., & Bonde, S. (2017). Contrast Enhancement and Visibility Restoration of Underwater Optical Images Using Fusion. International Journal of Intelligent Engineering & Systems, 10(4).

[7] Mishra, A., Gupta, M., & Sharma, P. (2018). Enhancement of underwater images using improved CLAHE. 2018 International Conference on Advanced Computation and Telecommunication (ICACAT),

[8] Yang, S., Chen, Z., Feng, Z., & Ma, X. (2019). Underwater image enhancement using scene depth-based adaptive background light estimation and dark channel prior algorithms. IEEE Access, 7, 165318-165327.

[9] Bhairannawar, S. S. (2018). Efficient medical image enhancement technique using transform HSV space and adaptive histogram equalization. In Soft Computing Based Medical Image Analysis (pp. 51-60). Elsevier.

[10] Ulutas, G., & Ustubioglu, B. (2021). Underwater image enhancement using contrast limited adaptive histogram equalization and layered difference representation. Multimedia Tools and Applications, 80, 15067-15091.

[11] Priyadharsini, R., Sharmila, T. S., & Rajendran, V. (2016). An efficient edge detection technique using filtering and morphological operations for underwater acoustic images. Proceedings of the Second International Conference on Information and Communication Technology for Competitive Strategies,

[12] Shourya, S., Kumar, S., & Jha, R. K. (2016). Adaptive fractional differential approach to enhance underwater images. 2016 Sixth International Symposium on Embedded Computing and System Design (ISED),

[13] Singh, N., & Bhat, A. (2023). A robust model for improving the quality of underwater images using enhancement techniques. Multimedia Tools and Applications, 1-22.

[14] Xiao, B., Wang, K., Bi, X., Li, W., & Han, J. (2018). 2D-LBP: an enhanced local binary feature for texture image classification. IEEE Transactions on Circuits and Systems for Video Technology, 29(9), 2796-2808.

[15] Ponomarev, A., Nalamwar, H. S., Babakov, I., Parkhi, C. S., & Buddhawar, G. (2016). Content-based image retrieval using color, texture and shape features. Key Engineering Materials, 685, 872-876.

[16] Humeau-Heurtier, A. (2019). Texture feature extraction methods: A survey. IEEE Access, 7, 8975-9000.

[17] Qasaimeh, M., Denolf, K., Lo, J., Vissers, K., Zambreno, J., & Jones, P. H. (2019). Comparing energy efficiency of CPU, GPU and FPGA implementations for vision kernels. 2019 IEEE international conference on embedded software and systems (ICESS),

[18] Gupta, U., Babu, M., Ayoub, R., Kishinevsky, M., Paterna, F., Gumussoy, S., & Ogras, U. Y. (2018). An online learning methodology for performance modeling of graphics processors. IEEE Transactions on Computers, 67(12), 1677-1691.

[19] HajiRassouliha, A., Taberner, A. J., Nash, M. P., & Nielsen, P. M. (2018). Suitability of recent hardware accelerators (DSPs, FPGAs, and GPUs) for computer vision and image processing algorithms. Signal Processing: Image Communication, 68, 101-119.

[20] Diouri, O., Gaga, A., Ouanan, H., Senhaji, S., Faquir, S., & Jamil, M. O. (2022). Comparison study of hardware architectures performance between FPGA and DSP processors for implementing digital signal processing algorithms: Application of FIR digital filter. Results in Engineering, 16, 100639.

[21] De Haro, J. M., Bosch, J., Filgueras, A., Vidal, M., Jiménez-González, D., Alvarez, C., Martorell, X., Ayguadé, E., & Labarta, J. (2021). OmpSs@ FPGA framework for high performance FPGA computing. IEEE Transactions on Computers, 70(12), 2029-2042.

[22] Pirzada, S. J. H., Murtaza, A., Xu, T., & Jianwei, L. (2020). A reconfigurable model-based design for rapid prototyping on FPGA. International Journal of Computer Theory and Engineering, 12(3), 80-84.

[23] Chamola, V., Patra, S., Kumar, N., & Guizani, M. (2020). Fpga for 5g: Re-configurable hardware for next generation communication. IEEE Wireless Communications, 27(3), 140-147.

[24] Cabello, F., León, J., Iano, Y., & Arthur, R. (2015). Implementation of a fixed-point 2D Gaussian Filter for Image Processing based on FPGA. 2015 Signal Processing: Algorithms, Architectures, Arrangements, and Applications (SPA),

[25] Murray, K. E., Luu, J., Walker, M. J., McCullough, C., Wang, S., Huda, S., Yan, B., Chiasson, C., Kent, K. B., & Anderson, J. (2020). Optimizing FPGA logic block architectures for arithmetic. IEEE Transactions on Very Large Scale Integration (VLSI) Systems, 28(6), 1378-1391.

[26] Nomani, T., Mohsin, M., Pervaiz, Z., & Shafique, M. (2020). xUAVs: Towards efficient approximate computing for UAVs—Low power approximate adders with single LUT delay for FPGA-based aerial imaging optimization. IEEE Access, 8, 102982-102996.

[27] Zhu, Z., Zhang, J., Zhao, J., Cao, J., Zhao, D., Jia, G., & Meng, Q. (2019). A hardware and software task-scheduling framework based on CPU+ FPGA heterogeneous architecture in edge computing. IEEE Access, 7, 148975-148988

[28] Guraksin, G. E., Deperlioglu, O., & Kose, U. (2019). A novel underwater image enhancement approach with wavelet transform supported by differential evolution algorithm. Nature Inspired Optimization Techniques for Image Processing Applications, 255-278.

[29] S. M. Alex Raj, M. H. S. (2015). FPGA Implementation of Underwater Image Enhancement using Nonlinear Filtering. Indian Journal of Science and Technology, 8(35),1-5. https://doi.org/10.17485/ijst/2015/v8i35/79110

[30] Aguirre-Castro, O., García-Guerrero, E., López-Bonilla, O., Tlelo-Cuautle, E., López-Mancilla, D., Cárdenas-Valdez, J., Olguín-Tiznado, J., & Inzunza-González, E. (2022). Evaluation of underwater image enhancement algorithms based on Retinex and its implementation on embedded systems. Neurocomputing, 494, 148-159.

[31] Park, J. W., Lee, H., Kim, B., Kang, D.-G., Jin, S. O., Kim, H., & Lee, H.-J. (2019). A low-cost and high-throughput FPGA implementation of the retinex algorithm for real-time video enhancement. IEEE Transactions on Very Large Scale Integration (VLSI) Systems, 28(1), 101-114.

[32] Padhy, A. P., & Das, B. P. (2023). Lightweight Approximate Multiplier with Improved Accuracy in FPGA for Error Resilient Application. 2023 36th International Conference on VLSI Design and 2023 22nd International Conference on Embedded Systems (VLSID),

[33] Ullah, S., & Kumar, A. (2023). Approximate Arithmetic Circuit Architectures for FPGA-based Systems. Springer Nature.

[34] Amrouch, H., Ehsani, S. B., Gerstlauer, A., & Henkel, J. (2019). On the efficiency of voltage overscaling under temperature and aging effects. IEEE Transactions on Computers, 68(11), 1647-1662.

[35] Bahoo, A. A., Akbari, O., & Shafique, M. (2023). An Energy-Efficient Generic Accuracy Configurable

Multiplier Based on Block-Level Voltage Overscaling. IEEE Transactions on Emerging Topics in Computing.

[36] Jiang, H., Santiago, F. J. H., Mo, H., Liu, L., & Han, J. (2020). Approximate arithmetic circuits: A survey, characterization, and recent applications. Proceedings of the IEEE, 108(12), 2108-2135.

[37] Mafi, M., Martin, H., Cabrerizo, M., Andrian, J., Barreto, A., & Adjouadi, M. (2019). A comprehensive survey on impulse and Gaussian denoising filters for digital images. Signal Processing, 157, 236-260.

[38] Anusha, G., & Deepa, P. (2020). Design of approximate adders and multipliers for error tolerant image processing. Microprocessors and Microsystems, 72, 102940.

[39] Assessment, I. Q. (2004). From error visibility to structural similarity. IEEE transactions on image processing, 13(4), 93.

[40] Liang, J., Han, J., & Lombardi, F. (2012). New metrics for the reliability of approximate and probabilistic adders. IEEE Transactions on Computers, 62(9), 1760-1771.

[41] Li, C., Guo, C., Ren, W., Cong, R., Hou, J., Kwong, S., & Tao, D. (2019). An underwater image enhancement benchmark dataset and beyond. IEEE transactions on image processing, 29, 4376-4389.